An Analytical Framework for Field Electron Emission, Incorporating Quantum-Confinement Effects

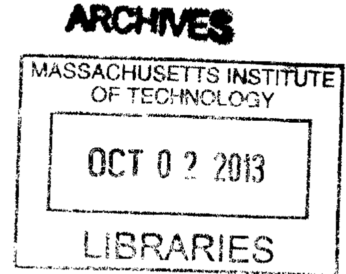

by

Alex A. Patterson

B.S., Electrical Engineering (2011)
University of Pittsburgh

Submitted to the Department of Electrical Engineering and Computer Science
in partial fulfillment of the requirements for the degree of

Master of Science

at the

MASSACHUSETTS INSTITUTE OF TECHNOLOGY

September 2013

© Massachusetts Institute of Technology 2013. All rights reserved.

Author ....
Department of Electrical Engineering and Computer Science
July 30, 2013

Certified by.....
Akintunde I. Akinwande
Professor of Electrical Engineering and Computer Science
Thesis Supervisor

Accepted by.......
Leslie A. Kolodziejski
Chairman, Department Committee on Graduate Theses

An Analytical Framework for Field Electron Emission, Incorporating Quantum-Confinement Effects

by

Alex A. Patterson

Submitted to the Department of Electrical Engineering and Computer Science
on July 30, 2013, in partial fulfillment of the
requirements for the degree of
Master of Science

Abstract

As field electron emitters shrink to nanoscale dimensions, the effects of quantum confinement of the electron supply and electric field enhancement at the emitter tip play a significant role in determining the emitted current density (ECD). Consequently, the Fowler-Nordheim (FN) equation, which primarily applies to field emission from the planar surface of a bulk metal may not be valid for nanoscale emitters. While much effort has focused on studying emitter tip electrostatics, not much attention has been paid to the consequences of a quantum-confined electron supply. This work builds an analytical framework from which ECD equations for quantum-confined emitters of various geometries and materials can be generated and the effects of quantum confinement of the electron supply on the ECD can be studied. ECD equations were derived for metal emitters from the elementary model and for silicon emitters via a more physically-complete version of the elementary model.

In the absence of field enhancement at the emitter tip, decreasing an emitter's dimensions is found to decrease the total ECD. When the effects of field enhancement are incorporated, the ECD increases with decreasing transverse emitter dimensions until a critical dimension d_{peak}, below which the reduced electron supply becomes the limiting factor for emission and the ECD decreases. Based on the forms of the ECD equations, alternate analytical methods to Fowler-Nordheim plots are introduced for parameter extraction from experimental field emission data. Analysis shows that the FN equation and standard analysis procedures overpredict the ECD from quantum-confined emitters. As a result, the ECD equations and methods introduced in this thesis are intended to replace the Fowler-Nordheim equation and related analysis procedures when treating field emission from suitably small field electron emitters.

Thesis Supervisor: Akintunde I. Akinwande
Title: Professor of Electrical Engineering and Computer Science

Acknowledgments

There are many people who have played an important role in me completing this work and I would like to thank them below. For those whom I may not have mentioned, thanks go out to you as well.

First, I'd like to thank my advisor, Professor Tayo Akinwande, for his guidance, encouragement, and support during this work. I could not possibly enumerate either the lessons I have learned or the great advice he has given me in the first two years of my graduate education. He holds his students to the highest scientific standards, making sure that they conduct their research carefully and completely, and from this I have grown immensely as a researcher and student. I appreciate that he has given me so much freedom in choosing the work I want to pursue, but also bringing me back to Earth when I need it. From him I have also learned that my work is only as good as my ability to convey it to others, whether it be placing it within the big picture or organizing my research into a compelling narrative. His enthusiasm for research and education is infectious and has served as a continuing motivation in my own career.

I would also like to thank the members of the Akinwande group: Melissa Smith, Steve Guerrera, and Arash Fomani, who have made this work and my experience as a graduate student go much more smoothly than it probably should have. They have answered my incessant questions about graduate school, served as a sounding board for my research ideas, and given me solid advice on so many topics. From discussions in the office to spending some quality time at the library, my group-mates have made life in building 39 truly a great experience.

Finally, I would like to thank my mom, dad, and brother for making sure that I take time to enjoy life outside my work and providing comic relief and reassurance when I needed it; Dan for his encouragement, commiseration as a fellow graduate student, and discussions about the elegance of physics and mathematics; Cait for her continued support and advice on life in general; the Exit Row Bros for keeping the graduate student life in (and outside of) Cambridge fun and continually interesting; Dr. David "Degas" Perello, Mike Rogers, and the members of Degas for ensuring that I don't forget about the importance of all my other major interests.

Again, thanks to you all!

Contents

1 Introduction **21**

2 Background **25**

2.1 Fowler-Nordheim Equation 25

2.2 Fowler-Nordheim-Type Equations 31

2.2.1 Temperature Correction Factor: λ_T 32

2.2.2 Band Structure Correction Factor: λ_B 32

2.2.3 Field Enhancement Factor: γ_a 37

2.2.4 Tunneling Prefactor and Correction Factor: P and λ_P 38

2.2.5 Barrier Shape and Decay Width Correction Factors: ν and λ_τ 40

2.3 Emission from Semiconductors 40

2.3.1 Emission from the Conduction Band for $E_F > 0$ 41

2.3.2 Emission from the Conduction Band for $E_F < 0$ 44

2.3.3 Emission from the Valence Band for $E_{Fv} < 0$ 46

2.3.4 Field Penetration and Band Bending 49

2.3.5 Tunneling from an Accumulation Layer 51

2.4 Emission from Quantum-Confined Emitters 53

2.4.1 Emission from a Nanowall Edge 53

2.4.2 Emission from a Thin Slab 57

2.5 Chapter Summary 59

3 Elementary Framework for Cold Field Emission from Metal Emitters 61

3.1 Introduction . . . 61

3.2 Model for Field Emission from Quantum-Confined Emitters . . . 62

3.2.1 Definition of Emitter System . . . 62

3.2.2 Quantum Confinement of Electrons . . . 62

3.3 Construction of the Framework . . . 68

3.3.1 Emitted Current Density . . . 68

3.3.2 Supply Functions . . . 68

3.3.3 Transmission Function . . . 71

3.4 Application of the Elementary Framework: Emitted Current Density Equations . . . 76

3.4.1 Normally-Unconfined Emitted Current Density Equations . . . 77

3.4.2 Normally-Confined Emitted Current Density Equations . . . 81

3.5 Chapter Summary . . . 84

4 Treatment of Field Emission from Quantum-Confined Silicon Emitters 85

4.1 Introduction . . . 85

4.2 Correction Factors: Emitter Electrostatics . . . 86

4.2.1 Schottky-Nordheim Barrier for Semiconductors . . . 86

4.3 Correction Factors: Emitter Electron Supply for Silicon . . . 87

4.3.1 Material Properties of Silicon . . . 87

4.3.2 Band Structure Corrections for QC Emitters . . . 88

4.4 Emitted Current Density Equations for Silicon . . . 92

4.4.1 ECD Equations: Conduction Band $E_F > 0$ . . . 94

4.4.2 ECD Equations: Conduction Band $E_F < 0$ . . . 101

4.5 Chapter Summary . . . 106

5 **Analysis of the Emitted Current Density from Quantum-Confined Emitters** **109**
5.1 Introduction 109
5.2 ECD as a Function of Emitter Dimensions: Elementary Model 110
5.2.1 Effects of Transverse Quantum Confinement 110
5.2.2 Normal Quantum Confinement 113
5.3 ECD as a Function of the Quantum Well Width: Silicon ECD Equations 117
5.3.1 Finite Temperature 117
5.3.2 Schottky-Nordheim Barrier 118
5.3.3 Band Structure Effects 119
5.4 Fowler-Nordheim Plots for Quantum-Confined Emitters 123
5.4.1 Parameter Extraction from Normally-Unconfined Emitters . . 123
5.4.2 NC Emitters 127
5.5 Comparison of Framework Equations to Experimental Data 128
5.5.1 Vertical Single-Layer Graphene 128
5.5.2 Single-Walled Carbon Nanotube 130
5.6 Chapter Summary 131

6 **Thesis Summary and Future Work** **135**
6.1 Summary 135
6.2 Model Limitations 137
6.3 Future Work 139

A **Poisson-Boltzmann Formulation of Band Bending** **153**

B **Elementary Emitted Current Density Equations** **157**
B.1 Normally-Unconfined Emitted Current Density Equations 157
B.1.1 NU Nanowire 157
B.2 Normally-Confined Emitted Current Density Equations 158

B.2.1 NC Nanowall 158
B.2.2 NC Rectangular Nanowire 158
B.2.3 NC Cylindrical Nanowire 159

C Field Enhancement Factor 161
C.1 Floating Sphere at Emitter Plane Potential 161
C.2 Semicylinder on Emitter Plane 162
C.3 Floating Cylinder at Emitter Plane Potential 164

D Emission from an Accumulation Layer 167
D.1 Accumulation Layer Well 167
D.2 Accumulation Layer Emitted Current Density 172

E Transition Region Between Emitter Dimensionalities 175
E.1 Transition Point 175
E.2 Transition Region and the Influence of System Parameters 176
E.2.1 Work Function 177
E.2.2 Effective Mass of Electrons 178
E.2.3 Applied Electric Field 179
E.2.4 Fermi Energy 179

List of Figures

1-1 A plot of the output power vs. operating frequency of state-of-the-art continuous-wave terahertz sources shows a lack of devices with power outputs of 1 W or greater between approximately 100 GHz and 10 THz. QCLs are represented by (□), frequency multipliers by (•) and other electronic devices by (-). Cryogenic results are plotted as hollow symbols. 22

2-1 Field emission consists of electrons being emitted from a material that has an electric field applied to one of its surfaces. The magnitude of the emitted current density depends on the electron flux at the surface of the emitter and the probability of electrons tunneling from the material into vacuum. 26

2-2 Normal energy diagram for a bulk metal emitter. As W increases, the barrier height seen by tunneling electrons decreases. 28

2-3 Fowler-Nordheim plot for an emitter with $\phi = 5$ eV. The linear fit y-intercept is equal to A and the slope is $-B\phi^{3/2}$. 29

2-4 Normal energy diagram for a bulk emitter with the Schottky-Nordheim barrier potential. 29

2-5 An example of a constant energy surface. This constant energy surface is being projected into the k_x-k_y plane, which is perpendicular to the emission direction. Figure adapted from [1]. 33

2-6 (a) Ellipsoidal constant energy surface with $m_0 > m_z > m_x = m_y$ (blue) compared to the free electron constant energy surface (red), (b) ellipsoidal and free electron constant energy surfaces projected into the $k_x - k_y$ plane, and (c) ellipsoidal and free electron constant energy surfaces projected into the $k_x - k_z$ plane. 34

2-7 Actual and free electron constant energy surfaces projected into the E_x-E_y plane. The area inside the red (blue) contour represents electron states that contribute to the free electron (actual) ECD. Areas shaded gray (orange) are electron states that contribute to the actual (free electron) ECD, but are excluded by the free electron (actual) ECD. If the constant energy surface has a neck, it is projected as an absence of electronic states in the E_x-E_y plane and therefore is also shaded orange. Figure adapted from [1]. 36

2-8 A schematic for the "floating sphere at emitter plane potential" model. The center of the sphere of radius ρ is located a distance l above the emitter plane. Far away from the sphere, the electric field is F_M, while at the apex of the sphere it is approximately $(3.5 + l/\rho)\, F_M$. 38

2-9 When the Fermi energy of a semiconductor emitter is located above the conduction band edge, most emitted electrons come from states close in energy to the Fermi energy. These electrons see a barrier height equal to the work function of the semiconductor, ϕ. 42

2-10 When the Fermi energy of the semiconductor is below the conduction band edge, most emitted electrons come from states close in energy to the edge of the conduction band. This presents a barrier height equal to the electron affinity of the semiconductor, χ_e. 45

2-11 For emission from the valence band, the majority of emitted electrons have energies close to the valence band edge. The barrier to transmission is the sum of the semiconductor's electron affinity, χ_e, and band gap energy, E_g. . . . 48

2-12 For $F = 5 \times 10^7 V/cm$, $N_D = 10^{17} cm^{-3}$, and $T = 300$ K, the magnitude of the band bending in silicon is approximately $\Delta\phi = 0.259 eV$. . . . 50

2-13 Band bending near the surface of a semiconductor leads to the formation of an accumulation layer and quasi-bound, discrete electronic states. In a MOS structure, the electrons in the accumulation layer can tunnel through the thin oxide layer from the substrate into the gate, leading to a current across the oxide layer. Figure adapted from [2]. . 52

2-14 Illustration of a nanowall emitter and the relative sizes of its dimensions. The structure is absolutely small in the x direction and has a quantum well width L_x in that dimension. The electric field F_M is applied from the z direction. . . . 54

2-15 Normal energy diagram for a nanowall emitter. The presence of transverse quantum confinement decreases the ERL in each subband and increases the reference zero-field barrier height relative to a bulk emitter. 56

2-16 A thin slab is absolutely small in the direction of emission, z, but semi-infinite in the x and y directions. L_z is small enough to consider the emitter to be quantum confined, discretizing energies in the emission direction. . . . 57

3-1 Normally-unconfined emission (left) is characterized by a lack of quantum confinement in the direction of emission, while normally-confined emission (right) consists of an emitter confined in the emission direction. 63

3-2 Diagram of the infinite square well of width L and the first four energy levels. . . . 64

3-3 Diagram of the infinite cylindrical well of radius a. 65
3-4 Normal energy diagrams for (a) bulk emitter, (b) normally-unconfined emitter that is also transversally confined, and (c) normally-confined emitter that is not transversally confined (c). 75
3-5 Emission from a bulk emitter (left) and normally-unconfined nanowall emitter (right). 78
3-6 Emission from a normally-unconfined rectangular nanowire (left) and normally-unconfined cylindrical nanowire emitter (right). 79
3-7 Emission from a normally-confined nanowall emitter. 82
3-8 Emission from a normally-confined nanowire emitter. 83

4-1 Electron constant energy surfaces of silicon. 87
4-2 Heavy hole and light hole constant energy surfaces for the valence band of silicon. The split-off band is excluded due to its maximum lying lower in energy than the heavy hole and light hole bands. 87
4-3 When projected into the k_x-k_y plane, the ellipsoidal constant energy surfaces of silicon become circles (characterized by m_t) along the axis of emission and ellipses (characterized by m_t and m_l) on axes perpendicular to the axis of emission. 89
4-4 Plotting the ECD from an elliptical constant energy projection of a bulk emitter together with the ECD from the approximated circular constant energy projection with $E_m = E\sqrt{m_t m_l}/m_0$ shows that the approximation is in good agreement with the exact result. 90
4-5 The 3D constant energy surfaces of silicon are reduced to constant energy contours in 2D and constant energy points in 1D. 91

4-6 For a 3D electron gas, ΔW is defined between two constant energy surfaces and takes on continuous values, while for a 2D electron gas it is defined between two constant energy contours of the same subband index and is continuous within each subband. In the case of a 1D electron gas, ΔW is defined between two constant energy points in the transverse plane and is entirely discrete. 92

4-7 The numerically-calculated total ECD with band structure effects (points) and analytical, band-structure-corrected total ECD calculated via the quasi-continuum approximation for a single circular constant energy projection (solid) for a 1 nm NU nanowall as a function of the applied field. 93

5-1 ECD from the NU nanowall emitter, NU rectangular nanowire emitter, and NU cylindrical nanowire emitter as a function of L_x, $L_x = L_y$, and $2a$ respectively, with $\phi = 5$ eV and $E_F = 10$ eV at $F = 2 \times 10^7$ V/cm. 111

5-2 Normalized ECD of the NU cylindrical nanowire emitter and bulk emitter with γ_a defined by the floating sphere model, with a constant applied field far from the emitter surface of $F_M = 1.145 \times 10^5$ V/cm, $\phi = 5$ eV, $E_F = 10$ eV, and an emitter height of $l = 1$ μm. The peak in the ECD curve occurs at $a = d_{peak}$, right of which field enhancement dominates the ECD and left of which quantum confinement dominates the ECD. 113

5-3 ECD from the NC nanowall and NC rectangular nanowire as a function of L_z and $L_x = L_z$ respectively, with $\phi = 5$ eV and $E_F = 10$ eV at $F = 2 \times 10^7$ V/cm. Plot points represent the average ECD per well width, calculated from a Gaussian distribution of well widths with a mean of the well width and standard deviation of 10% of the mean. . 114

5-4 ECD from the first subband of an NC nanowall emitter with selected quantum well widths labeled (top left), quantum wells with widths equal to the labels in the ECD plot and the corresponding normal energy level in each well (top right), and the average number of emitted electrons from the subband as a function of the normal energy W_Q (bottom). 116

5-5 Correction factors for a bulk emitter, 1 nm NU nanowall emitter, and 1 nm $\times$ 1 nm rectangular nanowire emitter as a function of the applied field for the first subband, at $T = 300$ K, with $\phi = 5$ eV and $E_F = 5$ eV. 120

5-6 Correction factors for the 15th (top), 10th, 5th, and 1st (bottom) subbands of a 10 nm NC nanowall emitter as a function of the applied field. The solid curves are the correction factors for the circular constant energy cross sections, while the dashed curves represent the elliptical constant energy cross sections. 121

5-7 Correction factors for the 15th (top), 10th, 5th, and 1st (bottom) subbands of a 10 nm x 10 nm NC rectangular nanowire emitter as a function of the applied field. The solid curves are the correction factors for the circular constant energy cross sections, while the dashed curves represent the elliptical constant energy cross sections. 121

5-8 The correction factors for NU emitters with $E_F < 0$ are the same between emitter geometries. For low applied fields, the correction factors increase sharply, but converge to the ratio of the effective mass to the free electron mass for high applied fields. 122

5-9 FN plots for for an elementary bulk emitter, 5 nm NU nanowall emitter, 1 nm NU nanowall emitter, 5 nm $\times$ 5 nm NU rectangular nanowire emitter, and 1 nm $\times$ 1 nm rectangular nanowire emitter for which $E_F = 10$ eV, $\phi = 5$ eV. 124

5-10 Experimental field emission data from a vertically-oriented single-layer graphene sheet for three different voltage sweeps, overlaid by the ECD predicted by Equation 5.17 for emitters with heights of 8.5 μm, 10.5 μm, and 14 μm. Dashed curves represent the ECD predicted for a bulk emitter of equivalent geometry. 130

5-11 Field emission data from four sets of experimental setups, where a is the SWNT radius, l is the SWNT length, and d is the SWNT-anode spacing: (a) $a = 5$ nm, $l = 0.66$ μm, $d = 2$ μm, (b) $a = 7$ nm, $l = 1.32$ μm, $d = 2$ μm, (c) $a = 7$ nm, $l = 2.35$ μm, $d = 3.75$ μm, and (d) $a = 5$ nm, $l = 4.56$ μm, $d = 5.8$ μm. Both the NU cylindrical nanowire equation and bulk emitter equation are plotted for each data set. . . 131

C-1 The "semicylinder on emitter plane" model consists of a semicylinder of radius ρ on a plane. The semicylinder and emitter plane form an equipotential system. 162

C-2 In the "floating cylinder at emitter plane potential" model, the center of a cylinder of radius ρ is a distance l above the emitter plane. The wire between the cylinder and the emitter plane indicates that they form an equipotential system. 164

D-1 The accumulation well is bounded by the energy of the conduction band edge in the bulk, the conduction band edge near the interface, and the semiconductor-vacuum boundary. 168

E-1 Normal energy diagram for emission from the NU nanowall. Lowering ϕ reduces the barrier thickness seen at the reference energy W_R and increases the transmission probability of electrons in that subband. . 177

E-2 The ECD of the NU nanowall normalized to the FN equation, as a function of the transverse well width L_x with the work function as a parameter, for which $F = 2 \times 10^7$ V/cm, $E_F = 10$ eV. 177

E-3 Normal energy diagram for emission from the NU nanowall. Decreasing the effective mass of electrons in the well, m^* causes all well energy levels to migrate upwards in energy, leading to a decrease in the reference state energy from W_R to W_R^* and a reduced transmission probability for electrons in that subband. 178

E-4 The ECD of the NU nanowall normalized to the FN equation, as a function of the transverse well width L_x with the effective mass m^* as a parameter, for which $F = 2 \times 10^7$ V/cm, $E_F = 10$ eV, $\phi = 5$ eV. . . 178

E-5 Normal energy diagram for emission from the NU nanowall. Increasing the applied electric field directly reduces the barrier thickness seen by electrons at reference energy W_R, increasing their transmission probability. 179

E-6 The ECD of the NU nanowall normalized to the FN equation, as a function of the transverse well width L_x with the applied field as a parameter, for which $E_F = 10$ eV and $\phi = 5$ eV. 179

E-7 The normalized ECD of the elementary NU nanowall for selected values of E_F. Above $E_{F,crit}$, changes in the Fermi energy do not affect the normalized ECD, while the ECD curve becomes discontinuous for Fermi energies below $E_{F,crit}$. 182

E-8 The normalized ECD of the elementary NC nanowall for selected values of E_F. As E_F decreases, the normalized ECD oscillations decrease in amplitude, become broader, and converge more quickly to the FN limit. For values of $E_F <\sim 0.2$ eV, the ECD is normalized to a numerically-integrated version of the FN equation. 183

List of Tables

2.1 Values for ν and t as functions of y [3]. 31

4.1 Selected material parameters of silicon [4,5]. 88

5.1 Work functions extracted from FN plots and FN-type plots for which $E_F = 10$ eV, $\phi = 5$ eV, and $\gamma_a = 1$. 125

D.1 Normalized energy levels for the logarithmic well calculated via the approximate JWKB method and exact three-point shooting Numerov method. 171

D.2 The first five energy levels in the accumulation layer well as a function of the donor dopant density in eV at $T = 300$ K. The conduction band edge in the bulk is taken as the energy reference. 171

D.3 Emitted current density from the accumulation layer well of a bulk silicon emitter ($J_{acc,bulk}$) and from the bulk silicon ECD equation without band bending (J_{bulk}) for $F = 2 \times 10^7\ V/cm$. 173

E.1 The midpoint of the transition region between the NU nanowall and bulk emitter, as determined by matching the extracted work functions from the FN plot and NUFN plots for the nanowall emitter, given in terms of L_x (nm). 176

Chapter 1

Introduction

The terahertz (THz) regime, which lies between 0.1THz and 10THz, is one of the most promising, yet technologically underdeveloped, regions of the electromagnetic spectrum. Recently, this frequency range has garnered increased attention within the scientific community due to its wide variety of practical applications in astronomy [6], medicine and biology [7], chemistry [8], atmospheric science [9], security [10], [11], and defense [12]. However, taking advantage of the properties of THz radiation has been especially challenging due to the lack of radiation sources that can operate with a significant power output (above 1 W) in this frequency range. This has come to be known as the THz technology gap. Figure 1-1 plots the power output of state-of-the-art continuous-wave electromagnetic radiation sources against their operating frequency. Solid-state devices such as frequency multipliers, amplifiers, resonant tunneling diodes, Impatts oscillators, and Gunn oscillators have achieved maximum operating frequencies of over 150 GHz, but are limited by the effects of electron velocity saturation, series resistance, and shunt capacitance as device sizes scale down [13]. Continuous-wave quantum cascade lasers (QCL) have demonstrated operation at frequencies as low as 0.84 THz, but must be cryogenically cooled to enable lasing at such low frequencies [14]. From the limitations of each of these types of devices, it

is clear that a new approach is needed. Vacuum nanoelectronic (VNE) devices are a

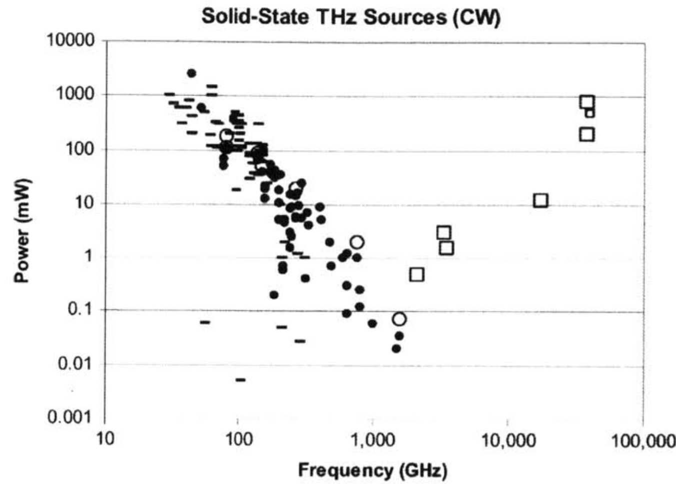

Figure 1-1: A plot of the output power vs. operating frequency of state-of-the-art continuous-wave terahertz sources shows a lack of devices with power outputs of 1 W or greater between approximately 100 GHz and 10 THz. QCLs are represented by (□), frequency multipliers by (•) and other electronic devices by (-). Cryogenic results are plotted as hollow symbols.

prime candidate for bridging the THz gap. Unlike solid-state electronic devices, the electrons in VNE devices travel through vacuum and can have saturation velocities that approach the speed of light. As an advantage over QCLs, VNE devices natively operate at room temperature [15]. In addition, if the electron transit distance in a VNE device is smaller than the mean free path of an electron in air, the devices need not be operated in a vacuum at all. To date, multiple terahertz VNE devices, such as the integrated microcavity klystron [16], vacuum channel transistor [17], and micro Barkhausen-Kurz THz oscillator [13], have been proposed.

The primary active component of any VNE device is the electron source. These sources are typically implemented via an electron field emitter array (FEA), which consists of a large number of closely-spaced field electron emitters. Due to the requirement of high current outputs from the electron source under low applied voltages [18] for VNE devices, it is desirable to reduce the lateral dimensions of field emitters for

larger electric field enhancement at the emitter tip and lower turn-on voltages. While experimentalists have succeeded in fabricating FEAs based on nanoscale field emitters in a variety of shapes and materials, such as carbon nanotubes [19], semiconductor nanostructures [20], and graphene [21], theoretical treatments and modeling of new types of field emitters have not kept pace. Primarily, as emitter dimensions shrink into the nanoscale, the effects of quantum confinement and electric field enhancement at the emitter tip play a significant role in determining the emitted current density (ECD). Consequently, the oft-cited Fowler-Nordheim (FN) equation, which was developed for and primarily applies to field emission from the planar surface of a bulk metal may not be valid for predicting the ECD from nanoscale emitters. This limitation of the FN equation is consistently overlooked in experimental studies and FN-type equations are routinely used to describe the ECD from carbon nanotubes, semiconductor nanowires, and graphene sheets. While many studies have focused on the electrostatics of nanoscale tip geometries [22–39], few have addressed the effects of quantum confinement on the electron supply in the emitter.

This work develops a unifying framework for treating field emission that incorporates effects of quantum-confinement on the electron supply. The framework unifies the existing ECD equations based on elementary models, such as the FN equation [40] and nanowall equation [41], and generates ECD equations for quantum-confined emitters of arbitrary geometry. In addition, the framework allows for an analysis of the effects of quantum confinement on emitters, such as the dependence of the ECD on the dimensions of the emitter. The ECD equations also provide an additional tool for experimentalists to use when analyzing field emission data from nanoscale emitters.

This thesis is divided into six chapters. Chapter 2 reviews previous theoretical and modeling work of field emission from metals, semiconductors, and quantum-confined structures. A framework for treating cold field emission from metal emitters of reduced dimensionality and equations predicting the emitted current density from

specific emitter geometries are derived in Chapter 3. Chapter 4 extends the applicability of the framework to silicon field emitters by incorporating correction factors into the ECD equations that account for physical phenomena that were omitted in developing the framework for metals. In Chapter 5, an analysis of the effects of quantum-confinement of the electron supply on the emitted current density from emitters of reduced dimensionality is performed, alternate data analysis procedures are proposed for quantum-confined emitters, and the ECD predicted by the model is compared to experimental field emission data from the literature for vertical graphene sheets and carbon nanotubes. Finally, a summary of the thesis, conclusions, limitations of the model, and proposed future work are covered in Chapter 6.

Chapter 2

Background

2.1 Fowler-Nordheim Equation

The first treatment of field electron emission came in 1928, with the publication of Fowler and Nordheim's "Electron emission in intense electric fields" [40]. This work produced the Fowler-Nordheim equation, which predicts the magnitude of the ECD emitted from the surface of a bulk metal: a metal large enough that the distribution of energy levels is assumed to be continuous. Fowler and Nordheim's model consisted of a Sommerfeld-type metal [42] at $T = 0$K with an electric field applied normal to a planar surface of the metal. The metal is composed of an ideal gas of free electrons which obey Fermi-Dirac statistics and have mass m_0, the mass of an electron in free space. All electronic states up to a maximum energy E_F, the Fermi energy, are occupied by electrons. Electron momenta in each translational degree of freedom are assumed to be independent of each other and can be separated into components that are normal and parallel to the emitting surface. Electrons with momentum normal to the emitting surface are defined as normal electrons with normal energy W, while all other electrons are termed transverse electrons, with transverse energy E_t, such that $E = W + E_t$. The surface of the metal is taken to be planar, perfectly smooth, free

of defects, and to have a uniform local work function equal to ϕ. The applied electric field, F, does not penetrate into the metal and creates a nearly triangular potential barrier between the metal and vacuum at the metal surface.

The emitted current density from a bulk metal, $J(F)$ is proportional to the product of the supply function, $N(W)$, and transmission function $D(F, W)$, as illustrated in Figure 2-1. The total emitted current density is calculated by integrating over all

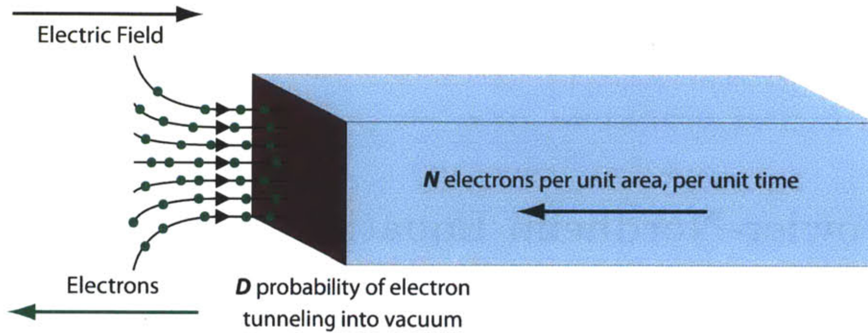

Figure 2-1: Field emission consists of electrons being emitted from a material that has an electric field applied to one of its surfaces. The magnitude of the emitted current density depends on the electron flux at the surface of the emitter and the probability of electrons tunneling from the material into vacuum.

normal energies and multiplying by the elementary charge, e:

$$J(F) = e \int N(W) D(F, W) dW \tag{2.1}$$

In the FN model, the supply function quantifies the number of electrons passing through a plane parallel to the emitting surface per unit area, per unit time. It is calculated by integrating the product of the electron group velocity, density of states in the direction of emission, density of states transverse to the direction of emission, and Fermi function over all k vectors in the transverse plane. The resulting supply function is

$$N(W) = \frac{4\pi m_0 k_B T}{h^3} \ln \left[1 + \exp\left[-\frac{W - E_F}{k_B T}\right]\right] \tag{2.2}$$

where k_B is Boltzmann's constant, h is Planck's constant, T is the thermodynamic temperature of the metal, W is the energy normal to the emitting surface, and E_F is the Fermi energy. The probability of an electron tunneling through the potential barrier is determined by the transmission function, which is calculated using a Jeffreys-Wentzel-Kramers-Brillouin (JWKB)-type approximation [43–46]:

$$D(F,W) \approx \exp\left[-g_0 \int_0^Z \sqrt{H - eV(F,z)}dz\right] \tag{2.3}$$

where z is the emission direction, $g_0 = 4\pi\sqrt{2m_0}/h$, $H = \phi + E_F - W$ is the height of the potential barrier in the absence of an applied electric field (zero-field barrier height), V is the barrier potential, and 0 and Z are the classical turning points of the electron. For the exact triangular barrier $V(F,z) = Fz$ and

$$D(F,W) = \exp\left[-\frac{B}{F}H^{3/2}\right] \tag{2.4}$$

where $B = (8\pi/3eh)\sqrt{2m_0}$ is the second FN constant, and F is the electric field at the surface of the metal. Figure 2-2 shows the relation between the electron normal energy, barrier height, and barrier thickness. Since most of the emitted electrons come from states near in energy to the Fermi energy, Equation 2.4 can be expanded about $W = E_F$:

$$D(F,W) = \exp\left[-\frac{B}{F}\phi^{3/2} + c(W - E_F)\right] \tag{2.5}$$

where $c = 3B\sqrt{\phi}/2F$ is the transmission function decay rate [47]. Integrating the product of Equation 2.2 and Equation 2.5 over all energies normal to the emitting surface and multiplying by the elementary charge yields the total current density emitted from the metal. In order to obtain an approximate, analytical solution, the limit as $T \to 0$ K is taken in Equation 2.2 and the lower limit of integration is extended from $W = 0$ to $W = -\infty$. The result is the elementary Fowler-Nordheim equation,

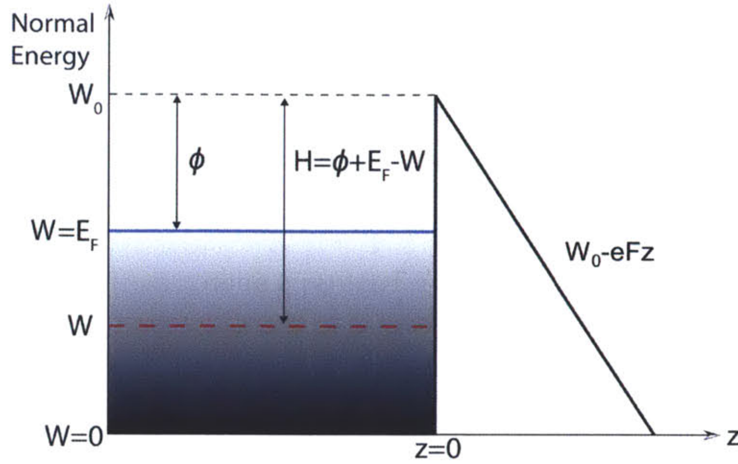

Figure 2-2: Normal energy diagram for a bulk metal emitter. As W increases, the barrier height seen by tunneling electrons decreases.

which predicts the magnitude of the ECD from the planar surface of a metal:

$$J_{FN}^{Elem}(F) = A\phi^{-1}F^2\exp\left[-\frac{B}{F}\phi^{3/2}\right] \tag{2.6}$$

where $A = e^3/8\pi h$ is known as the first FN constant.

Although the FN equation was derived from a basic physical model, it captures the qualitative characteristics of cold field emission, such as the emitted current density's quadratic dependence on the applied field in the pre-exponential factor and its $-1/F$ dependence in the exponent. In experimental studies of field emission, Fowler-Nordheim plots of $\ln[I/V^2]$ vs. $1/V$ are constructed using the measured I-V data. If it is assumed that I is linearly proportional to J and V is linearly proportional to F, an FN plot of field emission data should form a straight line. Aside from verifying that an electron emission process is due to field emission, FN plots can be used to extract the local work function (or field factor) by measuring the slope of a linear fit to the data: $m = -B\phi^{3/2}$. Figure 2-3 shows an FN plot and the extracted local work function, ϕ.

The standard form of the FN equation does not use the exact triangular potential barrier, but instead uses a triangular barrier rounded by an image potential. This is

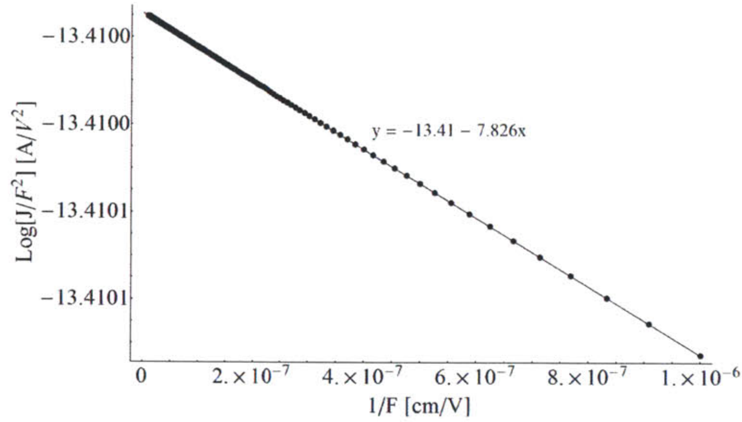

Figure 2-3: Fowler-Nordheim plot for an emitter with $\phi = 5$ eV. The linear fit y-intercept is equal to A and the slope is $-B\phi^{3/2}$.

known as the Schottky-Nordheim barrier [48] and is shown in Figure 2-4. The barrier

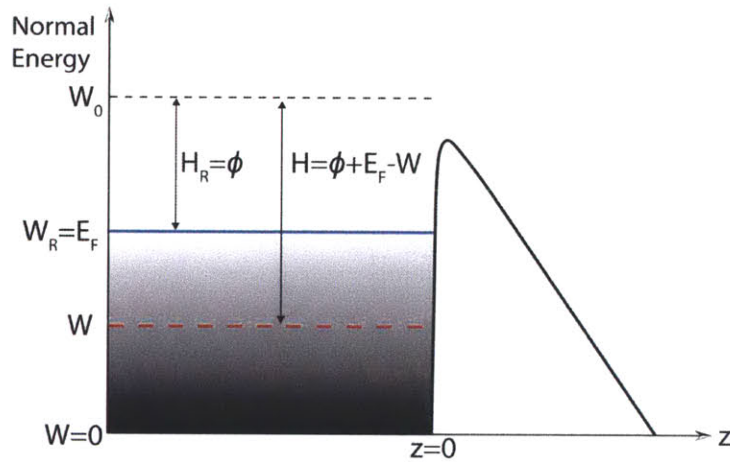

Figure 2-4: Normal energy diagram for a bulk emitter with the Schottky-Nordheim barrier potential.

potential then takes the form

$$V(F, z) = \frac{e}{16\pi\epsilon_0 z} - Fz \tag{2.7}$$

where ϵ_0 is the permittivity of free space. Substituting the potential from 2.7 into

Equation 2.3 yields a new form for the transmission function [49]

$$D(F,W) = \exp\left[-\frac{B}{F}\nu[y]H^{3/2}\right]. \tag{2.8}$$

Expanding D about $W = E_F$ gives an approximate transmission function

$$D(F,W) \simeq \exp\left[-\frac{B}{F}\phi^{3/2}\nu[y_{E_F}] + c(W - E_F)\right] \tag{2.9}$$

where [3, 50]

$$\begin{aligned}
c &= \frac{3B}{2F}t[y_{E_F}]\sqrt{\phi} \\
\nu[y] &= \frac{1}{\sqrt{2}}\left[1+\sqrt{1-y^2}\right]^{1/2}\left[E(k^2) - \frac{y^2K(k^2)}{1+\sqrt{1-y^2}}\right] \\
&\approx 1 - y^2 + \frac{1}{3}y^2\ln[y] \\
t[y] &= \nu[y] - \frac{2}{3}y\frac{d\nu[y]}{dy}. \\
&\approx 1 + \frac{1}{9}\left[y^2 - y^2\ln[y]\right] \\
k^2 &= \frac{2\sqrt{1-y^2}}{1+\sqrt{1-y^2}} \\
y &= \frac{\sqrt{e^3F/4\pi\epsilon_0}}{\phi + E_F - W},
\end{aligned} \tag{2.10}$$

$y_{E_F} = \sqrt{e^3F/4\pi\epsilon_0}/\phi$, $K(k^2)$ is the complete elliptic integral of the first kind, and $E(k^2)$ is the complete elliptic integral of the second kind. In general, these values must be calculated numerically, but good analytical approximations for ν and t exist via the work of Forbes, as listed above. The exact values for ν and t as functions of y are given in Table 2.1. Proceeding as in the case of deriving the elementary FN equation, integrating over all normal energies yields the standard Fowler-Nordheim

y	0	0.10	0.20	0.30	0.40	0.50	0.60	0.70	0.80	0.90	1
$\nu(y)$	1.000	0.982	0.937	0.872	0.789	0.690	0.577	0.450	0.312	0.161	0
$t(y)$	1.000	1.004	1.011	1.021	1.032	1.044	1.057	1.070	1.083	1.097	1.111

Table 2.1: Values for ν and t as functions of y [3].

equation [47]:

$$J_{FN}^{Stan}(F) = A\phi^{-1} t\left[y_{E_F}\right]^{-2} F^2 \exp\left[-\frac{B}{F}\nu\left[y_{E_F}\right]\phi^{3/2}\right] \tag{2.11}$$

As can be seen by looking at the values taken by ν and t, the incorporation of the image potential increases the transmission probability and emitted current density for a given applied field relative to the exact triangular barrier.

2.2 Fowler-Nordheim-Type Equations

While Fowler and Nordheim's results formed the foundation of the theory of field emission, their model was not complete. Due to non-ideal effects, the FN equation predicts ECDs that are significantly lower than experiments have shown for metal and semiconductor emitters [51]. To improve the accuracy of models for field emission, multiple correction terms have been appended to the standard FN equation to account for these non-idealities. This equation is known as the physically-complete Fowler-Nordheim equation:

$$J_{FN}^{PC}(F) = \lambda_T \lambda_B \lambda_P \lambda_\tau A\phi^{-1}\gamma_a^2 F^2 P \exp\left[-\frac{B}{\gamma_a F}\nu\phi^{3/2}\right] \tag{2.12}$$

where λ_T is a temperature correction factor, λ_B is the band structure correction factor, γ_a is a field enhancement factor, λ_P is a tunneling prefactor correction factor, λ_τ is a decay rate correction factor, P is the tunneling prefactor, and ν is a barrier-shape correction factor. The physics behind each of the correction factors is detailed below.

2.2.1 Temperature Correction Factor: λ_T

The standard Fowler-Nordheim equation is a result of taking the limit as $T \to 0$ K of the integrated product of the elementary charge, supply function, and transmission function. If this limit is not taken, the emitted current density is weakly dependent on temperature within the field emission regime. For a bulk emitter, the temperature correction factor to first order takes the form [47]

$$\lambda_T = \frac{\pi c k_B T}{\sin\left[\pi c k_B T\right]}. \tag{2.13}$$

Accordingly, when the limit as $T \to 0$ K is taken, λ_T evaluates to unity.

2.2.2 Band Structure Correction Factor: λ_B

By using the free electron mass and assuming spherical constant energy surfaces when deriving the Fowler-Nordheim equation, all band structure details specific to the emitter material are ignored. In actuality, the constant energy surfaces of a material are not spherical and are characterized by the shape of the conduction band minimum and valence band maximum. Many studies of varying levels of complexity and detail have investigated incorporating band structure effects into field emission calculations, ranging from directly calculating electron wave functions [52,53] to using the effective mass approximation [54]. For the purposes of this framework, an analytical method was desired and the approach of Stratton was chosen to address band structure effects.

Stratton was the first to incorporate band structure effects into field emission calculations, as part of a study of field emission from semiconductors. In his work, he assumes the emitter material has a spherical constant energy surface characterized by an isotropic effective mass m_n. Later, this treatment of band structure effects was generalized to include constant energy surfaces of arbitrary geometry, such as the one in Figure 2-5, by Gadzuk and Plummer [1]. Although comparatively simple, this

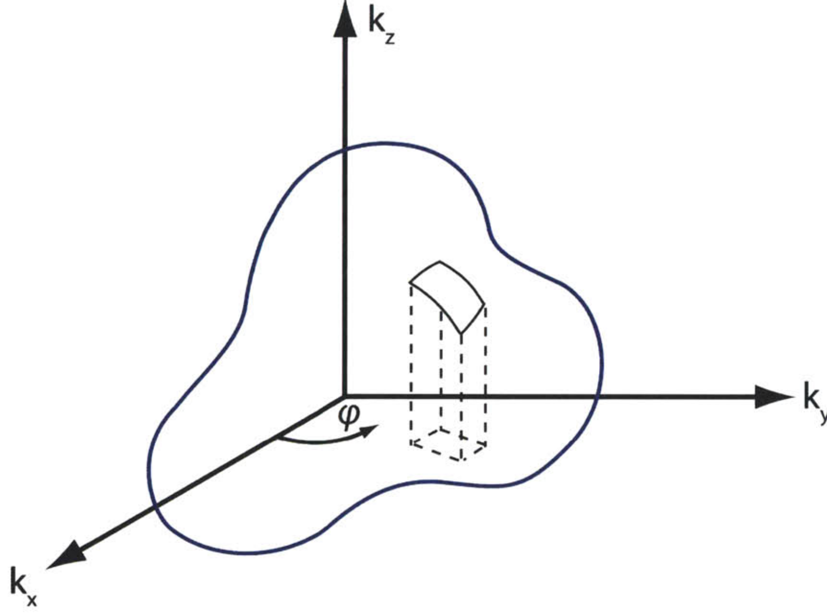

Figure 2-5: An example of a constant energy surface. This constant energy surface is being projected into the k_x-k_y plane, which is perpendicular to the emission direction. Figure adapted from [1].

approach has been used to reconcile qualitative discrepancies between experimental and theoretical total energy distributions from single emitters [55].

The energy of an electron is given by

$$E = \frac{\hbar^2 k_x^2}{2m_x} + \frac{\hbar^2 k_y^2}{2m_y} + \frac{\hbar^2 k_z^2}{2m_z} \tag{2.14}$$

where m_x, m_y, and m_z are the effective masses in the x, y, and z directions. A constant energy surface is generated by all points in k-space at which the sum of the energy components is equal to E. For the free electron constant energy surface, $m_x = m_y = m_z = m_0$, forming a spherical shell in k-space. However, electrons in semiconductors are often characterized by effective masses in the x, y, and z dimensions that are different from the free electron mass. Thus, for a given set of effective masses that

are not equal to m_0, the constant energy surface defined by the effective masses will be larger or smaller than the free electron constant energy surface in some regions, as shown in Figure 2-6. Since the volume enclosed by each of the constant energy surfaces represents the total number of electronic states contributing to the ECD, the volume between constant energy surfaces represents the excess number of electronic states that contribute to the free electron ECD, but should be omitted to calculate the ECD solely from the semiconductor. The goal of these band structure corrections is to calculate a correction ECD from states that lie between the free electron and emitter material's actual constant energy surfaces, then subtract it from or add it to the free electron ECD to obtain the ECD from the emitter.

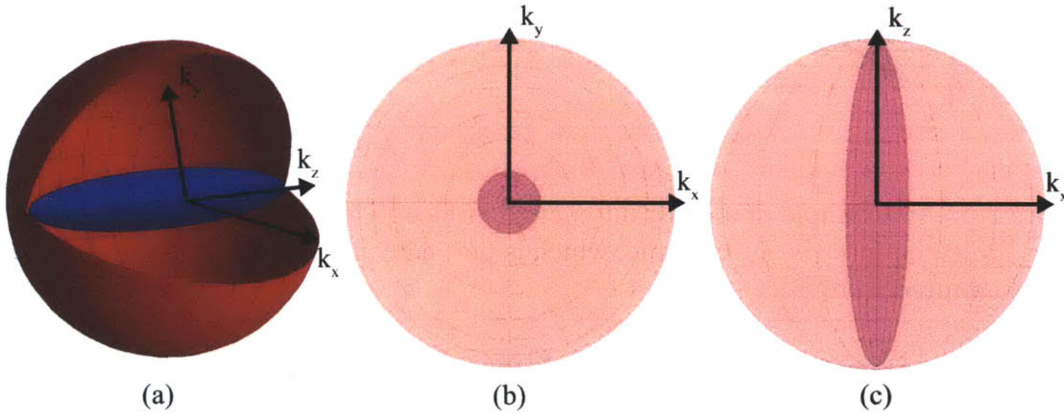

Figure 2-6: (a) Ellipsoidal constant energy surface with $m_0 > m_z > m_x = m_y$ (blue) compared to the free electron constant energy surface (red), (b) ellipsoidal and free electron constant energy surfaces projected into the $k_x - k_y$ plane, and (c) ellipsoidal and free electron constant energy surfaces projected into the $k_x - k_z$ plane.

Assuming that the momentum of the electrons is uncoupled between translational degrees of freedom, the electron energy can be split into normal energy W (k_z-direction) and transverse energy E_t (k_x-k_y plane). This separation of energies allows for the constant energy surfaces to be projected into the transverse plane and the integral over all k space to be separated into a transverse part and a normal part. For a given free electron energy E and polar angle ϕ in the transverse plane, there is a

maximum transverse k-vector and minimum transverse k-vector value that define the shape of the projected constant energy surface. The corrected ECD is calculated by integrating over all transverse k vectors and all free electron energies via the following equation [1]:

$$J(F,T) = \frac{e}{\pi h} \int_0^\infty f(E)\, dE \left[\int_0^{k_t(E)} D(E,k_t)\, k_t dk_t + (2\pi)^{-1} \right. \\ \left. \times \int_0^{2\pi} d\phi \left(\int_{k_t(E,0)}^{k_t(E,\phi)} - \int_{k_t^{min}(E,0)}^{k_t^{min}(E,\phi)} \right) D(E,k_t)\, k_t dk_t \right] \tag{2.15}$$

where e is the elementary charge and $D(E,k_t)$ is the transmission function. If considered in terms of the transverse energy, the integration is performed between a minimum effective mass (EM) transverse energy, $E_{t,EM,min}$, and some maximum transverse energy, $E_{t,EM,max}$. For free electrons (FE), the minimum transverse energy is $E_{t,FE,min} = 0$ and the maximum transverse energy possible at an energy E occurs when $W = 0$, leading to $E_{t,FE,max} = E$. In the transverse plane, the states that contribute to the free electron ECD are located between $E_t = 0$ and $E_t = E$, while states that contribute to the effective mass ECD are located between $E_{t,EM,min}$ and $E_{t,EM,max}$, which are functions of ϕ in general, as shown in Figure 2-7. When the true constant energy surface of the material is smaller (larger) than the free electron constant energy surface, electron states have been erroneously counted towards (omitted from) the actual ECD and must be subtracted from (added to) the free electron ECD as a correction term. For each free electron energy E and angle ϕ, there will be a discrepancy between the maximum transverse free electron energy and the maximum transverse effective mass electron energy. Since this energy is the difference between a total energy and a transverse energy, it can be considered to be a normal energy ΔW. When ΔW is positive, it is considered an energy surplus, while when ΔW is negative, it is deemed an energy deficit.

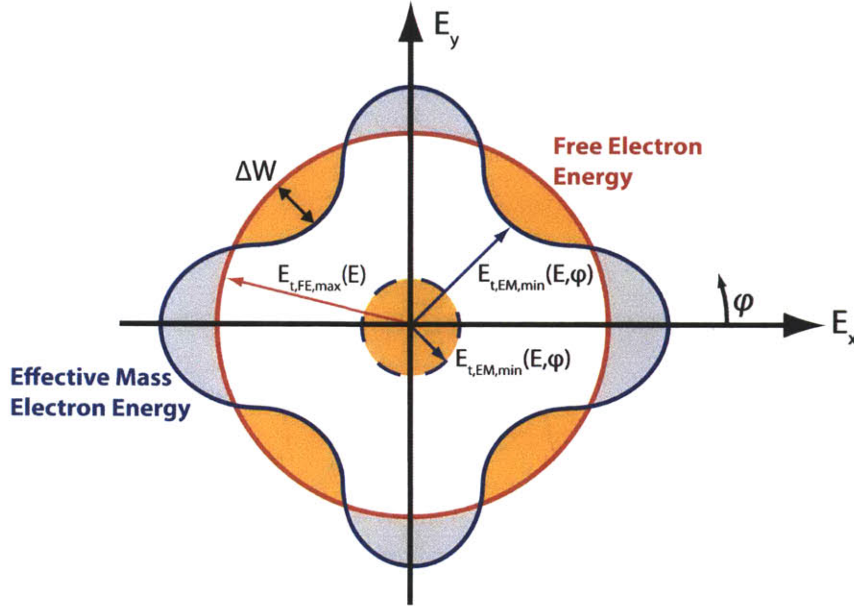

Figure 2-7: Actual and free electron constant energy surfaces projected into the E_x-E_y plane. The area inside the red (blue) contour represents electron states that contribute to the free electron (actual) ECD. Areas shaded gray (orange) are electron states that contribute to the actual (free electron) ECD, but are excluded by the free electron (actual) ECD. If the constant energy surface has a neck, it is projected as an absence of electronic states in the E_x-E_y plane and therefore is also shaded orange. Figure adapted from [1].

In order to proceed further in calculating the emitted current density, a specific material must be designated and the shape of its constant energy surfaces must be defined. Because the result of this particular calculation is used extensively in this thesis, the constant energy surfaces will be taken as spherical shells characterized by an isotropic effective mass m_n. Changing coordinates from k_t to E_t and taking into account that spherical constant energy surfaces are independent of ϕ, the ECD equation becomes

$$J\left(F,T\right) = e\frac{4\pi m_0}{h^3}\int_0^\infty dE\int_0^{E_m} dE_t\frac{D\left(E-E_t\right)}{1+\exp\left[\left(E-E_F\right)/k_BT\right]} \tag{2.16}$$

where $E_m = \left(m_n/m_0\right)E$ is the maximum value of $E_{t,EM}$ for a given value of E and E_F is the Fermi level. Making another variable change with $W = E - E_t$ and integrating

over E_t gives an equation of the form

$$J(F,T) = e\frac{4\pi m_0 k_B T}{h^3}\int_0^\infty dW \ln\left[1+\exp\left[\frac{E_F - W}{k_B T}\right]\right] \times \left\{D(W) - \left[1 - E_m'(W)\right] D(W - E_m(W))\right\} \tag{2.17}$$

where $E_m'(W)$ is the derivative of $E_m(W)$ with respect to W. The details of the variable substitution and integral transform are given in Appendix I of [54]. Inserting the expression for E_m above and defining $\gamma_n = 1 - (m_n/m_0)$ gives the equation for ECD with band structure corrections:

$$J(F,T) = e\frac{4\pi m_0 k_B T}{h^3}\int_0^\infty dW \ln\left[1+\exp\left[\frac{E_F - W}{k_B T}\right]\right]\{D(W) - \gamma_n D(\gamma_n W)\} \tag{2.18}$$

After specifying a form for the transmission coefficients and a value for the effective mass, an ECD equation can be derived. Factoring out all terms common to the Fowler-Nordheim equation gives a term of the form $\lambda_B = 1 - C$, where C includes the band structure effects.

2.2.3 Field Enhancement Factor: γ_a

Basic electrostatics dictates that the electric field at the surface of a cathode depends on its geometry. Rounded or pointed surfaces, such as the tips of field emitters, cause the electric field to be amplified at the apex relative to the surrounding applied field. Many models have been proposed for the field enhancement at the tip of a field emitter such as the ball-in-a-sphere model [27], hemisphere on a plane model [56], floating sphere between two plates model [31, 32], hemisphere on a post model [33, 38, 57], and hemi-ellipsoid on a plane model [31]. While the hemisphere on a post model is the most physically realistic for emission from thin whiskers, it comes at the cost of requiring numerical methods to evaluate the electric field at the emitter tip.

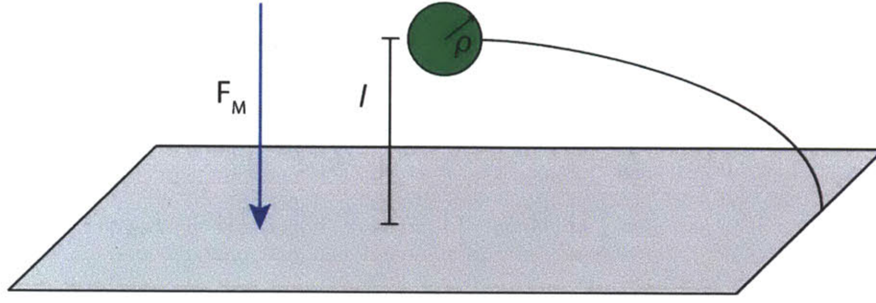

Figure 2-8: A schematic for the "floating sphere at emitter plane potential" model. The center of the sphere of radius ρ is located a distance l above the emitter plane. Far away from the sphere, the electric field is F_M, while at the apex of the sphere it is approximately $(3.5 + l/\rho)\, F_M$.

For emitters with large aspect ratios (emitter height to emitter width), the floating sphere at emitter plane potential model, shown in Figure 2-8, serves as a good semi-analytical approximation. In this model, the emitter tip is taken as a sphere that is floating in space above an emitter plane. The sphere is held at a uniform potential equal to that of the emitter plane below it. The field enhancement factor at the apex of the sphere is found to be [31]

$$\gamma_a = 3.5 + \frac{l}{\rho} \tag{2.19}$$

where l is the height of the center of the sphere above the emitter plane and ρ is the radius of curvature at the emitter tip.

2.2.4 Tunneling Prefactor and Correction Factor: P and λ_P

The form of the JWKB approximation appropriate for deriving the transmission function is dependent upon the shape of the potential barrier. The most mathematically rigorous and exact of these forms was derived by Fröman and Fröman (FF) in the 1960s [58]:

$$D\,(P, G) = \frac{P \exp\left[-G\right]}{1 + P \exp\left[-G\right]} \tag{2.20}$$

where P is the tunneling prefactor and G is the JWKB exponent given by

$$G = g_0 \int M(z)^{1/2} dz \tag{2.21}$$

with $g_0 = 4\pi(2m_0)/h$, $M = U(z) - W$, and $U(z)$ being the specific form of the $1D$ barrier potential. The integration is performed over all positive values of M, between the classical turning points of the electron. This expression for the transmission function is general and all other forms of transmission functions from JWKB approximations can be obtained from it by employing the proper approximations [59].

The validity of the approximations made to the FF JWKB expression is qualified by the shape of the potential barrier. Barrier shapes are classified as either *weak* ($e^{-G} \sim 1$) or *strong* ($e^{-G} \ll 1$) and *ideal* ($P = 1$) or *non-ideal* ($P \neq 1$) [59]. The form of the JWKB expression used in deriving the standard FN equation [47] corresponds to that of a strong, ideal barrier potential and is given by the "simple JWKB" form

$$D(G) = \exp[-G]. \tag{2.22}$$

However, according to Forbes [59], the exact triangular barrier (along with others) is not an ideal barrier potential and $P \neq 1$. In the limit of the strong barrier regime, the proper form of the transmission function should be that proposed by Landau and Lifschitz (LL) [60]. The LL formula is the simple JWKB expression with the addition of a tunneling prefactor

$$D(P,G) = P\exp[-G]. \tag{2.23}$$

In general, the tunneling prefactor depends on the normal energy and after integration over all normal energies produces a correction factor λ_P that is dependent upon the form of P. For barriers with exact, analytical solutions for the electron transmission probability, P can be calculated by determining the transmission probability

and making approximations (usually strong barrier) to arrive at an expression with the form of the LL formula. This procedure has been carried out for the rectangular barrier, exact triangular barrier, parabolic barrier, and Eckert barrier [59]. For potential barrier shapes without analytical transmission probability solutions, P must be determined numerically.

2.2.5 Barrier Shape and Decay Width Correction Factors: ν and λ_τ

If nearly-triangular potential barrier shapes are used instead of the exact triangular barrier, they can be incorporated into FN theory by way of a barrier shape correction factor, ν. One of the most common potential barrier shapes used is the Schottky-Nordheim barrier [48] shown in Figure 2-4 and given by Equation 2.7. Using this potential barrier, the barrier shape correction factor takes the form $\nu[y]$ as derived in the standard Fowler-Nordheim equation above [49]. When a transmission function incorporating ν is expanded about a particular normal energy, it generates an additional correction term that is grouped with decay rate, c. After the final integration step over all normal energies in deriving the ECD equation, this additional term, called the decay rate correction factor, appears in the pre-exponential factor and is denoted by λ_τ. In the standard FN equation, $\lambda_\tau = t^{-2}\left[\sqrt{e^3F/4\pi\epsilon_0}/\phi\right]$.

2.3 Emission from Semiconductors

When treating field emission from metals, electrons are emitted from the conduction band and the majority of them have energies close to the Fermi level, which is positive with respect to the conduction band edge. In the case of semiconductor emitters, the Fermi level may be negative with respect to the conduction band edge and emission also occurs from states in the valence band. Stratton was the first to address the

topic of emission from semiconductors [61], providing treatments of emission from the conduction band for positive and negative Fermi levels and emission from the valence band [54,62].

The major difference between these emission cases is the energy level from which the majority of the electrons are emitted and as a result, the energy level about which the transmission coefficients are expanded via Taylor series. The transmission function for emission from bulk semiconductors takes the form [54]

$$D(F,W) = \exp\left[-\frac{4}{3}\frac{\sqrt{2m_0}}{\hbar}\frac{(\phi+E_F-W)^{3/2}}{F}\nu\left[v\frac{\sqrt{e^3F/4\pi\epsilon_0}}{\phi+E_F-W}\right]\right]. \tag{2.24}$$

W is the electron energy in the direction of emission, ν is the Schottky-Nordheim barrier shape correction factor, and $v = \sqrt{(\epsilon_s-1)/(\epsilon_s+1)}$, with ϵ_s being the dielectric constant of the semiconductor. A more convenient form for performing the required expansions on the transmission coefficients that will be used in each of the cases below is

$$D(F,W) = \exp\left[-\frac{U^{1/2}(\phi+E_F-W)^{3/2}}{\psi_i^2}\nu\left[\frac{\psi_i}{\phi+E_F-W}\right]\right]. \tag{2.25}$$

where

$$\begin{aligned} U &= \frac{32}{9}\frac{m_0e^4}{\hbar^2}v^4 \\ \psi_i &= v\sqrt{\frac{e^3F}{4\pi\epsilon_0}} \end{aligned} \tag{2.26}$$

2.3.1 Emission from the Conduction Band for $E_F > 0$

Emission from semiconductors with a Fermi level above the edge of the conduction band is treated in the same manner as emission from metals. Just like in a metal, the majority of emitted electrons have energies that are close to the Fermi level, as shown in Figure 2-9. Stratton gives the transmission coefficients expanded about $E_F > 0$

as:

$$D(F, W) = \exp\left[-b_1 + c_1 (W - E_F)\right] \tag{2.27}$$

where

$$\begin{aligned} b_1 &= U^{1/2}\phi^{3/2}\nu\left[\frac{\psi_i}{\phi}\right]/\psi_i^2 = \frac{B}{F}\nu\left[\frac{v}{\phi}\sqrt{\frac{e^3F}{4\pi\epsilon_0}}\right]\phi^{3/2} \\ c_1 &= \frac{3}{2}U^{1/2}\phi^{1/2}t\left[\frac{\psi_i}{\phi}\right]/\psi_i^2 = \frac{3B}{2F}t\left[\frac{v}{\phi}\sqrt{\frac{e^3F}{4\pi\epsilon_0}}\right]\phi^{1/2} \end{aligned} \tag{2.28}$$

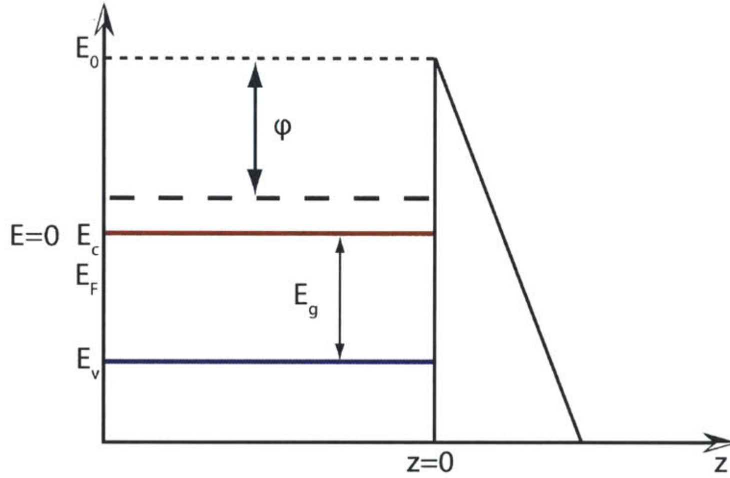

Figure 2-9: When the Fermi energy of a semiconductor emitter is located above the conduction band edge, most emitted electrons come from states close in energy to the Fermi energy. These electrons see a barrier height equal to the work function of the semiconductor, ϕ.

Multiplying the transmission coefficients by the supply function (Equation 2.2) and the elementary charge and integrating over all normal energies gives the emitted current density from the conduction band of a semiconductor with $E_F > 0$ for the free electron mass:

$$j_{c0}(F, T) = A\exp\left[-b_1\right] H_1\left(c_1 k_B T, E_F/k_B T\right). \tag{2.29}$$

where

$$H_1\left(c_1 k_B T, E_F/k_B T\right) = \left(c_1 k_B T\right)^{-2}\left[\frac{\pi c_1 k_B T}{\sin\left[\pi c_1 k_B T\right]} - \exp\left[-c_1 E_F\right]\left(1 + c_1 E_F\right) - \left(c_1 k_B T\right)^2\right]\exp\left[-c_1 E_F\right]\sum_{n=1}^{\infty}\frac{(-1)^{-1}\exp\left[-nE_F/k_B T\right]}{n\left(n + c_1 k_B T\right)} \quad (2.30)$$

and $A = e4\pi m_0 \left(k_B T\right)^2/h^3$. In order to make corrections for the effective mass, the expansion coefficients for $D\left(\gamma_n W\right)$ must be determined. Inserting $\gamma_n W$ for W in Equation 2.25 and factoring out $\gamma_n^{3/2}$ allows for the transmission coefficients to be expanded about W. Expanding about $W = E_F$ and rearranging gives the coefficients for the effective mass correction:

$$\begin{aligned} b_1^{'} &= \bar{b_1} \\ c_1^{'} &= \gamma_n \bar{c_1} \end{aligned} \quad (2.31)$$

where a bar over the variable indicates that ϕ should be replaced by an effective work function $\phi^{'} = \left[\phi + \left(1 - \gamma_n\right) E_F\right]/\gamma_n$. Substituting these coefficients into the transmission function and following the same procedure as above for calculating the ECD from a semiconductor with $E_F > 0$ gives the ECD correction due to the effective mass:

$$j_c^{'}(F,T) = -A\gamma_n \exp\left[-\bar{b_1}\right] H_1\left(\gamma_n \bar{c_1} k_B T, E_F/k_B T\right) \quad (2.32)$$

The total corrected ECD is given by

$$\begin{aligned} j_c(F,T) = &A\left\{\exp\left[-b_1\right] H_1\left(c_1 k_B T, E_F/k_B T\right)\right. \\ &\left.-\gamma_n \exp\left[-\bar{b_1}\right] H_1\left(\gamma_n \bar{c_1} k_B T, E_F/k_B T\right)\right\}. \end{aligned} \quad (2.33)$$

Noting that $\exp\left[-c_1 E_F\right] \ll 1$, the above equation can be simplified to

$$j_c(F,T) = e\frac{4\pi m_0}{h^3}\left\{c_1^{-2}\frac{\pi c_1 k_B T}{\sin\left[\pi c_1 k_B T\right]}\exp\left[-b_1\right] - \bar{c}_1^{-2}\frac{\pi \gamma_n \bar{c}_1 k_B T}{\sin\left[\pi \gamma_n \bar{c}_1 k_B T\right]}\exp\left[-\bar{b}_1\right]\right\} \tag{2.34}$$

2.3.2 Emission from the Conduction Band for $E_F < 0$

When $E_F < 0$, the Fermi level is located in the forbidden energy gap of the semiconductor and no electrons may occupy states at E_F. The closest occupied electron states to the Fermi level are located at the bottom of the conduction band and the majority of emitted electrons come from these states, as shown in Figure 2-10. Therefore, the transmission coefficients should be expanded about $W = 0$, giving

$$D(F,W) = \exp\left[-b_0 + c_0 W\right] \tag{2.35}$$

where

$$\begin{aligned} b_0 &= U^{1/2}(\phi + E_F)^{3/2}\frac{\nu\left[\psi_i/\chi_e\right]}{\psi_i^2} = \frac{B}{F}\nu\left[\frac{v}{\chi_e}\sqrt{\frac{e^3 F}{4\pi\epsilon_0}}\right]\chi_e^{3/2} \\ c_0 &= 3/2U^{1/2}\chi_e^{1/2}\frac{t\left[\psi_i/\chi_e\right]}{\psi_i^2} = \frac{3B}{2F}t\left[\frac{v}{\chi_e}\sqrt{\frac{e^3 F}{4\pi\epsilon_0}}\right]\chi_e^{1/2} \end{aligned} \tag{2.36}$$

and χ_e is the electron affinity of the semiconductor. Proceeding to calculate the ECD as above, the ECD for the free electron mass evaluates to

$$j_{c0}(F,T) = A\exp\left[-b_0 + \frac{E_F}{k_B T}\right]\sum_{n=0}^{\infty}\frac{(-1)^n \exp\left[\frac{nE_F}{k_B T}\right]}{(n+1)(n+1+c_0 k_B T)}. \tag{2.37}$$

Retaining only the first term, recognizing that $1 \gg c_0 k_B T$, and using the relation between the Fermi energy and the electron density n, gives a simplified form of the

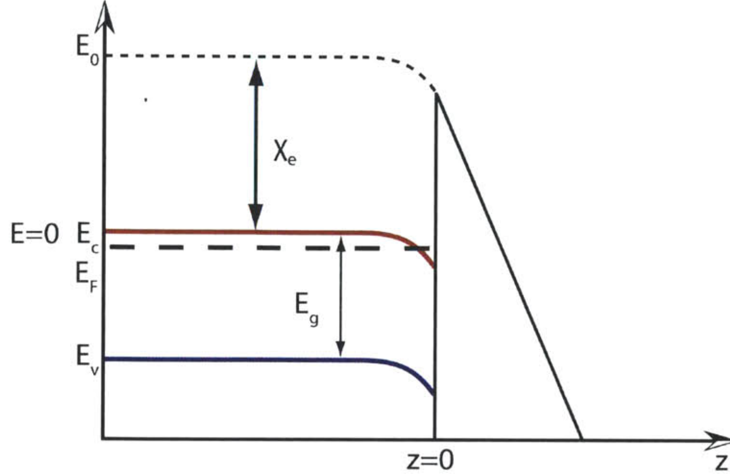

Figure 2-10: When the Fermi energy of the semiconductor is below the conduction band edge, most emitted electrons come from states close in energy to the edge of the conduction band. This presents a barrier height equal to the electron affinity of the semiconductor, χ_e.

ECD for the free electron mass for $E_F < 0$, valid when $-E_F/k_BT \gg 1$:

$$j_{c0}(F,T) \simeq en\sqrt{\frac{k_BT}{2\pi m_0}}\exp\left[-b_0\right] \tag{2.38}$$

The effective mass correction for this case only requires that c_0 be replaced by $\gamma_n c_0$. The ECD correction due to the effective mass is

$$j_c'(F,T) \simeq -\gamma_n en\sqrt{\frac{k_BT}{2\pi m_0}}\exp\left[-b_0\right] \tag{2.39}$$

and the total, corrected ECD is then

$$j_c(F,T) \simeq en\left(1-\gamma_n\right)\sqrt{\frac{k_BT}{2\pi m_0}}\exp\left[-b_0\right] \tag{2.40}$$

It should be noted that Stratton's equations for emission from semiconductors with $E_F < 0$ ignore the effects of band-bending and the formation of an accumulation layer of electrons near the surface of the semiconductor. Thus, the above equation

is not physically realistic. It is suspected that the total ECD from semiconductor emitters with$E_F < 0$ far from the surface is approximately the sum of the current from extended states and bound states in the accumulation layer as developed in the subsections below [2]. Alternatively, including band bending and the formation of an accumulation layer leads to a modified version of the Fowler-Nordheim equation with the work function reduced by the difference between the total amount of conduction band bending and the Fermi energy, which may be more physically realistic than Stratton's work in describing emission from extended states [63]. Analytical methods for treating band bending and electrons tunneling from an accumulation layer through a triangular barrier are presented in §2.3.4 and §2.3.5.

2.3.3 Emission from the Valence Band for $E_{Fv} < 0$

Emission from the valence band requires that the energy coordinates used for emission from the conduction band be modified. For these calculations, E_v, W_v, and E_{tv} are the negative total energy, normal energy, and transverse energy of the electron as measured downward from the top of the valence band, with $E_v = W_v - E_{tv}$. E_{Fv} is the negative Fermi level with respect to the valence band edge and is defined such that $E_F + E_{Fv} = -E_g$. In order to account for this change of variables in the transmission coefficients, W must be replaced by $-W_v - E_g$ where E_g is the energy gap of the semiconductor. This gives transmission coefficients of the form

$$D_v(F, W_v) = \exp\left[-\frac{4}{3}\frac{\sqrt{2m_0}}{\hbar}\frac{(\chi_e + E_g + W_v)^{3/2}}{F}\nu\left[\frac{v}{\chi_e + E_g + W_v}\sqrt{\frac{e^3 F}{4\pi\epsilon_0}}\right]\right]. \quad (2.41)$$

Making the proper substitutions for the energies in the Fermi-Dirac distribution gives a form appropriate for emission from the valence band:

$$f_v(W_v, E_{tv}) = \frac{1}{1 + \exp\left[-\frac{W_v - E_{tv} - E_{Fv}}{k_B T}\right]} \quad (2.42)$$

Integrating the product of f_v and the density of states over all transverse energies gives the supply function for emission from the valence band:

$$N_v(W_v) = \frac{4\pi m_0 k_B T}{h^3} \ln\left[1 + \exp\left[\frac{W_v - E_{Fv}}{k_B T}\right]\right] \tag{2.43}$$

Using these definitions, an equation for calculating the effective-mass-corrected ECD from the valence band can be derived, analogous to Equation 2.18 for the conduction band [62].

$$\begin{aligned} j_v(F,T) = &L\left[\int_0^{E_V} dW_v \ln\left[1 + \exp\left[\frac{W_v - E_{Fv}}{k_B T}\right]\right]\right. \\ &\times \left\{D_v(W_v) - \left[1 + E'_{vm}(W_v)\right] D_v\left(W_v + E_{vm}(W_v)\right)\right\} \\ &\left.+\ln\left[1 + \exp\left[\frac{E_V - E_{Fv}}{k_B T}\right]\right] \int_{E_V}^{E_{mv}(E_V)+E_V} D_v(W_v)\, dW_v\right] \end{aligned} \tag{2.44}$$

where E_V is the bandwidth of the valence band and E_{vm} is the maximum value of E_{tv} for a given value of E_v. For spherical constant energy surfaces, $E_{mv}(E_v) = (m_p/m_0)\, E_v$ where m_p is the hole effective mass at the top of the valence band. Seeing as no electronic states in the band gap may be occupied and D_v increases with decreasing W_v, the majority of electrons should be emitted from energy states close in energy to the valence band edge when $E_{Fv} < 0$ (Fermi level is above the valence band edge), as seen in Figure 2-11. Thus, D_v is expanded about $W_v = 0$, giving the transmission coefficients for emission from the valence band as

$$D_v(W_v) \simeq \exp\left[-b_v - c_v W_v\right] \tag{2.45}$$

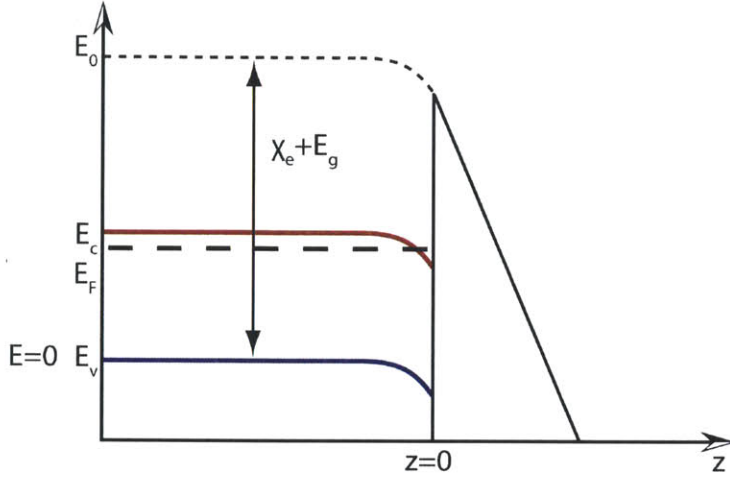

Figure 2-11: For emission from the valence band, the majority of emitted electrons have energies close to the valence band edge. The barrier to transmission is the sum of the semiconductor's electron affinity, χ_e, and band gap energy, E_g.

with b_v and c_v defined as follows:

$$b_v = U^{1/2}(\chi_e + E_g)^{3/2}\nu\left[\psi_i/\left(\chi_e + E_g\right)\right]/\psi_i^2 = \frac{B}{F}\nu\left[\frac{v}{\chi_e + E_g}\sqrt{\frac{e^3 F}{4\pi\epsilon_0}}\right]\left(\chi_e + E_g\right)^{3/2}$$

$$c_v = 3/2U^{1/2}(\chi_e + E_g)^{1/2}t\left[\psi_i/\left(\chi_e + E_g\right)\right]/\psi_i^2 = \frac{3B}{2F}t\left[\frac{v}{\chi_e + E_g}\sqrt{\frac{e^3 F}{4\pi\epsilon_0}}\right]\left(\chi_e + E_g\right)^{1/2} \tag{2.46}$$

Integrating over the product of the elementary charge, supply function, and transmission coefficients gives the ECD from the valence band for the free electron mass, when $E_{Fv} < 0$:

$$\begin{aligned} j_{v0}\left(F, T\right) = {} & e\frac{4\pi m_0 \left(k_B T\right)^2}{h^3}\exp\left[-b_v\right] \\ & \times\left[\left(c_v k_B T\right)^{-2} + \exp\left[E_{Fv}/k_B T\right] H_0\left(-c_v k_B T, E_{Fv}/k_B T\right)\right] \end{aligned} \tag{2.47}$$

Modifying the transmission coefficients for the effective mass correction requires that c_v be replaced by $\gamma_v c_v$:

$$j_v'(F,T) = -e\frac{1}{\gamma_v}\frac{4\pi m_0 (k_B T)^2}{h^3}\exp[-b_v] \times \left[(c_v k_B T)^{-2} - \gamma_v \exp\left[\frac{E_{Fv}}{k_B T}\right] H_0(-\gamma_v c_v k_B T, E_{Fv}/k_B T)\right] \tag{2.48}$$

where $\gamma_v = 1+(m_p/m_0)$. The total, corrected ECD from the valence band for $E_{Fv} < 0$ is

$$j_v(F,T) = e\frac{4\pi m_0 (k_B T)^2}{h^3}\exp[-b_v]\left[\left(1-\frac{1}{\gamma_v}\right)(c_v k_B T)^{-2} + \exp\left[\frac{E_{Fv}}{k_B T}\right]\{H_0(-c_v k_B T, E_{Fv}/k_B T) - \gamma_v H_0(-\gamma_v c_v k_B T, E_{Fv}/k_B T)\}\right] \tag{2.49}$$

When $E_{Fv}/k_B T \ll -1$, the equation simplifies to

$$j_v(F,T) = e\frac{4\pi m_0}{h^3} c_v^{-2}\left(1-\frac{1}{\gamma_v}\right)\exp[-b_v] \tag{2.50}$$

2.3.4 Field Penetration and Band Bending

When an electric field is applied to the surface of a solid, charges in the solid rearrange to set up an internal electric field that opposes the direction of the applied field. In the case of metals, the electron density is extremely large and the applied field is negated very close to the metal-vacuum interface. Semiconductors, however, have a much lower charge density that is set by the dopant concentration, allowing the applied field to penetrate to an appreciable depth. In the case of field emission, this results in an accumulation layer of electrons at the semiconductor-vacuum interface, which is depicted by the conduction band bending downwards in energy band diagrams, as in Figure 2-12.

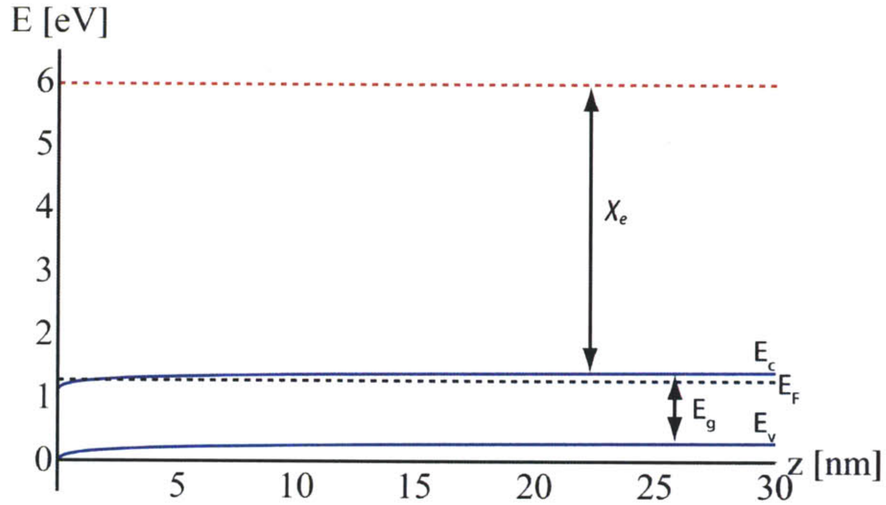

Figure 2-12: For $F = 5 \times 10^7 V/cm$, $N_D = 10^{17} cm^{-3}$, and $T = 300$ K, the magnitude of the band bending in silicon is approximately $\Delta\phi = 0.259eV$.

Band bending in semiconductors has been treated in general by Tsong [64] and for cases relevant to field emission by Stratton [54] and Gomer [63]. All of these treatments are numerical in nature, requiring repeated integrations over tabulated functions to obtain the electric field in the space charge region, the semiconductor potential, and the surface potential. Seeing as the focus of this work is an analytical treatment of field emission from quantum-confined emitters, analytical expressions for parameters related to band-bending are desired. Expressions of this nature can be obtained by making the assumption that band bending is only significant for non-degenerate semiconductors, which allows for the use of Maxwell-Boltzmann statistics for electrons [4]. For an n-type semiconductor, the band-bending parameters are as

follows:

$$
\begin{aligned}
F(z) &= -\sqrt{\frac{2N_D k_B T}{\epsilon_s}}\ln\left[\frac{z}{\sqrt{2}L_D} + \frac{1}{F_{vac}\frac{\epsilon_0}{\epsilon_s}\sqrt{\frac{\epsilon_s}{2N_D k_B T}}}\right] \\
\phi(z) &= -\frac{2k_B T}{e}\ln\left[\frac{z}{\sqrt{2}L_D} + \frac{1}{F_{vac}\frac{\epsilon_0}{\epsilon_s}\sqrt{\frac{\epsilon_s}{2N_D k_B T}}}\right] \\
F_s &= \frac{\epsilon_0}{\epsilon_s}F_{vac} \\
\phi_s &= \frac{2k_B T}{e}\ln\left[F_{vac}\frac{\epsilon_0}{\epsilon_s}\sqrt{\frac{\epsilon_s}{2N_D k_B T}}\right] \\
z_{acc} &\simeq \sqrt{2}L_D
\end{aligned}
\tag{2.51}
$$

where x_{acc} is the approximate width of the accumulation layer, F_{vac} is the applied electric field in vacuum, F is the electric field in the semiconductor, ϕ is the potential in the semiconductor, ϕ_s and F_s are the potential and electric field at the surface of the semiconductor, and $L_D = [\epsilon_s k_B T/(e^2 N_D)]^{1/2}$. These equations are valid when $\phi \gg k_B T/e$, which is satisfied for fields relevant to field emission applied to a non-degenerate semiconductor. The details of the band-bending derivation are located in Appendix A.

2.3.5 Tunneling from an Accumulation Layer

Band bending and the formation of an accumulation layer of electrons near the surface of the semiconductor can play a major role in determining the emitted current density. Due to the accumulation layer, the concentration of electrons at the surface of the semiconductor is much higher than it is in the bulk. In addition, the sharp change in carrier concentration close to the surface acts as a confining potential, keeping the electrons in the accumulation layer and separating them into subbands [2]. If the potential well is wide enough to allow for a bound state, as shown in Figure 2-13, electrons in this state will contribute to the tunneling current through the

barrier. This effect was studied in the case of electrons tunneling through a thin gate oxide from an accumulation layer in a MOSFET by Rana et al. [2]. Due to the oxide presenting a triangular potential barrier to tunneling electrons, this work is also directly applicable to field emission from semiconductors.

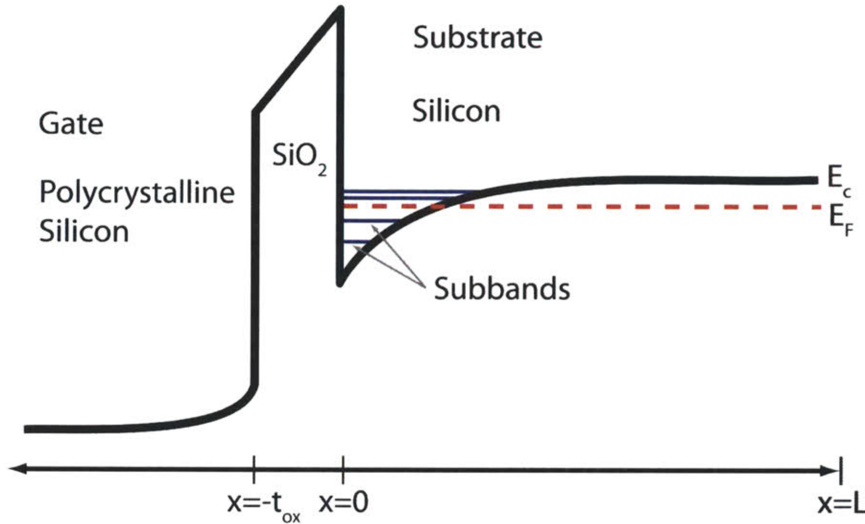

Figure 2-13: Band bending near the surface of a semiconductor leads to the formation of an accumulation layer and quasi-bound, discrete electronic states. In a MOS structure, the electrons in the accumulation layer can tunnel through the thin oxide layer from the substrate into the gate, leading to a current across the oxide layer. Figure adapted from [2].

The total emitted current density from a semiconductor with an accumulation layer is the sum of the current from the extended states and current from the bound states.:

$$J_{total} = J_{extended} + J_{bound} \tag{2.52}$$

The emitted current density from extended states is given by Equation 2.40, while the emitted current density from bound states must be calculated differently, as transmission probability through the barrier is not a meaningful concept for bound states. Instead, the approximate lifetime of the bound states should be used to determine

the emission current:

$$\frac{1}{\tau_n(E_t)} = \frac{T(E)}{\int_0^{z_n} \sqrt{2m_z/[E_n - E_c(z)]}\,dz} \tag{2.53}$$

where τ_n is the lifetime of the state, $T(E)$ is the transmission probability, E is the total energy, m_z is the effective mass in the emission direction, E_n is the subband energy for the state, x_n is the classical turning point for the nth bound state, and E_c is the conduction band edge as a function of position. The inverse of the state lifetime gives the rate of attempts at tunneling through the barrier, in the nth subband. Multiplying this by the number of electrons in the inversion layer and summing over all subbands in the well gives the bound state emitted current density [65]:

$$J_{bound} = e\left(\frac{k_BT}{\pi\hbar^2}\right)\sum_n \frac{1}{\tau_n(E)}\delta_n m_z \ln\left[1+\exp\left[\frac{E_F-E_n}{k_BT}\right]\right] \tag{2.54}$$

where δ_n is the Kronecker delta function.

2.4 Emission from Quantum-Confined Emitters

Recently, a few treatments of field emission from quantum-confined structures have been developed. Spurred mainly by the abundance of field emission data from graphene and no suitable ECD equations for analysis, the following treatments pertain to emission from quasi-two-dimensional systems.

2.4.1 Emission from a Nanowall Edge

In 2010, Qin et al. derived approximate, analytical equations appropriate for describing the emitted line current density from the edge of a nanowall emitter at $T = 0$ K [41]. As illustrated in Figure 2-14, a nanowall is a nanoscale, upright, blade-like structure with a length and height that are very large when compared to its width.

Aside from the incorporation of quantum confinement effects, the model employed in this study is identical to that used in deriving the elementary Fowler Nordheim equation. The major difference between the nanowall and a bulk emitter is that the

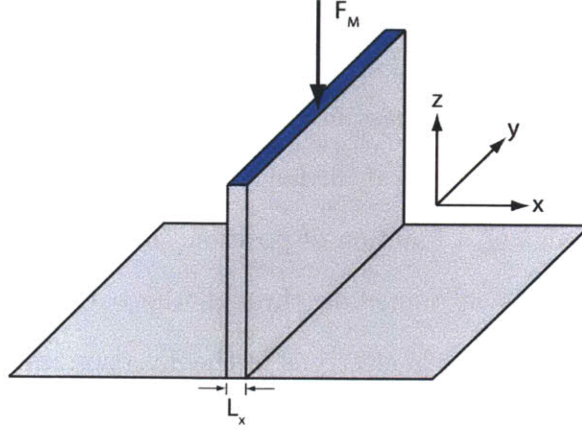

Figure 2-14: Illustration of a nanowall emitter and the relative sizes of its dimensions. The structure is absolutely small in the x direction and has a quantum well width L_x in that dimension. The electric field F_M is applied from the z direction.

nanowall is transversally quantum-confined in one dimension (x dimension). Consequently, the electron energies in the x dimension are discretized and separate the electrons into subbands. These discrete energies are assumed to take the form of those of the infinite square well, given by

$$E_n = \frac{n^2 h^2}{8 m_0 L_x^2} \tag{2.55}$$

where n is the "vibrational level" and subband index of the electrons and L_x is the width of the nanowall in the x direction, or the transverse well width. Accordingly, the energy of an electron in the emitter takes the form $E = W + E_t = W + E_n + p_y^2/2m_0$.

The supply function is calculated per subband of electrons, each of which have a 2D density of states. Integrating the product of the Fermi-Dirac distribution, transverse density of states, and electron group velocity in the emission direction, z, gives the

line supply function

$$N_n(W,T) = \frac{2}{h^2}\int_{-\infty}^{\infty} \frac{1}{1+\exp\left[\frac{W+\frac{p_y^2}{2m_0}+E_n}{k_BT}\right]}dp_y \tag{2.56}$$

where W is the normal energy, f_n is the Fermi-Dirac distribution, and p_y is the electron momentum in the y direction. This integral has no known analytical solution, so the evaluation of the line supply function is not possible at this point.

The presence of transverse quantum confinement in the emitter also affects the transmission function. It is convenient to define an emission reference level (ERL) [66], which is the normal electron state which has the maximum tunneling probability per subband. In the case of a bulk metal emitter at $T = 0$ K, there exists an electronic state for which $E = E_F$, $E_t = 0$, and $W = E_F$. This is the ERL for a bulk emitter. For the nanowall, there exists a state in which $E = E_F$, however, there is no state with $E_t = E_n + p_y^2/2m_0 = 0$ due to the restriction of E_n being a discrete, positive value. Therefore, the ERL for a given subband of the nanowall emitter is $W_{ERL} = E_F - E_n$.

The introduction of the ERL allows for the definition of a reference zero-field barrier height, H_R, which denotes the barrier height seen by an electron occupying the state at the ERL in each subband. For the nanowall, the lower-energy ERL results in a higher reference barrier height, $H_R = \phi + E_F - W_{ERL} = \phi + E_n$ than for a bulk emitter. As a result, each electronic state in the nanowall emitter has a lower probability of tunneling through the potential barrier than in the bulk emitter case. The relation between the ERL and H_R is shown in the normal energy diagram for the nanowall in Figure 2-15. The same general form of the transmission function used in deriving the FN equation (Equation 2.4) is also applicable in this case. Assuming that the majority of the emitted electrons come from energy states near the ERL, H can be expanded about H_R (identical to expanding W about W_{ERL}) to the first

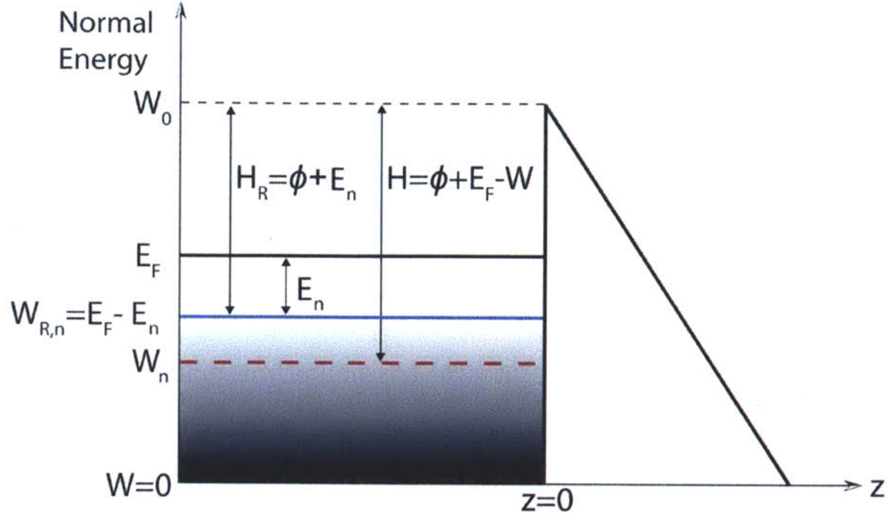

Figure 2-15: Normal energy diagram for a nanowall emitter. The presence of transverse quantum confinement decreases the ERL in each subband and increases the reference zero-field barrier height relative to a bulk emitter.

order, giving a transmission function of the form

$$D\left(F,W\right)=\exp\left[-\frac{B}{F}H_R^{3/2}\right]\exp\left[-c_R\left(H-H_R\right)\right]. \tag{2.57}$$

B is the second FN constant and $c_R=3B\sqrt{H_R}/2F$ is the transmission function decay rate at the ERL. Integrating the product of Equation 2.56 and Equation 2.57 from $W=-\infty$ to $W=\infty$ and multiplying by the elementary charge gives the emitted line current density from a single electron subband [41]:

$$J_n^{nw}\left(F\right)=e\frac{2}{h^2}\sqrt{2\pi m_0}c_n^{-3/2}\exp\left[-\frac{B}{F}\left(\phi+E_n\right)^{3/2}\right] \tag{2.58}$$

where n is the electron subband index and $c_n=3B\sqrt{\phi+E_n}/2F$. The total emitted current density is found by summing over all electron subbands in the emitter and dividing by the transverse well width L_x:

$$J_n^{nw}\left(F\right)=e\frac{2}{L_x h^2}\sqrt{2\pi m_0}\sum_n c_n^{-3/2}\exp\left[-\frac{B}{F}\left(\phi+E_n\right)^{3/2}\right] \tag{2.59}$$

2.4.2 Emission from a Thin Slab

The case of field emission from a quasi-2D structure which is quantum confined in the direction of emission was studied by Forbes [67]. The "thin slab" is a structure which is absolutely and relatively small in the direction of emission and large in dimensions transverse to the emission direction, as shown in Figure 2-16. Electrons in the emitter see an infinite potential outside the rear surface of the thin slab and a rounded triangular potential outside the emitting surface. In this treatment, the thin slab is assumed to be a single atomic layer thick, consistent with the thickness of a graphene sheet.

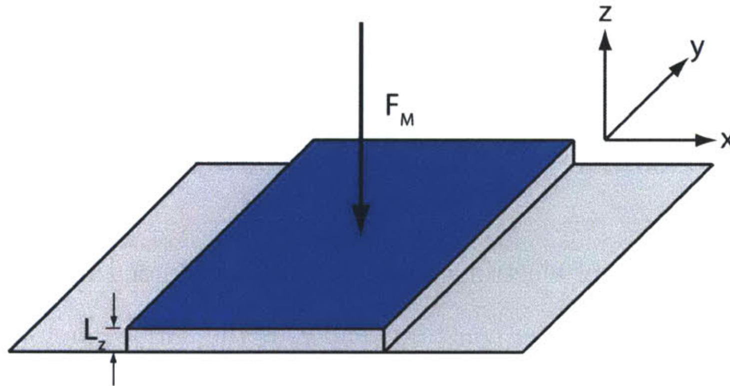

Figure 2-16: A thin slab is absolutely small in the direction of emission, z, but semi-infinite in the x and y directions. L_z is small enough to consider the emitter to be quantum confined, discretizing energies in the emission direction.

Unlike for bulk and nanowall emitters, the normal energies of a thin slab emitter are confined. The electrons are treated semi-classically, as particles vibrating between the walls of the thin slab in the dimension of emission [68]. The number of emitted electrons can be calculated by determining the frequency at which electrons strike the emitting surface, the spatial density of electrons per subband, and their transmission probability through the barrier per tunneling attempt. Normal energies take the form

of those for the infinite square well:

$$W_q = \frac{q^2 h^2}{8 m_0 L_z^2} \tag{2.60}$$

where q is the vibrational level of the electron and L_z is the thickness of the thin slab in the direction of emission. The classical frequency of vibration is given by

$$f_q = \frac{q^2}{L_z^2} \frac{h}{4 m_0}. \tag{2.61}$$

Since the thin slab is assumed to be one atomic layer thick, only a single electron subband should exist in the emitter below the maximum energy E_F. The classical current density incident on the emitting surface is

$$Z_q = e N_q f_q / \Sigma = N_q q a^{tns} / L_z^2 \Sigma \tag{2.62}$$

where N_q is the number of electrons from each atom included in the qth level, e is the elementary charge, a^{tns} is a constant, and Σ is the surface area associated with each atom.

The transmission function takes the same form as in Equation 2.4. As the normal energies are quantized, the barrier heights in the transmission function are also quantized, with $H = \phi + E_F - W_q$. Due to the quantization of the normal energies, thin-slab emitters will most likely see higher barrier heights than bulk emitters.

In this model, only a single electron subband (the highest energy subband, q) is assumed to contribute to the emitted current density. As a result, the ECD is given by the product of the transmission function and the classical current density incident on the emitting surface:

$$J^{tns} = \frac{\lambda_Z^{tns} a^{tns} N_q q}{L_z^2 \Sigma} P_q \exp\left[-\frac{B}{F} \nu_q (\phi + E_F)^{3/2} \right] \tag{2.63}$$

where P_q is a tunneling prefactor, ν_q is the barrier-shape correction factor for electrons tunneling from the qth vibrational level, and λ_Z^{tns} is a supply correction factor.

2.5 Chapter Summary

The Fowler-Nordheim equation and model have been the primary method for analyzing experimental field emission data since the late 1920s. In order to attain greater agreement between the FN model and experimental results, correction terms have been appended to the FN equation that account for physical phenomena omitted by the model and a separate treatment of field emission was developed for emission from semiconductors. However, these models are only appropriate for treating field emission from bulk emitters and may not be valid for treating field emission from quantum-confined structures. Recently, a few models for field emission from quantum-confined systems such as the nanowall and thin slab have emerged. These works treat field emission from quasi-2D structures, but a framework for treating field emission from systems of arbitrary geometry and reduced dimensionality is desired. Chapter 3 develops such a framework and employs it to derive ECD equations for a variety of quantum-confined emitter geometries.

Chapter 3

Elementary Framework for Cold Field Emission from Metal Emitters

3.1 Introduction

In this chapter, an elementary framework for field emission from metals at $T = 0K$ is developed. The elementary framework includes only the most basic physical phenomena required for treating field emission from metals, enabling the derivation of approximate, analytical, emitted current density equations for emitters with a 3D, 2D, or 1D electron density of states. Such equations make it possible to isolate changes in the supply function, transmission function, and total emitted current density solely due to imposing quantum confinement upon the electron supply. The elementary framework also serves as the basis for the development of the treatment of field emission from silicon emitters, which is the subject of Chapter 4.

3.2 Model for Field Emission from Quantum-Confined Emitters

3.2.1 Definition of Emitter System

The model that serves as the basis of the framework is qualitatively the same as the model used in deriving the elementary Fowler-Nordheim equation in §2.1, but with the addition of quantum confinement effects. In this model, quantum confinement is classified into two categories based on the orientation of the confinement direction relative to the emission direction. Transverse quantum confinement occurs when a dimension transverse to the emission direction is confined, while normal quantum confinement is the case in which the dimension in the direction of emission is confined. As the supply of electrons to the emitting surface and transmission probability of electrons through the potential barrier are functions of the normal energy, it is convenient to separate electron emitters into two categories: (i) normally-unconfined (NU) emitters and (ii) normally-confined (NC) emitters, both of which may also be transversally-quantum-confined. These two cases of emission are illustrated in Figure 3-1. Energies of confined electrons are taken to be those of the well consistent with the system's geometry.

3.2.2 Quantum Confinement of Electrons

At some point, when a system of electrons is compressed spatially, the assumption that they have a quasi-continuous distribution of wave vectors and energies becomes invalid. Their wave functions, wave vectors, and energies are no longer those of the free electron and must be calculated directly from the time-independent Schrödinger equation:

$$E\psi = -\frac{\hbar^2}{2m_0}\nabla^2\psi + V\psi \tag{3.1}$$

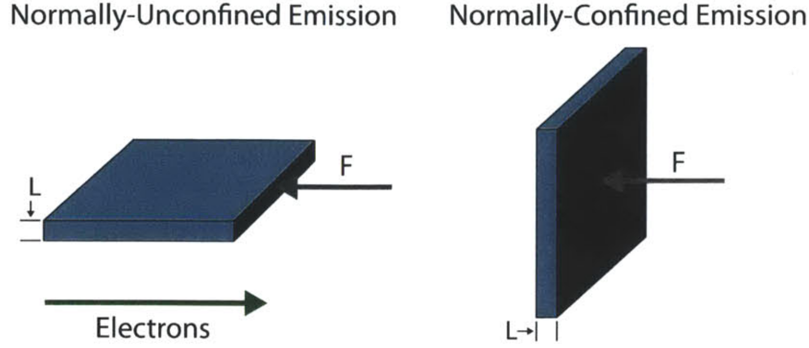

Figure 3-1: Normally-unconfined emission (left) is characterized by a lack of quantum confinement in the direction of emission, while normally-confined emission (right) consists of an emitter confined in the emission direction.

where E is the energy of the electron, ψ is the electron wave function, and V is the system's potential. As the emitted current density equations for the nanowall and cylindrical nanowire will be applications of this framework, the well geometries of interest here are the infinite square well and infinite cylindrical well.

Infinite Square Well

Quantum-confined dimensions of emitters with rectangular geometries will be treated as infinite square wells, shown in Figure 3-2. The potential for the one-dimensional infinite square well is

$$V(z) = \begin{cases} 0 & \text{for } 0 < z < L \\ \infty & \text{for } z < 0 \text{ and } z > L \end{cases} \tag{3.2}$$

where L is the width of the well. Inserting the infinite square well potential into the time-independent Schrödinger equation gives

$$E\psi(z) = -\frac{\hbar^2}{2m_0}\frac{d^2\psi(z)}{dz^2} \tag{3.3}$$

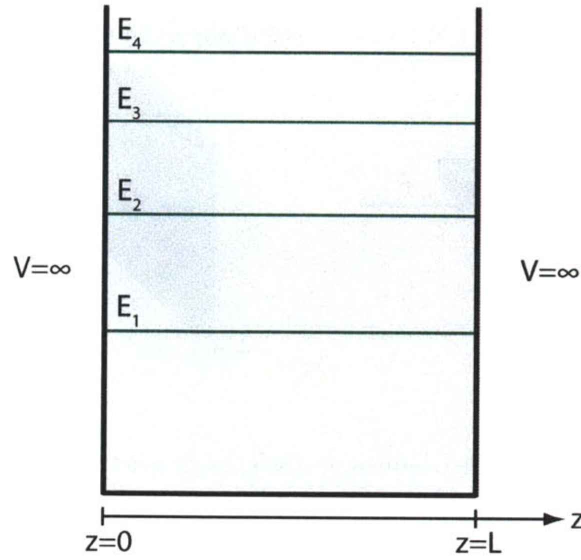

Figure 3-2: Diagram of the infinite square well of width L and the first four energy levels.

which is valid for $0 < z < L$. Defining $k^2 = 2m_0E/\hbar^2$, the differential equation has the solution

$$\psi(z) = A\sin[kz] + B\cos[kz] \tag{3.4}$$

where k is the electron wave vector. Due to boundary conditions, the value of the wave function must be equal to zero at the well edges, requiring that $B = 0$ and $k = n\pi/L$. Equating the value of k as defined in the differential equation with k from the boundary condition gives the wave functions and energies of the infinite square well [69]:

$$\begin{aligned}\psi_n(z) &= \sqrt{\frac{L}{2}}\sin\left[\frac{n\pi z}{L}\right] \\ E_n &= \frac{n^2h^2}{8m_0L^2}\end{aligned} \tag{3.5}$$

where n is the vibrational level and subband index of the electron. For the three-dimensional Schrödinger equation in Cartesian coordinates, the energies in the x and

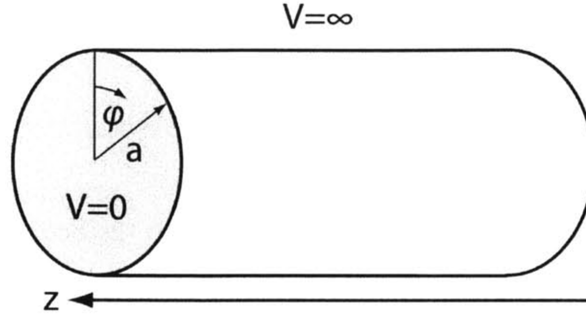

Figure 3-3: Diagram of the infinite cylindrical well of radius a.

y dimensions take those of the free electron and the total energy for the system is

$$E = \frac{\hbar^2 k_x^2}{2m_0} + \frac{\hbar^2 k_y^2}{2m_0} + \frac{n^2 h^2}{8m_0 L^2}. \tag{3.6}$$

Infinite Cylindrical Well

A quantum-confined emitter with a cylindrical geometry is treated as an infinite cylindrical well, shown in Figure 3-3. The infinite cylindrical well has a potential of the form

$$V(\rho) = \begin{cases} 0 & \text{for } 0 < \rho < a \\ \infty & \text{for } \rho > a \end{cases} \tag{3.7}$$

where ρ is the radial coordinate as measured from the center of the well and a is the radius of the well. Since the potential is not one-dimensional for the cylindrical well, the time-independent Schrödinger equation must be solved in cylindrical coordinates for $0 < \rho < a$:

$$E\psi(\rho,\phi,z) = -\frac{\hbar^2}{2m_0}\left[\frac{1}{\rho}\frac{\partial}{\partial\rho}\left(\rho\frac{\partial\psi(\rho,\phi,z)}{\partial\rho}\right) + \frac{1}{\rho^2}\frac{\partial^2\psi(\rho,\phi,z)}{\partial\phi^2} + \frac{\partial^2\psi(\rho,\phi,z)}{\partial z^2}\right] \tag{3.8}$$

where ϕ is the polar angle and z is the axis about which the cylinder is centered. The equation can be solved by the method of separation of variables, assuming that there

is a solution of the form

$$\psi(\rho, \phi, z) = R(\rho)\,\Phi(\phi)\,Z(z)\,. \tag{3.9}$$

Substituting the above form for the wave function into the Schrödinger equation and rearranging gives the equation

$$-\frac{2m_0 E}{\hbar^2} = \frac{1}{R(\rho)}\left[\frac{\partial^2 R(\rho)}{\partial \rho^2} + \frac{1}{\rho}\frac{\partial R(\rho)}{\partial \rho}\right] + \frac{1}{\rho^2}\frac{1}{\Phi(\phi)}\frac{\partial^2 \Phi(\phi)}{\partial \phi^2} + \frac{1}{Z(z)}\frac{\partial^2 Z(z)}{\partial z^2}. \tag{3.10}$$

Due to the sum of the equations being equal to a constant, the Schrödinger equation can be separated into parts that only involve z, ϕ, and ρ. Once separated, the equation involving $Z(z)$ is recognizable as the Schrödinger equation for a free electron in one dimension:

$$-k_z^2 = \frac{1}{Z(z)}\frac{\partial^2 Z(z)}{\partial z^2} \tag{3.11}$$

whose solution yields the wave functions and energies of the electron in the z-dimension:

$$\begin{aligned} Z(z) &= \exp\left[\pm \imath k_z z\right] \\ E_z(z) &= \frac{\hbar^2 k_z^2}{2m_0} \end{aligned} \tag{3.12}$$

where k_z is the electron wave vector in the z direction. The equation for $\Phi(\phi)$ is [70]

$$\frac{\partial^2 \Phi(\phi)}{\partial \phi^2} + m^2 \Phi(\phi) = 0. \tag{3.13}$$

Solving this equation yields a set of angular wave functions, which are eigenfunctions of the angular momentum operator, but have no energy eigenvalues:

$$\begin{aligned} \Phi(\phi) &= \frac{1}{\sqrt{2\pi}} \exp\left[\imath m \phi\right] \\ L &= \hbar m \end{aligned} \tag{3.14}$$

where m is an integer and quantum number related to the electron's angular momentum. The remaining function is $R(\rho)$, which has an equation of the form:

$$\rho^2 \frac{\partial^2 R(\rho)}{\partial \rho^2} + \rho \frac{\partial R(\rho)}{\partial \rho} + \left[k^2 \rho^2 - m^2\right] R(\rho) = 0 \tag{3.15}$$

The solution to this differential equation is the sum of a Bessel function of the first kind and a Bessel function of the second kind:

$$R(\rho) = AJ_m(k\rho) + BN_m(k\rho) \tag{3.16}$$

Imposing the boundary conditions that the radial wave function must be finite at $\rho = 0$ and zero at $\rho = a$ gives the radial wave functions and energies:

$$\begin{aligned} R(\rho) &= J_m(k\rho) \\ E_\alpha &= \frac{h^2 \alpha_{m,n}^2}{8\pi^2 m_0 a^2} \end{aligned} \tag{3.17}$$

where $\alpha_{m,n}$ is the nth zero of the mth order Bessel function of the first kind. Summing the energy contributions from all dimensions of the well gives the total energy for an electron in an infinite cylindrical well as

$$E = \frac{h^2 \alpha_{m,n}^2}{8\pi^2 m_0 a^2} + \frac{\hbar^2 k_z^2}{2m_0}. \tag{3.18}$$

While the energy terms come only from the radial and free-electron wave functions, not all of the kinetic energy is directed radially or along the z axis. The angular momentum present for wave functions for which $m \neq 0$ leads to an average non-radial kinetic energy component equal to [70]

$$\left\langle \hat{T}_\phi \right\rangle = \left\langle R(\rho) \left| \frac{\hbar^2 m^2}{2m_0 \rho^2} \right| R(\rho) \right\rangle \tag{3.19}$$

The radially-directed kinetic energy of the electron is then defined as

$$< \hat{T}_{\rho} >= E_{\alpha_{m,n}} - \left\langle \hat{T}_{\phi} \right\rangle . \tag{3.20}$$

3.3 Construction of the Framework

3.3.1 Emitted Current Density

The emitted current density from a single electronic state $J_{q,\alpha}$ for a normal energy W_q and transverse energy E_t is proportional to the product of supply function $N_{q,\alpha}(W_q)$, the electron flux impinging on the emitting surface, and transmission function $D_{q,\alpha}(F, W_q)$, the probability of electron transmission through the potential barrier into vacuum. The total emitted current density is calculated by summing over the contributions from all electronic states in the system and multiplying by the elementary charge:

$$J(F) = e \sum_{q} \sum_{\alpha} N_{q,\alpha}(W_q) D_{q,\alpha}(F, W_q) \tag{3.21}$$

where e is the elementary charge ,q is the subband index of normal electrons, and α is the subband index for transverse electrons. In the remainder of this section, a general framework for constructing supply functions and transmission functions for quantum-confined emitters is developed.

3.3.2 Supply Functions

The supply function quantifies the flux of electrons traveling normal to the emitting surface. In general, the supply function consists of two components: an attempt

frequency ν and a transverse electron density n_t:

$$N(W) = \nu \times n_t \tag{3.22}$$

Attempt Frequency

The attempt frequency is the frequency at which electrons pass a plane parallel to the emitting surface and is comprised of the normal electron group velocity v_g and the spatial density of states normal to the emitting surface $dn_\perp$.

$$\nu = v_g dn_\perp \tag{3.23}$$

Within the Sommerfeld theory of metals, the electrons are treated as point particles and the electron group velocity is readily calculated to be $v_g = \sqrt{2W/m_0}$. Excluding the spin degeneracy of electrons, the number of energy levels per unit length in a normal energy range dW, is found to be $dn_\perp = 1/h\sqrt{m_0/2W}dW$ [5]. The resulting arrival rate for NU emitters is the product of the group velocity and density of states:

$$\nu^u = \frac{1}{h}dW. \tag{3.24}$$

For NC emitters, if it is assumed that the electron is semi-classical, moving at the group velocity, and bouncing between the walls of a well with a bottom defined by the shape of the conduction band edge, the attempt frequency is given by [2]:

$$\nu_q^c = \left(\int_0^{Z_q} \sqrt{\frac{2m_0}{W_q - E_c(z)}}dz\right)^{-1} \tag{3.25}$$

where W_q is the discrete normal energy of electrons in subband q, E_c is the position of the conduction band edge as a function of z, and 0 and Z_q are the classical turning points of the electron. If the well is a square well of width L_z, the attempt frequency

simplifies to

$$\nu^{c}_{square,q} = \sqrt{\frac{2m_0}{W_q L_z^2}}. \tag{3.26}$$

Transverse Electron Density

The transverse electron density counts the spatial density of electrons in the metal with momentum parallel to the emitting surface and consists of two components: (i) the Fermi-Dirac distribution $f(W, k_t)$ and (ii) the transverse density of states $\rho_{t,M} = dn/dk_t$. The number of electrons with k-vectors in planes parallel to the emitting surface is determined by integrating the product of f and $\rho_{t,M}$ over all transverse k-vectors, k_t. The dimensionality of the system is given by M and is equivalent to the number of unconfined dimensions parallel to the emitting surface. A factor of 2 is appended to account for the spin degeneracy of electrons.

$$n_t = 2 \int f_{q,\alpha}\left(W_q, \boldsymbol{k_t}\right) \rho_{t,M}\left(\boldsymbol{k_t}\right) \frac{d^M \boldsymbol{k_t}}{(2\pi)^M} \tag{3.27}$$

where q and α are the normal and transverse subband indices. The form of the Fermi-Dirac distribution used here is given in terms of the transverse k-vector and is a function of the normal energy. When $\rho_{t,M}$ is transformed so that it depends only on the magnitude of k_t, $E\left(\boldsymbol{k_t}\right) \rightarrow \hbar^2 k_t^2 / \left(2m_0\right)$ plus any energy due to transverse confinement.

$$f_{q,\alpha}\left(W_q, \boldsymbol{k_t}\right) = \frac{1}{1 + \exp\left[\frac{W_q + E_{t,\alpha}(\boldsymbol{k_t}) - E_F}{k_B T}\right]} \tag{3.28}$$

While the form of the attempt frequency depends only on the dimensionality of the system normal to the emitting surface, the transverse electron density is sensitive to the transverse dimensionality. Therefore, the specific form for $\rho_{t,M}$ and the integration space are governed by the number of unconfined dimensions parallel to the emitting

surface.

$$\rho_{t,M}(k_t) = \begin{cases} 2\pi k_t & \text{for M=2,} \quad (3.29a) \\ 2\delta_\alpha & \text{for M=1,} \quad (3.29b) \\ \delta_\alpha & \text{for M=0,} \quad (3.29c) \end{cases}$$

The spatial dependence of the supply function is per unit area, which may require that the subband supply function be divided by the transverse cross sectional length or area of the emitter's quantum wells, denoted by L^{2-M}.

With all of the necessary pieces of the supply function, forms specific to both the NU emission case, N^u, and NC emission case, N^c, can be assembled:

$$N^u_\alpha = \frac{2}{hL^{2-M}} dW \int f_\alpha(W, k_t)\, \rho_{t,M}(k_t) \frac{dk_t}{(2\pi)^M} \quad (3.30a)$$

$$N^c_{q,\alpha} = \frac{2}{L^{2-M}} \left(\int_0^{Z_q} \sqrt{\frac{2m_0}{W_q - E_c(z)}} dz \right)^{-1} \int f_{q,\alpha}(W_q, k_t)\, \rho_{t,M}(k_t) \frac{dk_t}{(2\pi)^M} \quad (3.30b)$$

3.3.3 Transmission Function

In the interest of obtaining approximate, analytical solutions for the emitted current density, the transmission function is derived using a JWKB-type approximation [43]. The Landau and Lifschitz form of the transmission function [71], which is valid in the case of a strong, non-ideal barrier regime ($\exp[-G] \ll 1$), applies to the nearly triangular potentials inherent in studies of cold field electron emission.

$$D(F, H) \approx P \exp[-G(F, H)] \quad (3.31)$$

P is known as the tunneling prefactor [72] and depends on the potential barrier shape and G is the JWKB exponent, as defined below. For the elementary framework, P is taken to be unity, which is consistent with previous treatments of cold field electron emission [40, 41]. The JWKB exponent also depends on the shape of the potential

barrier and is defined as follows:

$$G(F,H) = g_0 \int_{Z_1}^{Z_2} \sqrt{M(l,F,H)}dl \tag{3.32}$$

where $g_0 = (4\pi/h)\sqrt{2m_0}$ is the JWKB coefficient for electrons, M is a function that is defined by the shape of the potential barrier, l is the distance into vacuum, as measured from Z_1 the first classical turning point and the surface of the metal, and Z_2 is the second classical turning point. For the exact triangular barrier,

$$M_{ET}(l,F,H) = H - eFl \tag{3.33}$$

where H is the potential barrier height that the electron sees when approaching the barrier with normal energy W and F is the magnitude of the electric field at the surface of the metal. Taking the emission direction to be z, $Z_1 = 0$, and $Z_2 = H/eF$, the JWKB exponent is calculated [41]:

$$G(F,H) = g_0 \int_{0}^{\frac{H}{eF}} \sqrt{H - eFz}dz = \frac{B}{\gamma_a F} H^{3/2}. \tag{3.34}$$

where $B = \frac{2g_0}{3e}$ is the second Fowler-Norheim constant, γ_a is the geometry-dependent field enhancement factor at the emitter tip, and H is the zero-field barrier height. It should be noted that more physically realistic barrier shapes, such as the Schottky-Nordheim barrier [48], are nearly triangular and their effect on the transmission function can be readily reincorporated into the JWKB exponent via the addition of a barrier shape correction factor ν [73], which is carried out in Chapter 4. For the case of the exact triangular barrier, $\nu \to 1$ [47], which is consistent with the calculation above. The zero-field barrier height, H, is defined as the electron affinity of the metal, which is the sum of the local work function, ϕ, and the Fermi energy, E_F, minus the

normal energy of the electron.

$$H = \phi + E_F - W \tag{3.35}$$

For field emitters in which quantum confinement effects are significant, it is convenient to define an emission reference level (ERL), which identifies the normal electronic state R in each subband that has the highest probability of transmission through the potential barrier [66]. In this model, the highest tunneling probability is defined as the electronic state with the highest normal energy, W_R. From the concept of ERL, two more mathematically convenient parameters can be defined: the reference zero-field barrier height, H_R, and the transmission function decay rate, c_R [47]. The reference zero-field barrier height is the magnitude of the potential barrier seen by an electron that is occupying the electronic state designated as the subband ERL.

$$H_R = \phi + E_F - W_R \tag{3.36}$$

The transmission function decay rate, c_R, is the reciprocal of the amount that the zero-field barrier height must be lowered in order to increase the probability of electron transmission by a factor of approximately exp [1] at the reference state. It is a result of the usual expansion of the transmission coefficients about a particular forward energy level:

$$c_R = -\frac{d\left(lnD\right)}{dH} \approx \frac{3B}{2\gamma_a F} H_R^{1/2}. \tag{3.37}$$

Since the transmission probability exponentially increases with increasing normal energy, it is valid to assume that the majority of emitted electrons are from the highest energy state, or $W \approx W_R$. In this case, the transmission function can be expanded via a Taylor series of H around H_R and the transmission function for NU emitters is

obtained:

$$D^u(F,W) \approx \exp\left[-\frac{B}{\gamma_a F} H_R^{3/2}\right] \exp\left[-c_R (H - H_R)\right] \tag{3.38}$$

Given that in the NU case, $W = E_F - E_{t,\alpha}$, the ERL should be calculated by minimizing the transverse kinetic energy of electrons. When electrons are unconfined in dimensions parallel to the emitting surface, the transverse energies form a quasi-continuum and $E_{t,min}$ can be reduced to zero, allowing $W_R = E_F$. However, when electrons are transversally confined, their transverse energies are fixed at the energy of the subband they occupy $E_{t,\alpha}$, which is determined by the shape of the well. Since the maximum total energy of electrons is fixed at E_F and the transverse energy is fixed at $E_{t,min,\alpha} = E_{t,\alpha}$, W_R is reduced by $E_{t,min,\alpha}$ relative to the bulk emitter case. Transverse quantum confinement requires that transverse electrons have non-zero minimum energies, effectively making that energy inaccessible for normal electrons to use for tunneling through the barrier. As a result, the reduced ERL has the effect of raising H_R by $E_{t,min,\alpha}$ [41].

$$H_{R,\alpha} = H_R^{bulk} + E_{t,min,\alpha} = \phi + E_{t,\alpha} \tag{3.39}$$

When determining the reference barrier height in the case of NC emitters, it is important that the definition of the ERL remain consistent with its previous usage. To reiterate, the ERL is the electronic state within each *subband* that has the highest probability for transmission through the barrier. This has important implications for the NC emission case, as within each subband there is only one possible value of normal energy for electrons: W_q, the discrete normal energy of the subband. Consequently, for all subbands, $W_R = W_q$ and $H_R = H_q$, so the transmission function for NC emitters reverts to its form prior to the Taylor series expansion:

$$D_q^c(F,W_q) = \exp\left[-\frac{B}{\gamma_a F} H_q^{3/2}\right] \tag{3.40}$$

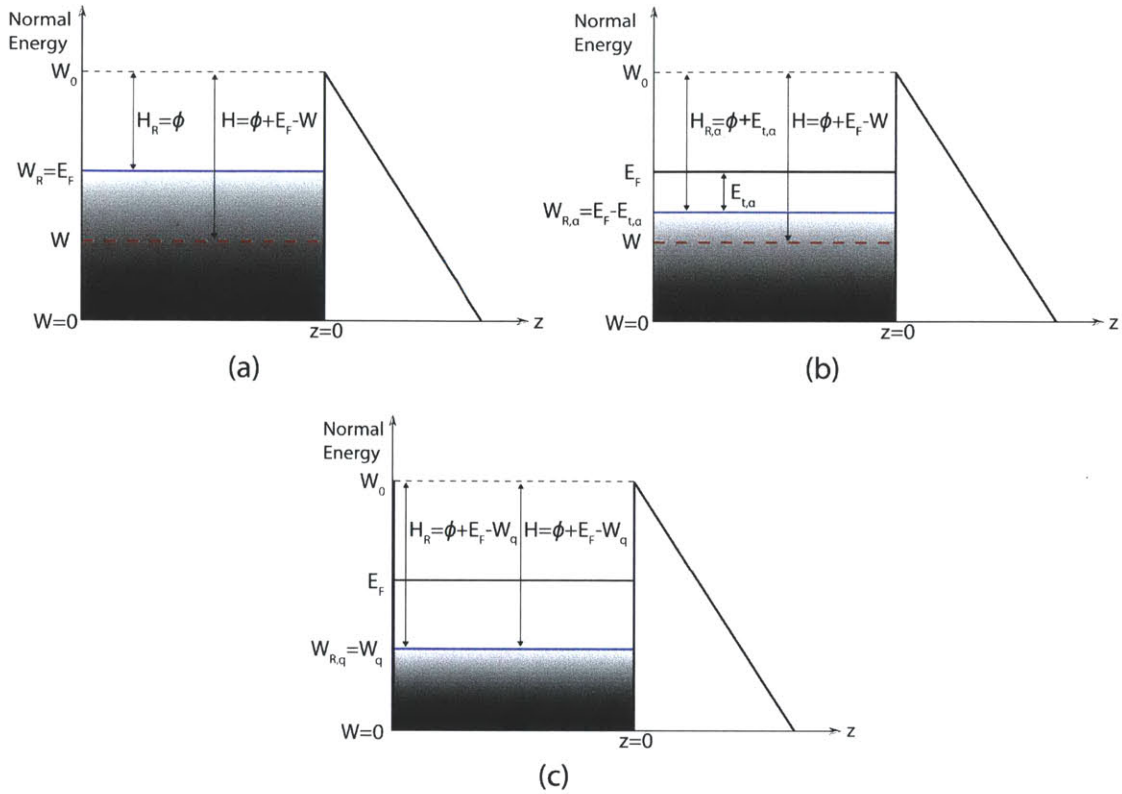

Figure 3-4: Normal energy diagrams for (a) bulk emitter, (b) normally-unconfined emitter that is also transversally confined, and (c) normally-confined emitter that is not transversally confined (c).

Normal energy diagrams for a bulk emitter, NU emitter, and NC emitter are shown in Figure 3-4.

In order to obtain the total emitted current density from quantum-confined emitters, it is necessary to sum over all subbands that contribute to emission. For $T = 0$K, the highest contributing subband energy may not exceed E_F. For the cylindrical well, the subband indices are given by the zeros of the Bessel functions, which are tabulated. Therefore, all subbands in a cylindrical well with indices leading to an energy less than or equal to the Fermi energy contribute to emission. For the infinite square well, the expressions for the terminal subband indices depend on the nesting order of the summations. In the case of a single degree of quantum confinement, the terminal

subband index A is calculated using E_F as the maximum energy:

$$A_x = \text{Integer}\left[\frac{2L_x}{h}\sqrt{2m_0 E_F}\right] \tag{3.41}$$

In the case of two degrees of quantum confinement, the terminal subband index of the inner summation must be calculated with regard to the outer summation's subband index, with a maximum energy $E_F - E_\alpha$,

$$A_y = \text{Integer}\left[\frac{2L_y}{h}\sqrt{2m_0\left(E_F - E_{\alpha_x}\right)}\right] \tag{3.42}$$

where E_{α_x} is the energy of the outer summation's subband, L_x is the infinite square well width for the outer summation, and L_y is the inner subband's infinite square well width. This method ensures that only valid subband energies enter the summation and no contributing subbands are excluded.

3.4 Application of the Elementary Framework: Emitted Current Density Equations

In order to extract the qualitative effects of transverse and normal quantum confinement on the current density emitted from a metal at $T = 0$ K, emitted current density equations for specific emitter geometries are derived. The systems were chosen in conjunction with the Fowler-Nordheim equation and the NU nanowall equation to cover the cases of NU emitters with zero, one, and two transversally-confined dimensions and the cases of NC emitters with zero and one transversally-confined dimension. An emitted current density equation was not derived for the case of a NC emitter with two transversally-confined dimensions (quantum dot) because Fermi-Dirac statistics are not suitable for describing the behavior of a small, finite number of electrons, which places it outside the scope of the model.

In applying the framework to specific emitter geometries, it is assumed that all emitters are oriented such that the electric field F is applied from the z direction and all electrons are emitted into the z direction. All energies lacking a subscript are to be considered continuous variables, while energies with an index in the subscript are discrete due to quantum confinement. Energies normal to the emitting surface are in general denoted by W and all other energies are denoted by E. In systems that are transversally-confined (in Cartesian coordinates), the first dimension subject to confinement is the x direction, with well width L_x, and the second is the y direction, with well width L_y. In normally-confined systems the well width is denoted by L_z. While the highlights of the derivations are in the sections below, the details of the derivations are located in Appendix B. In addition, expressions for the field enhancement factors (γ_a) relevant to the tip geometries of the emitters considered below are derived in Appendix C.

3.4.1 Normally-Unconfined Emitted Current Density Equations

Fowler-Nordheim Equation and Nanowall Equation

Within the class of normally-unconfined emitters are two systems whose emitted current density equations are already known: the bulk emitter and the NU nanowall, both shown in Figure 3-5. Applying the framework to a bulk emitter yields the elementary form of the Fowler-Nordheim equation that is consistent with the approximations and assumptions made in developing this framework [40] and will be referred to as the bulk emitted current density equation.

$$J_{bulk}(F) = e\frac{4\pi m_0}{h^3}c_3^{-2}\exp\left[-\frac{B}{\gamma_a F}\phi^{3/2}\right] \tag{3.43}$$

where $c_3 = 3B\sqrt{\phi}/2\gamma_a F$.

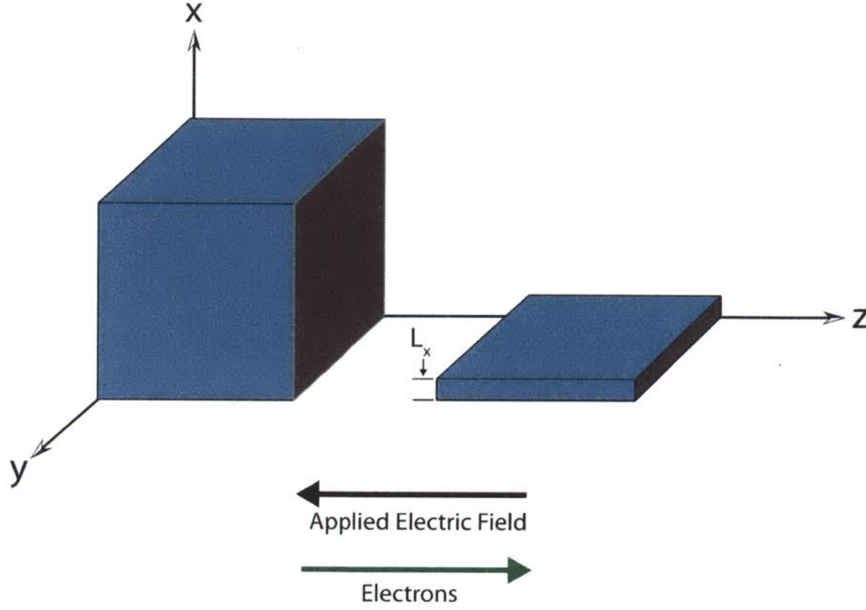

Figure 3-5: Emission from a bulk emitter (left) and normally-unconfined nanowall emitter (right).

Another known equation that falls under the category of an NU emitter is the nanowall equation, as derived by Qin et al. [41]:

$$J^u_{nwall} = e\frac{2}{h^2}\sqrt{2\pi m_0}L_x^{-1}\sum_{\alpha_x=1}^{A_x}\delta_{\alpha_x}c_{2,\alpha_x}^{-3/2}\exp\left[-\frac{B}{\gamma_a F}\left(\phi+E_{\alpha_x}\right)^{3/2}\right] \tag{3.44}$$

where δ_{α_x} is the Kronecker delta function, $c_{2,\alpha_x} = 3B\sqrt{\phi + E_{\alpha_x}}/2\gamma_a F$,$E_{\alpha_x}$ is the energy associated with transverse quantum confinement in the x-direction, with length L_x, α_x is the electron subband index, and A_x is the index of the highest energy subband in the system.

NU Nanowire Equation

A normally-unconfined nanowire is transversally-confined in the $x-y$ plane, but semi-infinite in the emission direction, z. Since multiple nanowire geometries are possible (Figure 3-6), the ECD equation is derived in terms of a general transverse confinement

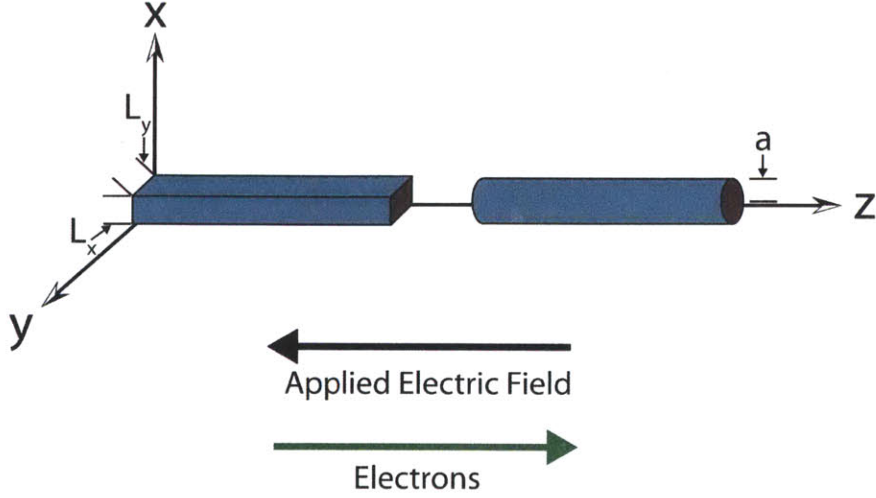

Figure 3-6: Emission from a normally-unconfined rectangular nanowire (left) and normally-unconfined cylindrical nanowire emitter (right).

energy, $E_{t,\alpha}$, cross-sectional area, A_e, and electron subband α. The supply function is given by Equation 3.30a and $\rho_{t,M}$ with $M = 0$ by Equation 3.29c:

$$N_\alpha (W) = \frac{2}{hA_e} dW \frac{\delta_\alpha}{1 + \exp\left[\frac{W + E_{t,\alpha} - E_F}{k_B T}\right]}. \tag{3.45}$$

For the transmission function, the reference zero-field barrier height is equal to the work function plus the energy associated with transverse quantum confinement for the given subband:

$$H_{R,\alpha} = \phi + E_{t,\alpha} \tag{3.46}$$

The transmission function is given by substituting the above expression for $H_{R,\alpha}$ in Equation (3.38).

$$D_\alpha (F, W) = \exp\left[-\frac{B}{\gamma_a F} (\phi + E_{t,\alpha})^{3/2}\right] \exp\left[c_{1,\alpha} (W + E_{t,\alpha} - E_F)\right] \tag{3.47}$$

Also dependent on the reference zero-field barrier height is the transmission decay rate, which is defined per electron subband:

$$c_{1,\alpha} = \frac{3B}{2\gamma_a F}\sqrt{\phi + E_{t,\alpha}} \tag{3.48}$$

In order to obtain the emitted current density per electron subband, the product of the electron charge, supply function, and transmission function is integrated over all normal energies, from 0 to $E_F - E_{t,\alpha}$. Performing the integration (§A.1.1) yields the ECD equation for the NU nanowire:

$$J^u_{nwire}(F) = e\frac{2}{hA_e}\sum_{\alpha}\delta_\alpha c_{1,\alpha}^{-1}\exp\left[-\frac{B}{\gamma_a F}\left(\phi + E_{t,\alpha}\right)^{3/2}\right]. \tag{3.49}$$

The ECD equation for a rectangular nanowire is obtained by noting that the transverse confinement energies are those of the infinite square well (Equation 3.6) in x and y ($E_{t,\alpha} = E_{\alpha_x} + E_{\alpha_y}$) and by defining a cross-sectional area $A_{e,rect} = L_x L_y$. This gives the NU rectangular nanowire emitted current density equation

$$J^u_{rwire}(F) = e\frac{2}{hL_xL_y}\sum_{\alpha_x=1}^{A_x}\delta_{\alpha_x}\sum_{\alpha_y=1}^{A_{y,\alpha_x}} c_{1,\alpha_x,\alpha_y}^{-1}\exp\left[-\frac{B}{\gamma_a F}\left(\phi + E_{\alpha_x} + E_{\alpha_y}\right)^{3/2}\right] \tag{3.50}$$

where $c_{1,\alpha_x,\alpha_y} = 3B\sqrt{\phi + E_{\alpha_x} + E_{\alpha_y}}/2\gamma_a F$. For the cylindrical nanowire, the transverse confinement energies take the form of those in Equation 3.17 and the cross-sectional area is defined as $A_{e,cyl} = \pi a^2$, where a is the radius of the nanowire. Making these substitutions yields the NU cylindrical emitted current density equation:

$$J^u_{cwire}(F) = e\frac{2}{\pi h a^2}\sum_{\alpha_{m,n}}^{A_{m,n}}\delta_{\alpha_{m,n}} c_{1,\alpha_{m,n}}^{-1}\exp\left[-\frac{B}{\gamma_a F}\left(\phi + \alpha_{m,n}\right)^{3/2}\right] \tag{3.51}$$

where $c_{1,\alpha_{m,n}} = 3B\sqrt{\phi + E_{\alpha_{m,n}}}/2\gamma_a F$.

3.4.2 Normally-Confined Emitted Current Density Equations

NC Nanowall Equation

The supply function for the normally-confined nanowall with normal well width L_z, shown in Figure 3-7, is given by Equation 3.30b with $\rho_{t,M}$ corresponding to Equation 3.29a, indicating no transverse quantum confinement.

$$N_q\left(W_q\right) = \frac{2}{2\pi 2L_z}\sqrt{\frac{2W_q}{m_0}}\delta_q 2\int_0^{\infty}\frac{2\pi k_t}{1+\exp\left[\frac{W_q+\frac{\hbar^2k_t^2}{2m_0}-E_F}{k_BT}\right]}\frac{dk_t}{(2\pi)^2} \tag{3.52}$$

The integral also appears in the supply function for a bulk emitter and has a known analytical solution:

$$N_q\left(W_q\right) = \frac{8\pi m_0 k_B T}{h^3}\frac{W_q}{q}\delta_q \ln\left[1+\exp\left[\frac{E_F-W_q}{k_BT}\right]\right] \tag{3.53}$$

Since there is no meaningful definition of a reference zero-field barrier height for NC emitters, it is not useful to expand the transmission function about an emission reference level and the transmission probability is given by (3.40).

$$D_q\left(F,W_q\right) = \exp\left[-\frac{B}{\gamma_a F}\left(\phi+E_F-W_q\right)^{3/2}\right]. \tag{3.54}$$

The emitted current density from a single subband of electrons is calculated from the product of the elementary electron charge, supply function, and transmission coefficients (§B.2.1). The total ECD for the NC nanowall is

$$J^c_{nwall}\left(F\right) = e\frac{8\pi m_0}{h^3}\sum_{q=1}^{Q}\frac{W_q}{q}\delta_q\left(E_F-W_q\right)\exp\left[-\frac{B}{\gamma_a F}\left(\phi+E_F-W_q\right)^{3/2}\right]. \tag{3.55}$$

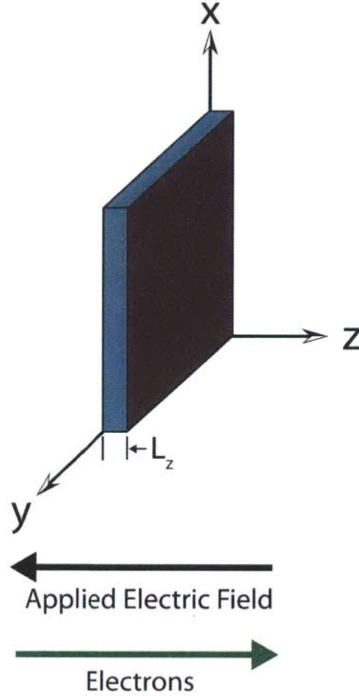

Figure 3-7: Emission from a normally-confined nanowall emitter.

NC Nanowire Equation

Just as in the NU nanowire case, the ECD equations for the NC nanowire can be presented in a geometry-independent form by defining the transverse confinement energy as $E_{t,\alpha}$, a cross-sectional length L_e, and distance between collisions with the emitting surface, d. While the supply function for a normally-confined nanowire is readily found by using Equation 3.30b and Equation 3.29b, the integral has no known analytical solution and approximations must be made in order to continue (§B.2.1). The approximate supply function is given by

$$N_{q,\alpha}(W_q) = \frac{8}{dhL_e}\sqrt{W_q(E_F - W_q - E_{t,\alpha})} \tag{3.56}$$

Multiplying the supply function by the elementary charge, transmission function in Equation 3.40 and summing over all subbands produces the NC nanowire emitted

current density equation.

$$\begin{aligned} J^c_{nwire}\left(W_q,F\right) = e\frac{8}{dh}L_e^{-1}\sum_q^Q\sum_\alpha^A\sqrt{W_q\left(E_F-W_q-E_{t,\alpha}\right)} \\ \times\exp\left[-\frac{B}{\gamma_a F}\left(\phi+E_F-W_q\right)^{3/2}\right]. \end{aligned} \tag{3.57}$$

For a NC rectangular nanowire (Figure 3-8), emission occurs in the z direction, with an cross-sectional length of L_x in the x direction. The well energies in the x and

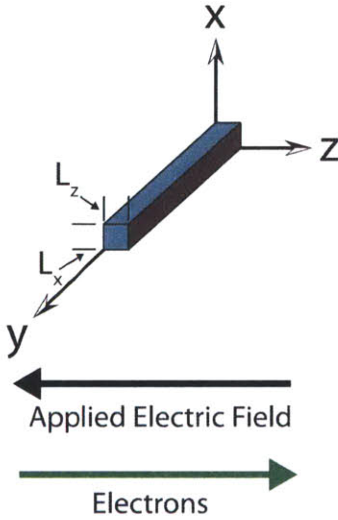

Figure 3-8: Emission from a normally-confined nanowire emitter.

z dimensions are given by the infinite square well energies with subband indices α_x and q and the distance traveled between collisions with the emitting surface is twice the well width in the z direction, L_z. These geometric parameters give the emitted current density for a rectangular nanowire:

$$\begin{aligned} J^c_{rwire}\left(W_q,F\right) = e\frac{4}{L_x L_z h}\sum_{q=1}^Q\sum_{\alpha_x}^{A_{x,q}}\sqrt{W_q\left(E_F-W_q-E_{\alpha_x}\right)} \\ \times\exp\left[-\frac{B}{\gamma_q F}\left(\phi+E_F-W_q\right)^{3/2}\right] \end{aligned} \tag{3.58}$$

Due to the model requiring that emission come from a planar surface, emission from the NC cylindrical nanowire falls outside direct focus of the work in this thesis. However, an ECD equation can still be derived for which the details are located in §B.2.2.

3.5 Chapter Summary

Using an elementary model of field emission similar to that employed by Fowler and Nordheim, a framework for treating emission from normally-unconfined and normally-confined emitters has been developed. General supply functions and transmission functions for NU and NC emitters of arbitrary geometry that apply to systems with two and one degrees of transverse quantum confinement were derived. Quantum confining an emitter transversally is shown to increase the zero-field barrier height seen by electrons traveling towards the barrier and reduce the density of states in the supply function. Emitted current density equations for the NU nanowire (rectangular and cylindrical), NC nanowall, and NC nanowire (rectangular) were presented and are part of an analysis of the consequences of quantum confinement of the electron supply on the ECD in Chapter 5.

Chapter 4

Treatment of Field Emission from Quantum-Confined Silicon Emitters

4.1 Introduction

While the framework and emitted current density equations developed in Chapter 3 provide a qualitative understanding of the effects of quantum confinement on the electron supply, many simplifications were made that make the model physically unrealistic. Due to these simplifications, the elementary framework is not appropriate for treating emission from semiconductors or for rough fits to experimental field emission data. This chapter develops a more physically-complete treatment of field emission, specifically for silicon field emitters, by incorporating the Schottky-Nordheim barrier potential for semiconductors, and band structure effects. Total emitted current density equations from the conduction band of emitters with Fermi energies above and below the conduction band edge are derived for the same emitter geometries as in Chapter 3.

4.2 Correction Factors: Emitter Electrostatics

4.2.1 Schottky-Nordheim Barrier for Semiconductors

Although the Schottky-Nordheim barrier potential, which incorporates the image potential from electrons just outside the emitting surface, was discussed for metals in §2.1, a correction must be made when applying it to semiconductor surfaces. The change in electrical permittivity between vacuum and the semiconductor, which has a dielectric constant ϵ_s, causes an abrupt change in the electric field at the semiconductor surface and alters the strength of the image potential correction. Including this correction into the potential yields the transmission function [54]

$$D(F,H) = \exp\left[-\frac{B}{F}\nu[y]\,H^{3/2}\right] \tag{4.1}$$

where $v = \sqrt{(\epsilon_s - 1)/(\epsilon_s + 1)}$, $y = \sqrt{e^3 vF/4\pi\epsilon_0}/H$, and H is the zero-field barrier height. When expanded about a reference barrier height H_R, the transmission function becomes

$$D(F,H) \simeq \exp\left[-\frac{B}{F}\nu[y_R]\,H_R^{3/2}\right]\exp\left[c_R(H_R - H)\right] \tag{4.2}$$

where $y_R = \sqrt{e^3 vF/4\pi\epsilon_0}/H_R$, $c_R = 3B\sqrt{H_R}t[y_R]/2F$ is the barrier decay rate at the reference state, and t is a weak function of y_R, tabulated along with values for ν in Table 2.1.

4.3 Correction Factors: Emitter Electron Supply for Silicon

4.3.1 Material Properties of Silicon

In order to proceed in constructing a more physically-complete model, it is necessary to designate an emitter material. Silicon is chosen due to its widespread use as an emitter material [74–82] and compatibility with microfabrication techniques [83]. Silicon is an indirect bandgap semiconductor with a diamond crystal structure, an energy gap of $E_g = 1.12$eV, conduction band minima in the <100> crystal directions, and a valence band maximum at the Γ point. It has two conduction band effective masses, defined as longitudinal (m_l) and transverse (m_t), which give rise to ellipsoidal constant energy surfaces in the conduction band [5], as shown in Figure 4-1. There

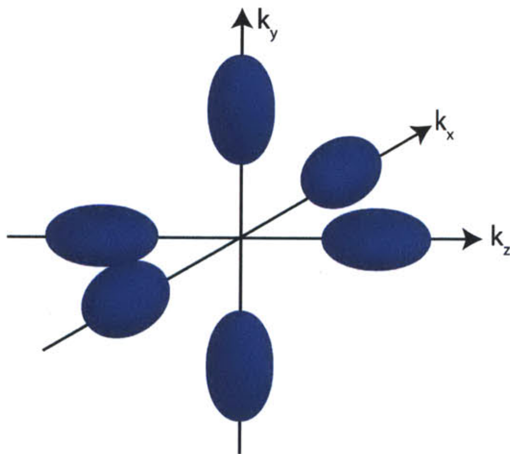

Figure 4-1: Electron constant energy surfaces of silicon.

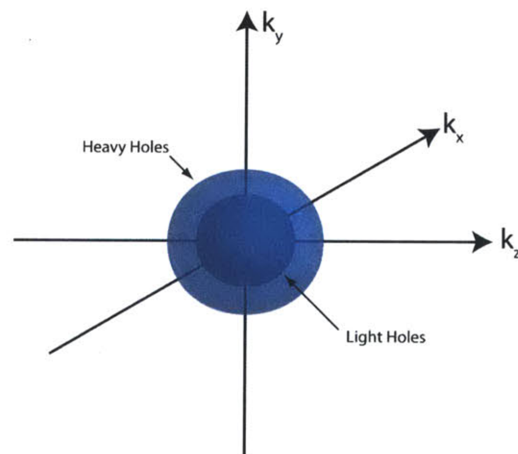

Figure 4-2: Heavy hole and light hole constant energy surfaces for the valence band of silicon. The split-off band is excluded due to its maximum lying lower in energy than the heavy hole and light hole bands.

are three valence band effective masses, one each for the light hole band (m_{lh}), heavy hole band (m_{hh}), and split-off band (m_{so}), all of which give rise to spherical constant

Physical Parameter	**Symbol**	**Value**	**Units**
Electron Affinity	χ	4.04	eV
Bandgap Energy @ T=300K	E_g	1.12	eV
DOS Electron Effective Mass	m_{de}	$1.09m_0$	eV·s^2/cm^2
DOS Hole Effective Mass	m_{dh}	$1.15m_0$	eV·s^2/cm^2
Longitudinal Conduction Band Effective Mass	m_l	$0.9163m_0$	eV·s^2/cm^2
Transverse Conduction Band Effective Mass	m_t	$0.1905m_0$	eV·s^2/cm^2
Heavy Hole Valence Band Effective Mass	m_{hh}	$0.537m_0$	eV·s^2/cm^2
Light Hole Valence Band Effective Mass	m_{lh}	$0.153m_0$	eV·s^2/cm^2
Split-Off Hole Valence Band Effective Mass	m_{so}	$0.234m_0$	eV·s^2/cm^2
Conduction Band Effective DOS	N_c	2.86×10^{19}	cm^{-3}
Valence Band Effective DOS	N_v	3.10×10^{19}	cm^{-3}
Intrinsic Carrier Concentration @ T=300K	n_i	1.07×10^{10}	cm^{-3}

Table 4.1: Selected material parameters of silicon [4,5].

energy surfaces in the valence band, as seen in Figure 4-2. The properties of silicon most relevant to studies of field emission are listed in Table 4.1.

4.3.2 Band Structure Corrections for QC Emitters

Spherical Approximation for Ellipsoidal Constant Energy Surfaces

Although the band structure corrections as applied to a bulk emitter with spherical constant energy surfaces were discussed for the conduction band and valence band in §2.2.2, the constant energy surfaces of silicon are ellipsoidal. Defining k_z as the emission direction in k-space, projections of the constant energy surfaces into the transverse plane are circles (along the k_z axis) and ellipses (along the k_x and k_y axes), as shown in Figure 4-3. In order to calculate band structure corrections for silicon via Stratton's method, it is necessary to determine the relation between the maximum transverse energy of the elliptical constant energy projections and the free electron energy as a function of ϕ, the angular coordinate in the $k_x - k_y$ plane. For an ellipse, the maximum transverse energy for a circular projection is [55]

$$E_m\left(E,\phi\right) = \frac{r_2}{\sin^2\left(\phi\right) + \frac{r_2}{r_1}\cos^2\left(\phi\right)}E \tag{4.3}$$

where $r_1 = m_t/m_0$ and $r_2 = m_l/m_0$ for silicon. This gives a corrected ECD for

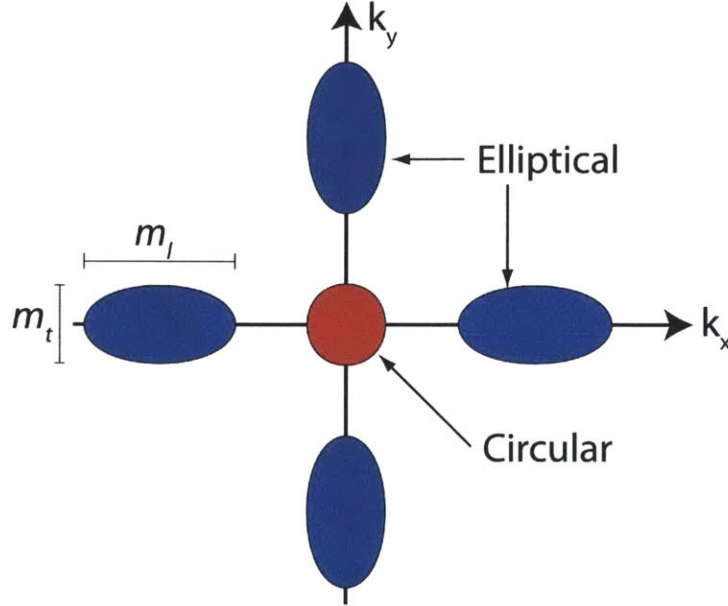

Figure 4-3: When projected into the k_x-k_y plane, the ellipsoidal constant energy surfaces of silicon become circles (characterized by m_t) along the axis of emission and ellipses (characterized by m_t and m_l) on axes perpendicular to the axis of emission.

emission from the conduction band of bulk silicon as

$$J = (F,T)\, e\frac{4\pi m_0}{h^3}\int_0^{\infty} dE f\,(E)\int_0^{2\pi} d\phi \int_0^{\frac{m_t}{\sin^2(\phi)+\frac{m_t}{m_l}\cos^2(\phi)}E} D\,(E-E_t)\, dE_t. \tag{4.4}$$

Since this integral does not have an analytical solution, approximations are needed in order to proceed. If it is assumed that the supply function is dominated by the total number of states enclosed by each constant energy surface, but is insensitive to the exact distribution of the states in k-space, the elliptical constant energy projections of silicon can be taken as circular constant energy projections. The effective mass that characterizes this new circular constant energy projection is found by equating the area enclosed by a circular constant energy projection with the area enclosed by silicon's elliptical constant energy projections. The result is an effective mass that is the geometric mean of the transverse effective mass and longitudinal effective mass.

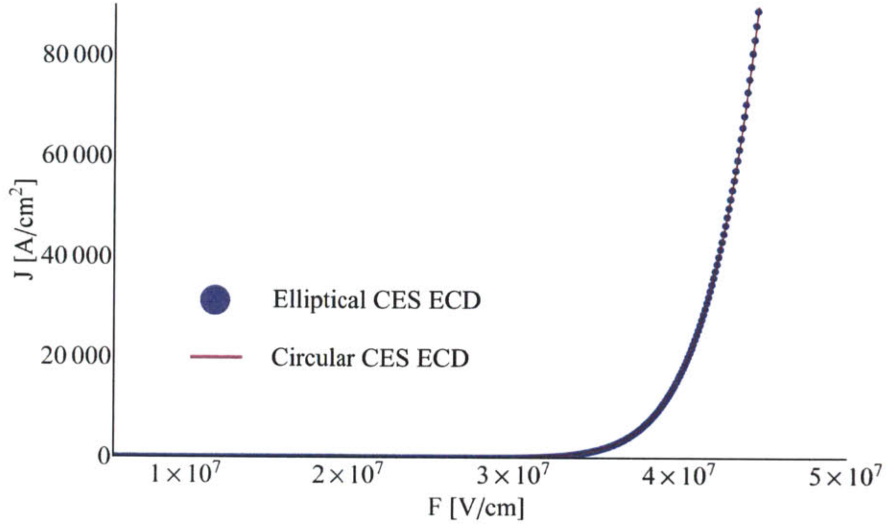

Figure 4-4: Plotting the ECD from an elliptical constant energy projection of a bulk emitter together with the ECD from the approximated circular constant energy projection with $E_m = E\sqrt{m_t m_l}/m_0$ shows that the approximation is in good agreement with the exact result.

For constant energy surfaces with elliptical projections in the transverse energy plane, the maximum transverse energy becomes

$$E_m(E) = \frac{\sqrt{m_t m_l}}{m_0} E \tag{4.5}$$

Figure 4-4 shows the validity of this approximation by plotting the numerically-calculated ECD from an elliptical constant energy projection and the ECD from the approximate circular constant energy projection for a bulk emitter. Using this approximation, the band structure corrections for spherical constant energy surfaces can be directly applied to all six constant energy surfaces of silicon.

Quasi-continuum Approximation for QC Emitters

When an emitter is quantum confined, electrons are split into subbands and the constant energy surfaces are reduced in dimension, as illustrated in Figure 4-5. This requires that the supply function integral in Equation 2.16 be replaced by its 2D and 1D counterparts and the band structure corrections be derived per electron subband.

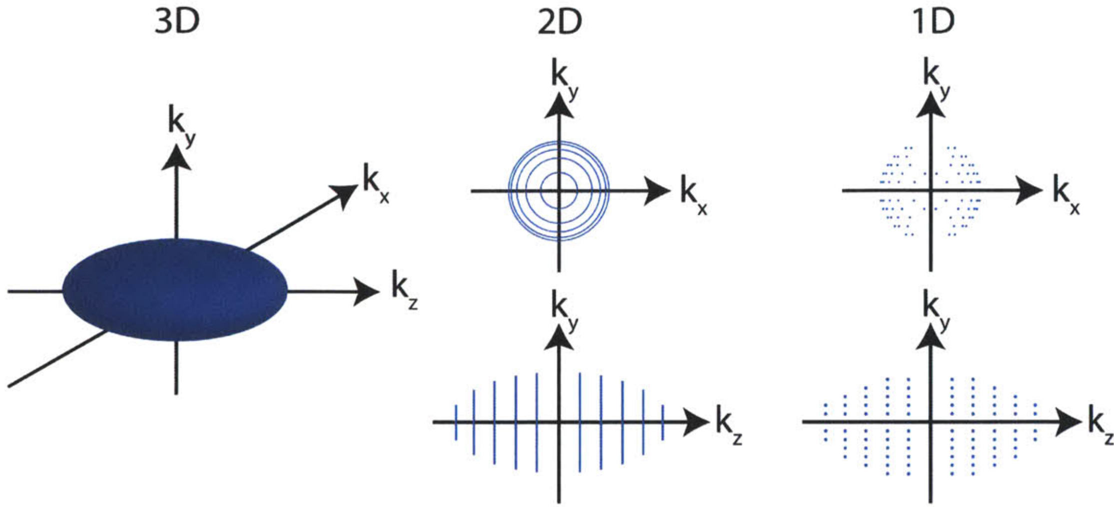

Figure 4-5: The 3D constant energy surfaces of silicon are reduced to constant energy contours in 2D and constant energy points in 1D.

Figure 4-6 shows that for a 3D electron gas, the energy discrepancy between the maximum free electron transverse energy and the maximum effective mass electron transverse energy, ΔE_t, is a continuous variable, while it has both continuous and discrete components for a 2D electron gas, and for a 1D gas is entirely discrete. In Stratton's treatment of band structure effects, the transverse energy discrepancy is integrated from 0 to ∞, which are the same limits of integration as for W, allowing the change of variables $\Delta E_t \to W$, as in Equation 2.18. Attempting to directly apply Stratton's band structure corrections to NU emitters results in problems for the 2D and 1D electron gases: i) the lack of a closed-form solution for the supply function of a 2D electron gas prevents an exact analytical calculation of the band structure corrections per subband in terms of ΔE_t and ii) the lack of integration over transverse energies to derive the supply function of a 1D electron gas results in no clear way to introduce band structure corrections.

However, if it is assumed that the energy states in the transverse plane lie close enough together that the transverse energies can be considered to form a quasi-continuum, ΔE_t becomes a continuous variable for the 2D and 1D electron gas cases and the band structure corrections can be calculated in a manner similar to Stratton's

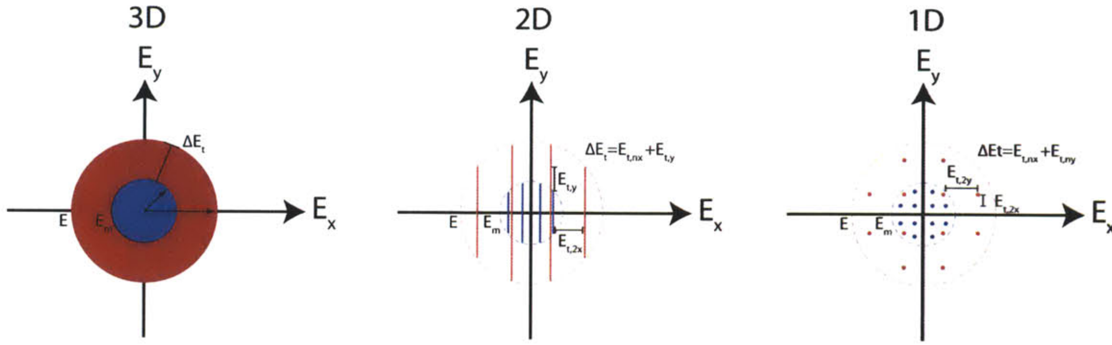

Figure 4-6: For a 3D electron gas, ΔW is defined between two constant energy surfaces and takes on continuous values, while for a 2D electron gas it is defined between two constant energy contours of the same subband index and is continuous within each subband. In the case of a 1D electron gas, ΔW is defined between two constant energy points in the transverse plane and is entirely discrete.

approach. This approximation allows for the band structure corrections to be entirely incorporated into the transmission function, leaving the supply functions unchanged, as in the bulk emitter case. Inspecting Equation 2.18, the corrected ECD from the conduction band for a bulk emitter can be written more generally as

$$J_c(F,T) = e\int_0^{\infty} N(W)\,dW\left[D(F,W) - \gamma_n D(F,\gamma_n W)\right] \tag{4.6}$$

where $\gamma_n = 1 - m_n/m_o$. With the quasi-continuum approximation as stated above, the ECD equations corrected for band structure effects can be derived by replacing $N(F,W)$ in Equation 4.6 with the form appropriate for a specific emitter geometry. While seemingly an approximation that contradicts the goal of the corrections being made, it is in good agreement with the numerically-calculated band structure correction factor for NU nanowall emitter, as shown in Figure 4-7.

4.4 Emitted Current Density Equations for Silicon

This section directly builds upon §3.4 by deriving emitted current density equations that are applicable to semiconductor emitters. The physically-complete model used

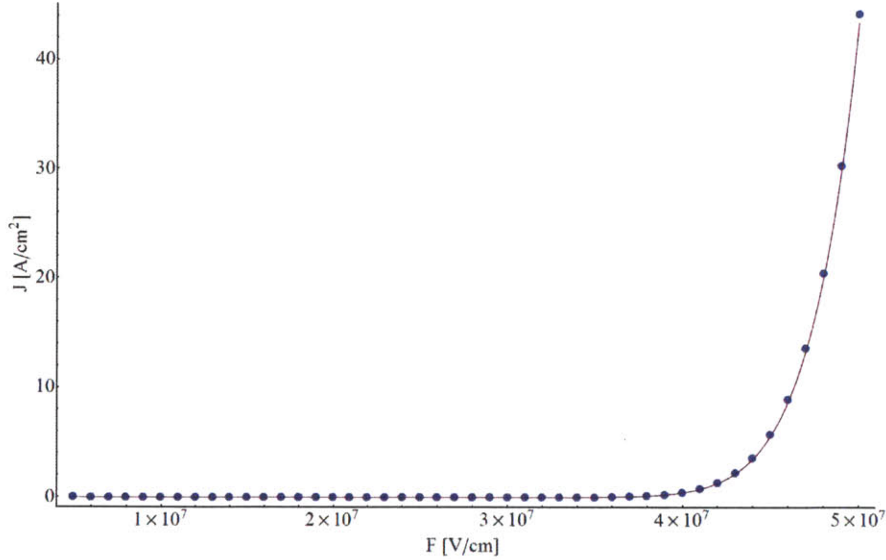

Figure 4-7: The numerically-calculated total ECD with band structure effects (points) and analytical, band-structure-corrected total ECD calculated via the quasi-continuum approximation for a single circular constant energy projection (solid) for a 1 nm NU nanowall as a function of the applied field.

here differs from the elementary model in four significant ways: i) emitters are no longer assumed to be at $T = 0$ K, ii) the barrier potential is now the Schottky-Nordheim barrier, iii) electrons are no longer considered to be free electrons inside the emitter, and iv) there are three pairs of constant energy surfaces for silicon, as opposed to the single free electron constant energy surface. The emission direction is defined as the [001] crystal direction of silicon, which corresponds to the k_z direction in k-space and the z direction in real space. Projected into planes transverse to the emission direction, the emitter has two circular constant energy projections (along the z axis) and four elliptical constant energy projections (along the x and y axes). As discussed in §4.1.1, the elliptical constant energy surfaces can be assumed to be circular constant energy projections.

The ECD equation derivations are split into two major sections: i) emission from the conduction band for $E_F > 0$ and ii) emission from the conduction band of an n-type semiconductor with $E_F < 0$. In both of these sections, the ECD from each of the six constant energy surfaces of 3D, 2D, and 1D NU and 2D and 1D NC silicon emitters

will be determined. Between constant energy surfaces, the only term that changes is the effective mass of the electron, which is $m_c = m_t$ for the circular constant energy projections and $m_e = \sqrt{m_t m_l}$ for the elliptical constant energy projections. The total ECD is the sum of the contributions from all of the constant energy surfaces. Due to the number of variables with the same alphabetical representations in different ECD equations, an additional set of subscript labels is applied to the variables H_R, y_R, and c_R. In addition to the subscript R, the first label denotes the dimensionality of the emitter system and the second denotes the relative location of the Fermi energy to the conduction band edge (p for positive or n for negative. For example, emission from a bulk emitter with $E_F > 0$ is labeled with $3p$.

4.4.1 ECD Equations: Conduction Band $E_F > 0$

When $E_F > 0$ for a silicon emitter, the semiconductor is considered degenerate and can be treated like a metal. As a result, band-bending is not significant in this case and is ignored. Since most emitted electrons are expected to come from energy states very close to the emission reference level in NU emitters, the transmission coefficients are expanded about $W = W_R$. In addition, band structure corrections give rise to another transmission function term $D(F, \gamma_n W)$, which when expanded about $W = W_R$, generates different expansion coefficients. For NC emitters, no expansion of the transmission coefficients is required. This leads to the expressions for the transmission coefficients for emitters with $E_F > 0$:

$$D_{NU}(F, W) = \exp\left[-\frac{B}{\gamma_a F}\nu[y_{R,p}] H_{R,p}^{3/2}\right]\exp[c_{R,p}(H_{R,p} - H)] \tag{4.7a}$$

$$D_{NU}(F, \gamma_n W) = \exp\left[-\frac{B}{\gamma_a F}\nu[\bar{y}_{R,p}] \bar{H}_{R,p}^{3/2}\right]\exp[\gamma_n \bar{c}_{R,p}(H_{R,p} - H)] \tag{4.7b}$$

where

$$\begin{aligned}
\gamma_n &= 1 - \frac{m_n}{m_0} \\
H_{R,p} &= \phi + E_F - W_R \\
c_{R,p} &= \frac{3B}{2\gamma_a F} t\left[y_{R,p}\right]\sqrt{H_{R,p}} \\
y_{R,p} &= \frac{v}{H_{R,p}}\sqrt{\frac{e^3 \gamma_a F}{4\pi\epsilon_0}}
\end{aligned} \tag{4.8}$$

A bar over the variable denotes that W_R is replaced by $\gamma_n W_R$ and γ_a is the field enhancement factor at the apex of the emitter tip. For the circular constant energy projections, γ_n is replaced by $\gamma_c = 1 - \frac{m_t}{m_0}$ and for the elliptical constant energy projections, it is replaced by $\gamma_e = 1 - \frac{\sqrt{m_t m_l}}{m_0}$. Despite the additional physics incorporated into the model, the supply functions for each of the emitter geometries from Chapter 3 remain unaltered.

Bulk Emitter

Substituting Equation 4.7a, Equation 4.7b, and Equation 3.30a with $M = 2$ into Equation 4.6 and defining $H_{R,3p} = \phi$ yields the integral for determining the corrected ECD from a single constant energy surface of silicon:

$$\begin{aligned}
J_{bulk,p}\left(F,T\right) =& e\frac{4\pi m_0 k_B T}{h^3}\int_0^{\infty} \ln\left[1 + \exp\left[\frac{E_F - W}{k_B T}\right]\right] \\
&\times \left\{\exp\left[-b_{R,3p}\right]\exp\left[c_{R,3p}\left(W - E_F\right)\right]\right. \\
&\left.-\gamma_n \exp\left[-\bar{b}_{R,3p}\right]\exp\left[\gamma_n \bar{c}_{R,3p}\left(W - E_F\right)\right]\right\} dW.
\end{aligned} \tag{4.9}$$

The variables from the transmission functions are defined as follows:

$$\begin{aligned}
b_{R,3p} &= \frac{B}{\gamma_a F}\nu\left[\frac{v\sqrt{e^3\gamma_a F/4\pi\epsilon_0}}{\phi}\right]\phi^{3/2} \\
\bar{b}_{R,3p} &= \frac{B}{\gamma_a F}\nu\left[\frac{v\sqrt{e^3\gamma_a F/4\pi\epsilon_0}}{\phi+(1-\gamma_n)E_F}\right]\left(\phi+(1-\gamma_n)E_F\right)^{3/2} \\
c_{R,3p} &= \frac{3B}{2\gamma_a F}t\left[\frac{v\sqrt{e^3\gamma_a F/4\pi\epsilon_0}}{\phi}\right]\sqrt{\phi} \\
\bar{c}_{R,3p} &= \frac{3B}{2\gamma_a F}t\left[\frac{v\sqrt{e^3\gamma_a F/4\pi\epsilon_0}}{\phi+(1-\gamma_n)E_F}\right]\sqrt{\phi+(1-\gamma_n)E_F}
\end{aligned} \tag{4.10}$$

Performing the integration (see §3.1 of [54]) and taking the leading term of Stratton's Equation 24 gives

$$\begin{aligned}
J_{bulk,p}(F,T) =& e\frac{4\pi m_0}{h^3}\frac{c_{R,3p}\pi k_B T}{\sin\left[c_{R,3p}\pi k_B T\right]}\left\{1-\frac{c_{R,3p}}{\bar{c}_{R,3p}}\frac{\sin\left[c_{R,3p}\pi k_B T\right]}{\sin\left[\gamma_n\bar{c}_{R,3p}\pi k_B T\right]}\exp\left[b_{R,3p}-\bar{b}_{R,3p}\right]\right\} \\
& \times c_{R,3p}^{-2}\exp\left[-b_{R,3p}\right]
\end{aligned} \tag{4.11}$$

The total ECD is given by the sum of the ECD from all of the constant energy surfaces.

$$\begin{aligned}
J_{bulk,p}(F,T) = & e\frac{4\pi m_0}{h^3}\frac{c_{R,3p}\pi k_B T}{\sin\left[c_{R,3p}\pi k_B T\right]} \\
& \times\left\{6-2\frac{c_{R,3p}}{\bar{c}_{R,3pc}}\frac{\sin\left[c_{R,3p}\pi k_B T\right]}{\sin\left[\gamma_c\bar{c}_{R,3pc}\pi k_B T\right]}\exp\left[b_{R,3p}-\bar{b}_{R,3pc}\right]\right. \\
& \left.-4\frac{c_{R,3p}}{\bar{c}_{R,3pe}}\frac{\sin\left[c_{R,3p}\pi k_B T\right]}{\sin\left[\gamma_e\bar{c}_{R,3pe}\pi k_B T\right]}\exp\left[b_{R,3p}-\bar{b}_{R,3pe}\right]\right\}c_{R,3p}^{-2}\exp\left[-b_{R,3p}\right]
\end{aligned} \tag{4.12}$$

where the subscripts c and e indicate that γ_n should be replaced by γ_c and γ_e, respectively. As is discussed in §5.3.3, the band structure corrections per constant energy surface for silicon emitters with $E_F > 0$ are negligible and the total ECD can be

approximated as

$$J_{bulk,p}(F,T) \approx 6e\frac{4\pi m_0}{h^3}\frac{c_{R,3p}\pi k_B T}{\sin[c_{R,3p}\pi k_B T]}c_{R,3p}^{-2}\exp[-b_{R,3p}]. \tag{4.13}$$

NU Nanowall Emitter

The silicon ECD equation for the NU nanowall is derived in a parallel manner to §3.4.1, with the same kind of band structure corrections as in the bulk ECD equation. The total ECD for the NU nanowall emitter is

$$\begin{aligned} J_{wall,p}^{u}(F,T) = e&\frac{2}{L_x h^2}\frac{c_{R,2p}\pi k_B T}{\sin[c_{R,2p}\pi k_B T]} \\ &\times\sum_{\alpha_x}^{\infty}\delta_{\alpha_x}\left\{6-2\left(\gamma_c\frac{c_{R,2p}}{\bar{c}_{R,2pc}}\right)^{1/2}\frac{\sin[c_{R,2p}\pi k_B T]}{\sin[\gamma_c\bar{c}_{R,2pc}\pi k_B T]}\exp\left[b_{R,2p}-\bar{b}_{R,2pc}\right]\right. \\ &\left.-4\left(\gamma_e\frac{c_{R,2p}}{\bar{c}_{R,2pe}}\right)^{1/2}\frac{\sin[c_{R,2p}\pi k_B T]}{\sin[\gamma_e\bar{c}_{R,2pe}\pi k_B T]}\exp\left[b_{R,2p}-\bar{b}_{R,2pe}\right]\right\} \\ &\times c_{R,2p}^{-3/2}\exp[-b_{R,2p}] \end{aligned} \tag{4.14}$$

with the variables from the transmission functions defined as:

$$\begin{aligned} b_{R,2p} &= \frac{B}{\gamma_a F}\nu\left[\frac{v\sqrt{e^3\gamma_a F/4\pi\epsilon_0}}{\phi+E_{\alpha_x}}\right](\phi+E_{\alpha_x})^{3/2} \\ \bar{b}_{R,2p} &= \frac{B}{\gamma_a F}\nu\left[\frac{v\sqrt{e^3\gamma_a F/4\pi\epsilon_0}}{\phi+(1-\gamma_n)E_F+\gamma_n E_{\alpha_x}}\right](\phi+(1-\gamma_n)E_F+\gamma_n E_{\alpha_x})^{3/2} \\ c_{R,2p} &= \frac{3B}{2\gamma_a F}t\left[\frac{v\sqrt{e^3\gamma_a F/4\pi\epsilon_0}}{\phi+E_{\alpha_x}}\right]\sqrt{\phi+E_{\alpha_x}} \\ \bar{c}_{R,2p} &= \frac{3B}{2\gamma_a F}t\left[\frac{v\sqrt{e^3\gamma_a F/4\pi\epsilon_0}}{\phi+(1-\gamma_n)E_F+\gamma_n E_{\alpha_x}}\right]\sqrt{\phi+(1-\gamma_n)E_F+\gamma_n E_{\alpha_x}}. \end{aligned} \tag{4.15}$$

Just as for the bulk emitter, the band structure corrections here are negligible and the ECD equation can be approximated as:

$$J^{u}_{wall,p}(F,T) \approx 6e\frac{2}{L_x h^2}\frac{c_{R,2p}\pi k_B T}{\sin\left[c_{R,2p}\pi k_B T\right]}\sum_{\alpha_x}^{\infty}\delta_{\alpha_x} c_{R,2p}^{-3/2}\exp\left[-b_{R,2p}\right] \tag{4.16}$$

NU Nanowire Emitter

Also In a manner parallel to §3.4.1, the physically-complete ECD equation for the NU nanowire emitter is derived:

$$\begin{aligned} J^{u}_{wire,p}(F,T) = {} & e\frac{2}{A_e h}\frac{c_{R,1p}\pi k_B T}{\sin\left[c_{R,1p}\pi k_B T\right]} \\ & \times \sum_{\alpha}^{\infty}\delta_{\alpha}\left\{6 - 2\gamma_c\frac{\sin\left[c_{R,1p}\pi k_B T\right]}{\sin\left[\gamma_c \bar{c}_{R,1pc}\pi k_B T\right]}\exp\left[b_{R,1p} - \bar{b}_{R,1pc}\right]\right. \\ & \left. -4\gamma_e\frac{\sin\left[c_{R,1p}\pi k_B T\right]}{\sin\left[\gamma_e \bar{c}_{R,1pe}\pi k_B T\right]}\exp\left[b_{R,1p} - \bar{b}_{R,1pe}\right]\right\} c_{R,1p}^{-3/2}\exp\left[-b_{R,1p}\right]. \end{aligned} \tag{4.17}$$

with the variables from the transmission functions defined as

$$\begin{aligned} b_{R,1p} &= \frac{B}{\gamma_a F}\nu\left[\frac{v\sqrt{e^3\gamma_a F/4\pi\epsilon_0}}{\phi + E_{t,\alpha}}\right](\phi + E_{t,\alpha})^{3/2} \\ \bar{b}_{R,1p} &= \frac{B}{\gamma_a F}\nu\left[\frac{v\sqrt{e^3\gamma_a F/4\pi\epsilon_0}}{\phi + (1-\gamma_n)E_F + \gamma_n E_{t,\alpha}}\right](\phi + (1-\gamma_n)E_F + \gamma_n E_{t,\alpha})^{3/2} \\ c_{R,1p} &= \frac{3B}{2\gamma_a F}t\left[\frac{v\sqrt{e^3\gamma_a F/4\pi\epsilon_0}}{\phi + E_{t,\alpha}}\right]\sqrt{\phi + E_{t,\alpha}} \\ \bar{c}_{R,1p} &= \frac{3B}{2\gamma_a F}t\left[\frac{v\sqrt{e^3\gamma_a F/4\pi\epsilon_0}}{\phi + (1-\gamma_n)E_F + \gamma_n E_{t,\alpha}}\right]\sqrt{\phi + (1-\gamma_n)E_F + \gamma_n E_{t,\alpha}}. \end{aligned} \tag{4.18}$$

The band structure effects are negligible for parameters relevant to field emission and the NU nanowire ECD equation can be approximated as

$$J^{u}_{wire,p}(F,T) \approx 6e\frac{2}{A_e h}\frac{c_{R,1p}\pi k_B T}{\sin\left[c_{R,1p}\pi k_B T\right]}\sum_{\alpha}^{\infty}\delta_{\alpha} c_{R,1p}^{-3/2}\exp\left[-b_{R,1p}\right]. \tag{4.19}$$

For a rectangular nanowire,

$$\begin{aligned} E_{t,\alpha} &= E_{\alpha_x} + E_{\alpha_y} \\ A_e &= L_x L_y \end{aligned} \tag{4.20}$$

while for a cylindrical nanowire

$$\begin{aligned} E_{t,\alpha} &= E_{\alpha_{m,n}} \\ A_e &= \pi a^2. \end{aligned} \tag{4.21}$$

NC Nanowall Emitter

For the case of a NC nanowall emitter, the corrected ECD for a single constant energy surface can be found by substituting Equation 3.53 and the unexpanded transmission functions into Equation 4.6

$$\begin{aligned} J^c_{wall,p}(F,T) =& e\frac{2\pi k_B T}{L_z h^2}\sum_q^\infty \delta_q \sqrt{2m_0 W_q} \ln\left[1+\exp\left[\frac{E_F - W_q}{k_B T}\right]\right] \\ & \times\left\{1-\gamma_n \exp\left[-\frac{B}{\gamma_a F}\left(\bar{H}_n^{3/2} - H^{3/2}\right)\right]\right\}\exp\left[-\frac{B}{\gamma_a F}H^{3/2}\right] \end{aligned} \tag{4.22}$$

where $H = \phi + E_F - W_q$ and $\bar{H}_n = \phi + E_F - \gamma_n W_q$. Totaling the contributions from each of the constant energy surfaces and summing over all normal electron subbands gives the total ECD from the nanowall:

$$\begin{aligned} J^c_{wall,p}(F,T) =& e\frac{2\pi k_B T}{L_z h^2}\sum_{q=1}^\infty \delta_q \sqrt{2m_0 W_q} \ln\left[1+\exp\left[\frac{E_F - W_q}{k_B T}\right]\right] \\ & \times\left\{6 - 2\gamma_c \exp\left[-\frac{B}{\gamma_a F}\left(\bar{H}_c^{3/2} - H^{3/2}\right)\right]\right. \\ & \left. -4\gamma_e \exp\left[-\frac{B}{\gamma_a F}\left(\bar{H}_e^{3/2} - H^{3/2}\right)\right]\right\}\exp\left[-\frac{B}{\gamma_a F}H^{3/2}\right] \end{aligned} \tag{4.23}$$

where the subscripts c and e indicate that γ_n should be replaced by γ_c and γ_e.

NC Nanowire Emitter

The derivation of the NC nanowire ECD equation consists of substituting the approximate supply function from Equation 3.56, which was derived for $T = 0$ K, and the unexpanded transmission functions into Equation 4.6:

$$\begin{aligned} J^{c}_{wire,p}(F) =& e\frac{8}{L_e dh}\sum_{q}^{\infty}\delta_q\sum_{\alpha}^{\infty}\delta_\alpha\sqrt{W_q\left(E_F - W_q - E_{t,\alpha}\right)} \\ &\times\left\{1-\gamma_n\exp\left[-\frac{B}{\gamma_a F}\left(\bar{H}_n^{3/2}-H^{3/2}\right)\right]\right\}\exp\left[-\frac{B}{\gamma_a F}H^{3/2}\right] \end{aligned} \tag{4.24}$$

The total ECD from all electron subbands and constant energy surfaces is

$$\begin{aligned} J^{c}_{wire,p}(F) = & e\frac{8}{L_e dh}\sum_{q}^{\infty}\delta_q\sum_{\alpha}^{\infty}\delta_\alpha\sqrt{W_q\left(E_F - W_q - E_{t,\alpha}\right)} \\ &\times\left\{6-2\gamma_c\exp\left[-\frac{B}{\gamma_a F}\left(\bar{H}_c^{3/2}-H^{3/2}\right)\right]-4\gamma_e\exp\left[-\frac{B}{\gamma_a F}\left(\bar{H}_e^{3/2}-H^{3/2}\right)\right]\right\} \\ &\times\exp\left[-\frac{B}{\gamma_a F}H^{3/2}\right]. \end{aligned} \tag{4.25}$$

For the rectangular nanowire,

$$\begin{aligned} E_{t,\alpha} &= E_{\alpha_x} \\ d &= 2L_z \\ L_e &= L_x. \end{aligned} \tag{4.26}$$

It should be noted that since the supply function was derived for $T = 0$ K, this ECD equation is not strictly appropriate for describing emission at finite temperatures. However, it can still serve as a good approximation for the ECD at temperatures relevant to field emission.

4.4.2 ECD Equations: Conduction Band $E_F < 0$

When $E_F < 0$ in the bulk, a semiconductor emitter can no longer be treated like a metal and most of the emitted electrons are expected to come from states close in energy to the conduction band edge, $W_R = 0$. As mentioned in §2.3.2, band bending for non-degenerate semiconductors is non-negligible and may lead to a potentially significant current component from bound states in the accumulation layer. The equations derived below do not include band bending and the formation of an accumulation layer and thus are not physically realistic for predicting the ECD from a semiconductor emitter with $E_F < 0$ in the bulk. Instead, the equations are more of an exercise in calculating the band structure corrections for semiconductor emitters with $E_F < 0$ in the bulk and are meant to serve as a lower limit on the ECD from a semiconductor emitter. Also, the validity of the assumption that the total ECD from semiconductor emitters is the sum of a FN-type ECD and a NC ECD is currently unknown and will be investigated, along with ECD equations for emission from the accumulation layer of quantum-confined emitters, in future work. An equation predicting the ECD from a single conduction valley of the accumulation layer of a bulk silicon emitter is derived in Appendix D.

Just as for the $E_F > 0$ case, the band structure corrections necessitate the specification of two transmission functions, both expanded about $W = 0$:

$$D_{NU}\left(F, W\right) = \exp\left[-b_{R,n}\right] \exp\left[c_{R,n} W\right] \tag{4.27a}$$

$$D_{NU}\left(F, \gamma_n W\right) = \exp\left[-b_{R,n}\right] \exp\left[\gamma_n c_{R,n} W\right] \tag{4.27b}$$

where

$$
\begin{aligned}
b_{R,n} &= \frac{B}{\gamma_a F}\nu\left[y_{R,n}\right]\chi_e^{3/2} \\
c_{R,n} &= \frac{3B}{2\gamma_a F}t\left[y_{R,n}\right]\sqrt{\chi_e} \\
y_{R,n} &= \frac{v}{\chi_e}\sqrt{\frac{e^3 F}{4\pi\epsilon_0}}
\end{aligned}
\tag{4.28}
$$

Unlike for emission from degenerate semiconductors and metals, transverse quantum confinement does not influence the barrier height seen by tunneling electrons, which is the electron affinity of silicon, χ_e. Due to the reference barrier height being independent of the emitter geometry, the above expansion coefficients remain the same for all NU derivations.

Bulk Emitter

Substituting Equation 4.27a, Equation 4.27b, and Equation 3.30a with $M = 2$ into Equation 4.6 yields the integral for determining the corrected ECD from a single constant energy surface of a bulk silicon emitter:

$$
\begin{aligned}
J_{bulk,n}\left(F,T\right) =& e\frac{4\pi m_0 k_B T}{h^3}\int_0^\infty \ln\left[1+\exp\left[\frac{E_F - W}{k_B T}\right]\right] \\
&\times\left\{\exp\left[-b_{R,n}\right]\exp\left[c_{R,n}W\right] - \gamma_n\exp\left[-b_{R,n}\right]\exp\left[\gamma_n c_{R,n}W\right]\right\}dW.
\end{aligned}
\tag{4.29}
$$

Performing the integration (see section 3.2 of [54]) and taking the first term of the summation in Stratton's Equation 36:

$$
J_{bulk,n}\left(F,T\right) \approx e\frac{4\pi m_0\left(k_B T\right)^2}{h^3}\frac{1-\gamma_n}{\left(1-c_{R,n}k_B T\right)\left(1-\gamma_n c_{R,n}k_B T\right)}\exp\left[\frac{E_F}{k_B T} - b_{R,n}\right]
\tag{4.30}
$$

Summing the contributions from all constant energy surfaces yields the total ECD from a bulk silicon emitter with a Fermi energy below the conduction band edge:

$$\begin{aligned} J_{bulk,n}(F,T) =& e\frac{4\pi m_0}{h^3}\frac{(k_BT)^2}{1-c_{R,n}k_BT} \\ &\times\left\{\frac{2}{1-\gamma_c c_{R,n}k_BT}\frac{m_t}{m_0}+\frac{4}{1-\gamma_e c_{R,n}k_BT}\frac{\sqrt{m_tm_l}}{m_0}\right\}\exp\left[\frac{E_F}{k_BT}-b_{R,n}\right] \end{aligned} \tag{4.31}$$

NU Nanowall Emitter

While the supply function for a bulk emitter can be expressed in closed form, the supply function for the nanowall cannot. However, for a non-degenerate semiconductor, Boltzmann statistics are a good approximation for electronic state occupation probability and the Fermi-Dirac distribution can be replaced by $\exp\left[-\frac{E-E_F}{k_BT}\right]$. With this substitution, the new supply function becomes

$$N_{\alpha_x}(W,T) = e\frac{2}{h^2L_x}\sqrt{2\pi m_0k_BT}\exp\left[-\frac{W+E_{\alpha_x}-E_F}{k_BT}\right]dW. \tag{4.32}$$

Inserting the expanded transmission functions for $E_F < 0$ and the above supply function into Equation 4.6 results in

$$\begin{aligned} J^u_{wall,n,\alpha_x}(F,T) =& e\frac{2}{h^2L_x}\sqrt{2\pi m_0k_BT}\exp\left[\frac{E_F-E_{\alpha_x}}{k_BT}\right]\int_0^\infty \exp\left[-\frac{W}{k_BT}\right] \\ &\times\{\exp[-b_{R,n}]\exp[c_{R,n}W]-\gamma_n\exp[-b_{R,n}]\exp[\gamma_nc_{R,n}W]\}\,dW. \end{aligned} \tag{4.33}$$

Performing the integration produces

$$\begin{aligned} J^u_{wall,n,\alpha_x}(F,T) \approx& e\frac{2}{h^2}\sqrt{2\pi m_0}\frac{(k_BT)^{3/2}}{(1-c_{R,n}k_BT)(1-\gamma_nc_{R,n}k_BT)}\exp\left[\frac{E_F-E_{n_x}}{k_BT}\right] \\ &\times\{1-\gamma_n\}\exp[-b_{R,n}] \end{aligned} \tag{4.34}$$

Adding the contributions from all constant energy surfaces and summing over all subbands gives the total ECD from the nanowall

$$J^u_{wall,n}(F,T) \approx e\frac{2}{L_x h^2}\sqrt{2\pi m_0}\frac{(k_BT)^{3/2}}{1-c_{R,n}k_BT}\exp\left[\frac{E_F-E_{\alpha_x}}{k_BT}\right] \times\left\{\frac{2}{1-\gamma_c c_{R,n}k_BT}\frac{m_t}{m_0}+\frac{4}{1-\gamma_e c_{R,n}k_BT}\frac{\sqrt{m_t m_l}}{m_0}\right\} \times\exp\left[\frac{E_F}{k_BT}-b_{R,n}\right]\sum_{\alpha_x=1}^{\infty}\delta_{\alpha_x}\exp\left[-\frac{E_{\alpha_x}}{k_BT}\right] \tag{4.35}$$

NU Nanowire Emitter

For consistency with the previous equations, the supply function for the nanowire is also derived using Boltzmann statistics:

$$N_\alpha(W,T) = e\frac{2}{hA_e}\exp\left[-\frac{W+E_{t,\alpha}-E_F}{k_BT}\right]dW. \tag{4.36}$$

Inserting the expanded transmission functions for $E_F < 0$ and the above supply function into Equation 4.6 leads to

$$J^u_{wire,n,\alpha}(F,T) = e\frac{2}{hA_e}\exp\left[\frac{E_F-E_{t,\alpha}}{k_BT}\right]\int_0^{\infty}\exp\left[-\frac{W}{k_BT}\right] \times\left\{\exp\left[-b_{R,n}\right]\exp\left[c_{R,n}W\right]-\gamma_n\exp\left[-b_{R,n}\right]\exp\left[\gamma_n c_{R,n}W\right]\right\}dW. \tag{4.37}$$

Integrating over all W gives

$$J^u_{wire,n,\alpha}(F,T) \approx e\frac{2}{hA_e}\frac{k_BT}{(1-c_{R,n}k_BT)(1-\gamma_n c_{R,n}k_BT)} \times\exp\left[\frac{E_F-E_{t,\alpha}}{k_BT}\right]\{1-\gamma_n\}\exp\left[-b_{R,n}\right] \tag{4.38}$$

Adding the contributions from all constant energy surfaces and summing over all subbands gives the total ECD from the nanowire

$$\begin{aligned}J^{u}_{wire,n}\left(F,T\right) \approx & e\frac{2}{A_e h}\frac{k_BT}{1-c_{R,n}k_BT} \\ & \times\left\{\frac{2}{1-\gamma_c c_{R,n}k_BT}\frac{m_t}{m_0}+\frac{4}{1-\gamma_e c_{R,n}k_BT}\frac{\sqrt{m_t m_l}}{m_0}\right\} \\ & \times\exp\left[\frac{E_F}{k_BT}-b_{R,n}\right]\sum_{\alpha}\delta_\alpha\exp\left[-\frac{E_{t,\alpha}}{k_BT}\right].\end{aligned} \tag{4.39}$$

For a rectangular nanowire,

$$\begin{aligned}E_{t,\alpha} &= E_{\alpha_x}+E_{\alpha_y} \\ A_e &= L_x L_y\end{aligned} \tag{4.40}$$

and for a cylindrical nanowire,

$$\begin{aligned}E_{t,\alpha} &= E_{\alpha_{m,n}} \\ A_e &= \pi a^2.\end{aligned} \tag{4.41}$$

NC Nanowall Emitter

Due to the lack of expansion of the transmission functions for normally-confined systems, the form of the equation does not change for $E_F < 0$. Therefore, the ECD equation for the NC silicon nanowall is given by Equation 4.23, but with $\phi + E_F$ replaced by χ_e in the transmission function:

$$\begin{aligned}J^{c}_{wall,n}\left(F,T\right) = & e\frac{2\pi k_BT}{L_z h^2}\sqrt{2m_0}\sum_{q=1}^{\infty}\delta_q\sqrt{W_q}\ln\left[1+\exp\left[\frac{E_F-W_q}{k_BT}\right]\right] \\ & \times\left\{6-2\gamma_c\exp\left[-\frac{B}{\gamma_a F}\left(\bar{H}_c^{3/2}-H^{3/2}\right)\right]\right. \\ & \left.-4\gamma_e\exp\left[-\frac{B}{\gamma_a F}\left(\bar{H}_e^{3/2}-H^{3/2}\right)\right]\right\}\exp\left[-\frac{B}{\gamma_a F}H^{3/2}\right]\end{aligned} \tag{4.42}$$

where

$$
\begin{aligned}
H &= \chi_e - W_q \\
H_n &= \chi_e - \gamma_n W_q
\end{aligned}
\tag{4.43}
$$

NC Nanowire Emitter

Using Maxwell-Boltzmann statistics, the supply function for the NC silicon nanowire is

$$
N_{q,\alpha}\left(W_q, T\right) = \frac{4}{dhL_e}\sqrt{\pi k_B T W_q}\exp\left[\frac{E_F - W_q - E_{t,\alpha}}{k_B T}\right]. \tag{4.44}
$$

The total ECD from the nanowire is obtained by incorporating the transmission function and band structure corrections and summing over all subbands:

$$
\begin{aligned}
J^c_{wire,n}\left(F,T\right) =& e\frac{4}{L_e dh}\sqrt{\pi k_B T}\sum_q^{\infty}\delta_q\sum_\alpha^{\infty}\delta_\alpha\sqrt{W_q}\exp\left[\frac{E_F - W_q - E_{t,\alpha}}{k_B T}\right] \\
&\times\left\{6 - 2\gamma_c\exp\left[-\frac{B}{\gamma_a F}\left(\bar{H}_c^{3/2} - H^{3/2}\right)\right]\right. \\
&\left.-4\gamma_e\exp\left[-\frac{B}{\gamma_a F}\left(\bar{H}_e^{3/2} - H^{3/2}\right)\right]\right\}\exp\left[-\frac{B}{\gamma_a F}H^{3/2}\right]
\end{aligned}
\tag{4.45}
$$

For the rectangular nanowire,

$$
\begin{aligned}
E_{t,\alpha} &= E_{\alpha_x} \\
d &= 2L_z \\
L_e &= L_x.
\end{aligned}
\tag{4.46}
$$

4.5 Chapter Summary

In this chapter, correction factors for quantum-confined silicon emitters were derived and applied to the elementary framework to create a more physically-complete treatment of field emission. The treatment for silicon consists of incorporating the Schottky-Nordheim barrier, finite temperatures, and band structure effects into the

elementary framework derived in Chapter 3. Approximating the elliptical constant energy projections of silicon as circles with a new effective mass and employing a quasi-continuum approximation allows for Stratton's band structure corrections to be applied to quantum-confined silicon field emitters. With these correction factors, ECD equations for emission from silicon were derived for Fermi energies above and below the edge of the conduction band for each of the emitter geometries considered in Chapter 3.

Chapter 5

Analysis of the Emitted Current Density from Quantum-Confined Emitters

5.1 Introduction

Having derived equations predicting the emitted current density from emitters of reduced dimensionality and various geometries, the next step is to investigate how these equations differ from the bulk emitter ECD equations. In order to gain a qualitative understanding of how quantum confinement of the electron supply affects the emitted current density, ECD equations from the elementary model are compared to the elementary FN equation as a function of the emitter dimensions. In addition, the influence of emission at finite temperatures, the incorporation of the Schottky-Nordheim barrier potential, and band structure effects on the total ECD for silicon emitters with $E_F > 0$ and $E_F < 0$ are analyzed. The validity of using FN plots for analyzing field emission data from quantum-confined emitters is investigated and an alternative method for data analysis for quantum-confined emitters is proposed.

Finally, ECD equations are compared to field emission data from vertical, single-layer graphene and single carbon nanotube emitters in order to test the validity of the framework.

5.2 ECD as a Function of Emitter Dimensions: Elementary Model

In this section, the emitted current density from the elementary ECD equations derived in §3.4 are compared to the elementary FN equation (Equation 2.6) as a function of the emitter dimensions. The ECD equations are normalized to the elementary FN equation and plotted versus the appropriate quantum well width(s). The effects of transverse quantum confinement and normal quantum confinement on the normalized ECDs are analyzed as a function of the quantum well width(s) with $\gamma_a = 1$ and the physical mechanisms behind the behavior of the normalized ECD plots are discussed. In order to investigate the competing effects of quantum confinement of the electron supply and field enhancement at the emitter tip, plots of the ECD versus quantum well width(s) under a constant applied voltage are presented and discussed.

5.2.1 Effects of Transverse Quantum Confinement

Figure 5-1 shows the normalized elementary ECD equations from the NU nanowall, NU rectangular nanowire, and NU cylindrical nanowire as a function of the appropriate quantum well width(s) with $\gamma_a = 1$. As the well width decreases, the ECD decreases exponentially, eventually reaching zero. As the well width increases towards infinity, the ECD from each of the emitter geometries asymptotically approaches the elementary Fowler-Nordheim equation ECD (FN limit).

As discussed in §3.2.2, quantum confinement of the electron supply discretizes electron energies, separating the formerly-continuous band of electrons into subbands.

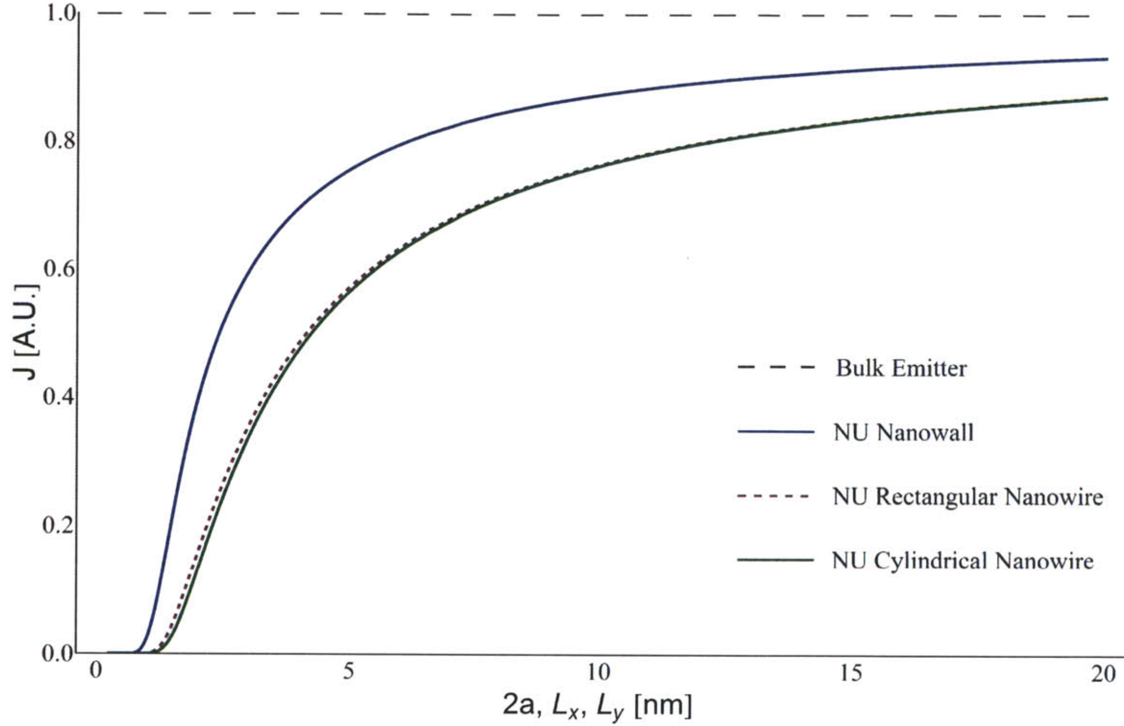

Figure 5-1: ECD from the NU nanowall emitter, NU rectangular nanowire emitter, and NU cylindrical nanowire emitter as a function of L_x, $L_x = L_y$, and $2a$ respectively, with $\phi = 5$ eV and $E_F = 10$ eV at $F = 2 \times 10^7$ V/cm.

At $T = 0$ K, no electronic states may be occupied at energies above E_F, which limits the electron subbands that contribute to the total ECD to a finite number with energies below the Fermi energy. In the case of the NU nanowall, transverse quantum confinement fixes the x-directed electron kinetic energies at $E_{\alpha_x} = \alpha_x^2 h^2 / (8 m_0 L_x^2)$ within each subband α_x. As L_x decreases, the minimum kinetic energy of electrons in each subband increases and when E_x exceeds E_F the number of subbands contributing to emission is reduced by one. Fewer subbands of electrons contributing to emission leads to a lower total electron flux at the emitting surface and decreases the total ECD relative to a bulk emitter.

Changes in the transmission function due to transverse quantum confinement are also responsible for the reduced ECD of transversally-confined emitters. According to Equation 3.35 and Equation 3.38, the probability of an electron being transmitted through the potential barrier is a strong function of the electron normal energy $W =$

$E - E_t$, where E is the total kinetic energy of the electron and E_t is its transverse kinetic energy. In the bulk emitter case, all components of W and E_t are continuous and each can range from 0 to E_F. However, when a system is transversally quantum-confined, at least one component of the transverse energy becomes discretized and electrons in that dimension are limited to minimum kinetic energy values greater than zero. For the NU nanowall, within a given subband α_x, E_{t,min,α_x} is fixed at $E_{\alpha_x} = \alpha_x^2 h^2 / (8m_0 L_x^2)$ and the range of energy values available to W is reduced to $0 < W < E_F - E_{\alpha_x}$, also reducing W_R. The effect of reducing W_R in the transmission probability arises in the reference zero-field barrier height (Equation 3.36) of the expanded transmission function Equation 3.38, which becomes $H_{R,\alpha_x} = \phi + E_{\alpha_x}$ [41]. Therefore, limiting the normal electron energy to a lower maximum value in each subband reduces the maximum transmission probability of electrons in each subband relative to the bulk emitter case. Since the emitted current density is an exponential function of $H_R^{3/2}$ and E_{α_x} is a function of L_x^{-2}, the current density decreases with decreasing transverse well width approximately as $\exp[L_x^{-3}]$. Adding an additional degree of transverse quantum confinement, such as in the case of the NU nanowire, leads to a greater confinement energy term in $H_{R,\alpha}$ and further reduces the ECD.

A more realistic look at how the ECD of NU emitters changes with transverse emitter dimensions is gained by incorporating the effects of field enhancement at the emitter tip into the model. Using the floating sphere model (§C.1) for the NU cylindrical nanowire emitter, a plot of the total ECD versus quantum well radius for a constant applied electric field was constructed. Figure 5-2 shows that above a critical size, d_{peak}, decreasing the emitter width increases field enhancement at the emitter tip and the higher local electric field increases the ECD. Below d_{peak}, emission is limited by the supply of electrons to the barrier and the ECD decreases despite further increases in the local electric field at the emitter surface. As a result, there is an optimal set of transverse emitter dimensions that lead to the maximum-attainable

ECD for a given emitter geometry, height, and applied field.

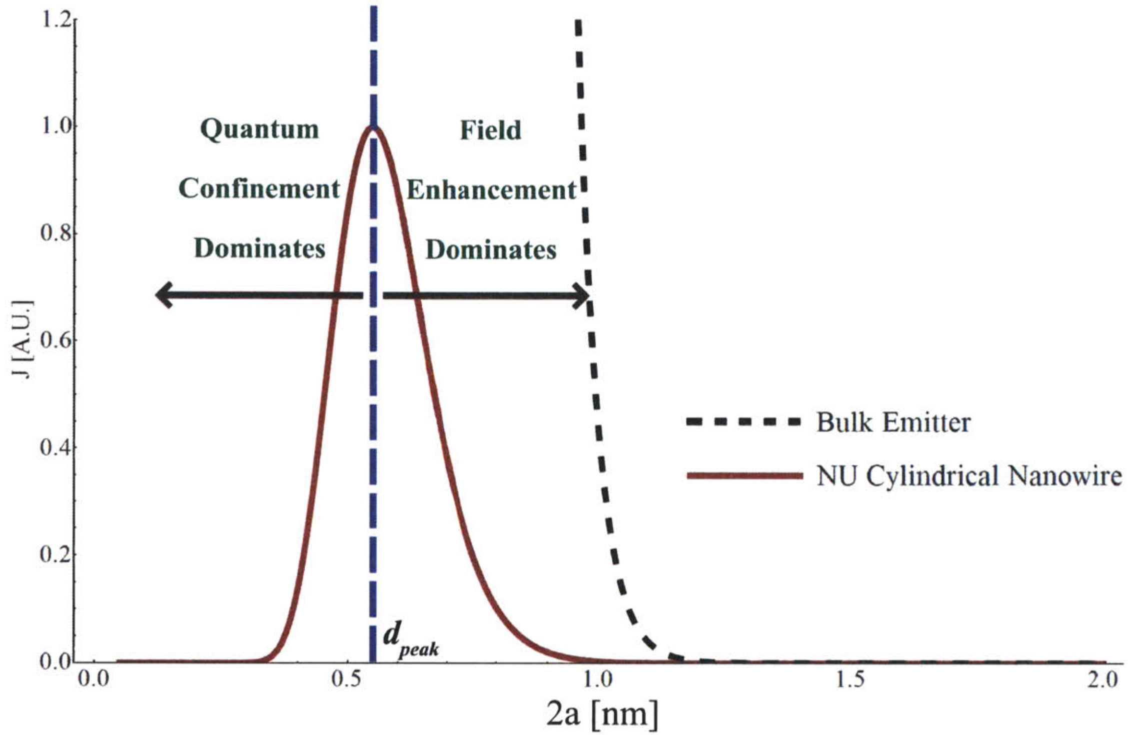

Figure 5-2: Normalized ECD of the NU cylindrical nanowire emitter and bulk emitter with γ_a defined by the floating sphere model, with a constant applied field far from the emitter surface of $F_M = 1.145 \times 10^5$ V/cm, $\phi = 5$ eV, $E_F = 10$ eV, and an emitter height of $l = 1$ μm. The peak in the ECD curve occurs at $a = d_{peak}$, right of which field enhancement dominates the ECD and left of which quantum confinement dominates the ECD.

5.2.2 Normal Quantum Confinement

The ECD of the elementary NC nanowall and NC rectangular nanowire normalized to the elementary Fowler-Nordheim equation as a function of the well width(s) with $\gamma_a = 1$, as shown in Figure 5-3. The effects of normal quantum confinement on the ECD are analyzed within the NC nanowall system. The analysis is simplified if the normal well width, L_z, is sufficiently small such that the highest-energy subband ,W_Q, makes the dominant contribution to the total ECD. Under this assumption, J^c_{wall} is proportional to the product of the supply function and the transmission function for

the dominant subband (Q):

$$J^c_{wall,Q}(F) \simeq e\frac{4\pi m_0}{h^3}\frac{2W_Q[L_z]}{Q} \times [E_F - W_Q[L_z]] \exp\left[-\frac{B}{F}(\phi + E_F - W_Q[L_z])^{3/2}\right] \tag{5.1}$$

The plot of the normalized ECD against L_z in Figure 5-3 raises two important questions: i) Why does the emitted current density oscillate as a function of L_z and ii) What physical mechanisms determine the shape of the ECD's envelope function?

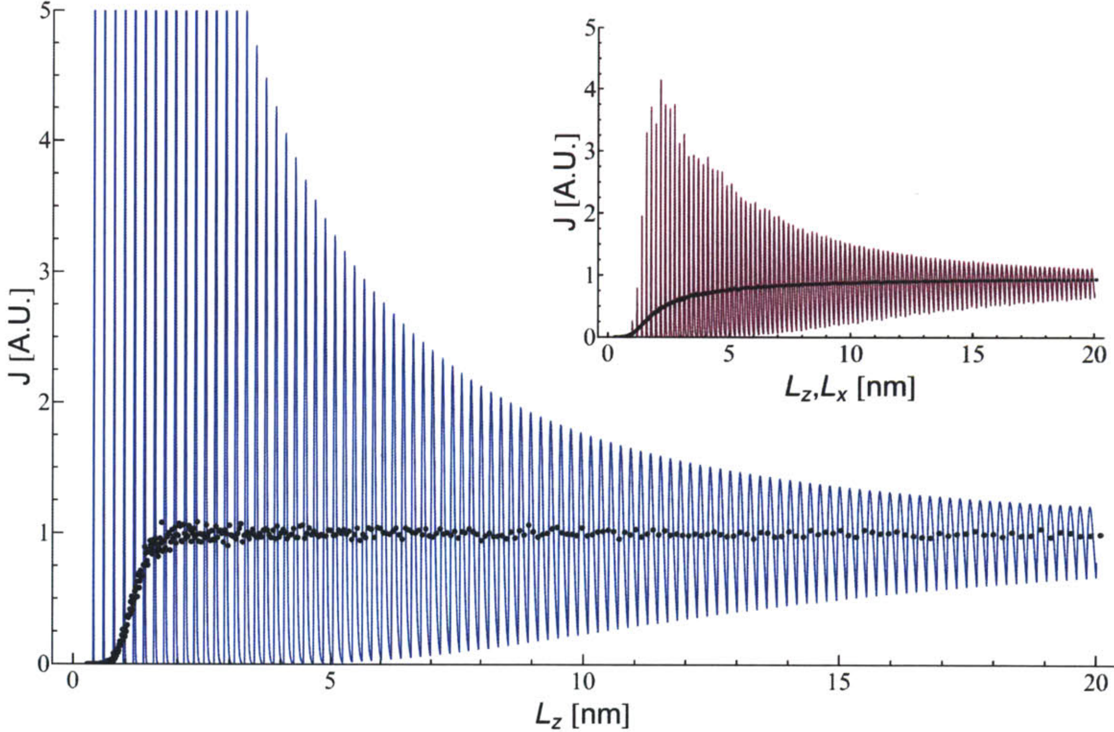

Figure 5-3: ECD from the NC nanowall and NC rectangular nanowire as a function of L_z and $L_x = L_z$ respectively, with $\phi = 5$ eV and $E_F = 10$ eV at $F = 2\times 10^7$ V/cm. Plot points represent the average ECD per well width, calculated from a Gaussian distribution of well widths with a mean of the well width and standard deviation of 10% of the mean.

The oscillatory nature of the emitted current density is a direct result of the migration of the subband energies with varying normal well width and the lack of occupied electronic states above the Fermi energy at $T = 0$ K. If only one subband is

being considered, such as in Equation 5.1, the energy of the subband can be shifted by changing L_z; thus W_Q may be treated as a continuous variable as a function of L_z, bounded by 0 and E_F. Figure 5-4 illustrates the effect that shifting the subband energies via changes in L_z has on the ECD. The plot on the left shows the ECD from the dominant subband of the NC nanowall as a function of L_z, with the ECD noted at four well widths labeled L_{z1}, L_{z2}, L_{z3}, and L_{z4}. Creating infinite square wells with these well widths and noting the location of the dominant subband energy W_Q and the next highest energy W_{Q+1} (outside the well) relative to the Fermi energy in each of the wells leads to the center diagram. In the right diagram, the average emitted electron flux is plotted versus the W_Q, with the normal energies W_{Q1}, W_{Q2}, W_{Q3}, and W_{Q4} corresponding to the value of W_Q for each of the well widths in the center diagram. According to the diagrams, as L_z increases, the ECD from the subband (proportional to the average emitted electron flux) increases until L_{z2}, then decreases until L_{z4}. For normal well widths larger than L_{z4}, a new electron subband with energy just below E_F begins to emit and becomes the new dominant emitting subband. This new subband $(Q+1)$ displays the same ECD behavior as was seen for the previous dominant subband (Q), causing oscillations in the total ECD to occur.

The envelope function that serves as the upper bound of the NC nanowall ECD increases as L_z decreases due to the reduced distance traveled between tunneling attempts for normally-confined emitters. The smaller normal well width translates into a reduced travel distance between collisions with the emitting surface and greatly increases the attempt frequency of electrons at the potential barrier, producing an ECD that may exceed that of the bulk emitter case for certain normal well widths. For well widths below a transition point that marks the boundary between emitters comprised of 3D and 2D electron gases, single subbands become increasingly more dominant contributors to the total ECD. Given that the total ECD is comprised of the sum of the contributions from all emitting subbands, as fewer subbands contribute

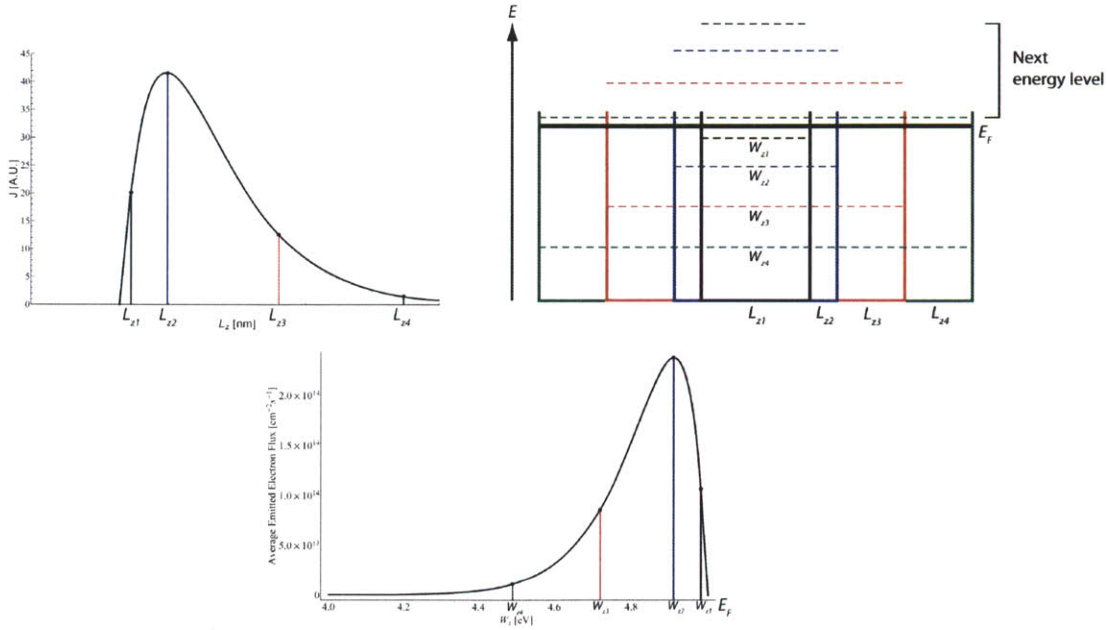

Figure 5-4: ECD from the first subband of an NC nanowall emitter with selected quantum well widths labeled (top left), quantum wells with widths equal to the labels in the ECD plot and the corresponding normal energy level in each well (top right), and the average number of emitted electrons from the subband as a function of the normal energy W_Q (bottom).

significantly, the total ECD decreases to values closer to zero each time the dominant subband energy equals the Fermi energy, for which $J^c_{wall,Q} = 0$. When the emitter dimensions are small enough that the energy of the last contributing subband is raised to E_F, emission from the emitter ceases completely.

Although predicted by the model, the oscillatory behavior of the ECD from normally confined systems cannot currently be linked with any physical systems. Instead, an expected value for the ECD can be calculated by averaging the ECD from a Gaussian distribution of normal well widths (simulating surface roughness) with a mean of L_z and standard deviation of 10% of the mean. For both the NC nanowall and NC rectangular nanowire, the expected value of the ECD exhibits a behavior similar to that of the NU emitters in Figure 5-1. For both NC systems, at small normal well widths the expected value of the ECD drops exponentially towards zero and for large normal well widths, the ECD approaches the FN limit, as shown by the black points

on both plots in Figure 5-3.

5.3 ECD as a Function of the Quantum Well Width: Silicon ECD Equations

The silicon ECD equations incorporate the effects of emission at finite temperatures, the Schottky-Nordheim barrier potential, and band structure corrections. In this section, the effects of each of these physical phenomena on the ECD are analyzed.

5.3.1 Finite Temperature

Within the elementary framework ($T = 0$ K), any electron subbands with energies greater than the Fermi energy were forbidden to contribute to emission due to zero probability of electrons occupying those states. When considering Fermi-Dirac statistics at finite temperatures, all energies above E_F have a non-zero electron occupation probability and the total ECD is a sum over all electron subbands. However, due to the occupation probabilities of states more than $3k_BT$ above the Fermi energy being negligible at typical cold field emission temperatures, there is only a small additional contribution to the ECD from subbands just above E_F for NU emitters with $E_F > 0$. Because $3k_BT \approx 0.075$ eV at $T = 300$ K, the additional ECD contributions due to finite temperature are only significant when multiple subband energies are in the range $E_F < E_\alpha < E_F + 3k_BT$, which could occur if E_F is close to the conduction band edge and the emitter is large enough that there are many subbands near the conduction band edge. For NC emitters with a $E_F > 0$, raising the temperature causes the distribution of the average number of emitted electrons per subband in Figure 5-4 to broaden, replacing the oscillating subband ECD segments with more linear ones.

Unlike emission from metals and semiconductors with $E_F > 0$, emission from the

conduction band of semiconductors with $E_F < 0$ cannot occur at $T = 0$ K. Without thermal energy to promote electrons to the conduction band from either the valence band or donor levels, no emission can occur. As a result, the ECDs for semiconductor emitters with $E_F < 0$ are highly dependent upon the temperature of the emitter and are reduced to zero at $T = 0$ K. Although the qualitative characteristics of NU emitter ECD plots with $E_F < 0$ are the same as those of the NU emitter ECD plots with $E_F > 0$, non-degenerate semiconductor emitters suffer from a severely reduced ECD due to the emitting subbands being at least $3k_BT$ above E_F. The position of the Fermi energy far below all emitting subbands is also responsible for the elimination of oscillations in the ECD plots for NC silicon emitters. Since the oscillations were a result of subbands with normal energies below E_F emitting more strongly than subbands with normal energies above E_F, having a system in which all emitting subbands have normal energies far above E_F reduces the discrepancy between subband ECD contributions and leads to a smoothed ECD for NC silicon emitters.

5.3.2 Schottky-Nordheim Barrier

The incorporation of quantum-confinement into models of field emission directly affects the values of the argument of the barrier shape correction factor ν and the decay rate correction factor t. For NU emitters with $E_F > 0$, the argument y_R is dependent upon the reference zero-field barrier height of the electrons in the subband:

$$y_{R,\alpha} = \sqrt{\frac{e^3 \gamma_a F}{4\pi\epsilon_0}} H_{R,\alpha}^{-1} \tag{5.2}$$

The introduction of transverse quantum confinement increases $H_{R,\alpha}$ and, in turn, decreases the value of $y_{R,\alpha}$. A reduced $y_{R,\alpha}$ pushes the values for $\nu\,[y_{R,\alpha}]$ and $t\,[y_{R,\alpha}]$ closer towards unity (see Table 2.1), diminishing the effect of both of these correction

factors relative to the bulk emitter case. This is physically intuitive, as most emission is occurring at energy levels that are far from the top of the rounded potential barrier where the effects of a rounded barrier have little geometric influence on the transmission probably.

Since the transmission function for NU emitters with $E_F < 0$ is expanded about the conduction band edge, the reference zero-field barrier height for emitters is the electron affinity, leading to

$$y_R = \sqrt{\frac{e^3\gamma_a F}{4\pi\epsilon_0}}\chi_e^{-1} \tag{5.3}$$

for all emitters, independent of their dimensionality. As a result, ν and t do not change form between bulk emitters and transversally-confined NU emitters.

Since the transmission function remains unexpanded for emission from NC emitters with $E_F > 0$ and $E_F < 0$, y_q depends heavily on the normal energy of the emitter

$$y_q = \sqrt{\frac{e^3\gamma_a F}{4\pi\epsilon_0}}\left(\chi_e - W_q\right)^{-1} \tag{5.4}$$

where W_q is the normal energy of electrons in subband q. Due to ν for the bulk emitter being fixed at a value less than or equal to ν for NC emitters ($H_q \geq \phi$), the transmission probability for electrons in a bulk emitter will be greater than or equal to the transmission probability in NC emitters.

5.3.3 Band Structure Effects

The band structure corrections for NU and NC, n-type semiconductor emitters with $E_F > 0$ and $E_F < 0$ have varying degrees of influence on the total ECD. For NU emitters with $E_F > 0$ the band structure corrections for a single constant energy surface take the form

$$\lambda_B = 1 - G\frac{\sin\left[c\pi k_B T\right]}{\sin\left[\gamma_n \bar{c}\pi k_B T\right]}\exp\left[b - \bar{b}\right] \tag{5.5}$$

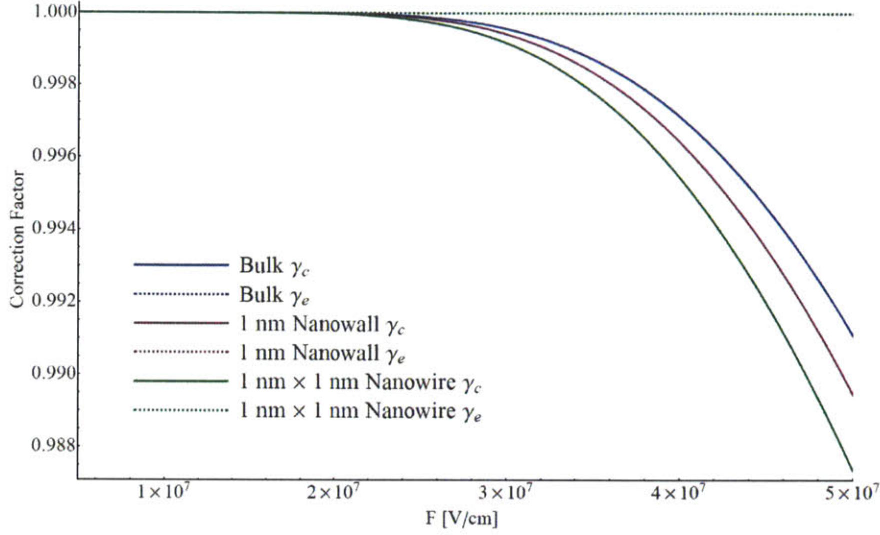

Figure 5-5: Correction factors for a bulk emitter, 1 nm NU nanowall emitter, and 1 nm × 1 nm rectangular nanowire emitter as a function of the applied field for the first subband, at $T = 300$ K, with $\phi = 5$ eV and $E_F = 5$ eV.

where G is a function of γ_n, c, and $\bar{c}$. Figure 5-5 shows the correction factors for both the circular and elliptical constant energy cross sections of the bulk, NU nanowall, and NU rectangular nanowire emitters as a function of the applied electric field. As can be seen, across all applied fields in the plot, the band structure correction factor is approximately unity. Increases in the Fermi energy and work function result in the band structure correction factors converging to unity at higher applied fields. Consequently, the band structure corrections for NU emitters with $E_F > 0$ can be ignored without introducing significant error into the total ECD and the new band structure correction factor for a single constant energy surface becomes $\lambda_B \approx 1$.

Correction factors for NC emitters with $E_F > 0$ and $E_F < 0$ play a more significant role in determining the total ECD and take the form

$$\lambda_{B,q} = 1 - \gamma_n \exp\left[-\frac{B}{\gamma_a F}\left[\left(E_F + \phi - \gamma_n W_q\right)^{3/2} - \left(E_F + \phi - W_q\right)^{3/2}\right]\right]. \qquad (5.6)$$

As Figure 5-6 shows, the correction factors for both the NC nanowall and NC rectangular nanowire can reach values as low as 0.2 at high applied fields for the higher

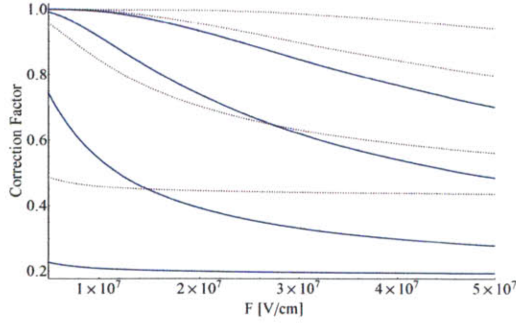

Figure 5-6: Correction factors for the 15th (top), 10th, 5th, and 1st (bottom) subbands of a 10 nm NC nanowall emitter as a function of the applied field. The solid curves are the correction factors for the circular constant energy cross sections, while the dashed curves represent the elliptical constant energy cross sections.

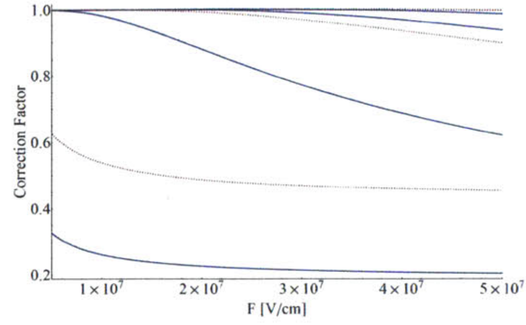

Figure 5-7: Correction factors for the 15th (top), 10th, 5th, and 1st (bottom) subbands of a 10 nm x 10 nm NC rectangular nanowire emitter as a function of the applied field. The solid curves are the correction factors for the circular constant energy cross sections, while the dashed curves represent the elliptical constant energy cross sections.

energy subbands. The correction factors also show a weak dependence on both the Fermi energy and work function of the material, with the band structure correction factors for the lower energy subbands increasing towards unity as the Fermi energy and work function increase. Band structure correction factors of this magnitude significantly reduce the emitted current density compared to the elementary ECD equations. For the NC rectangular nanowire, the correction factors are shown in Figure 5-7. Relative to the NC nanowall, these correction factors exhibit a different dependence on the field due to the incorporation of a non-unity field enhancement factor, γ_a. Again these correction factors are non-negligible and reduce the ECD in a significant manner relative to the elementary ECD from the corresponding emitter type. The same dependence on the Fermi energy and work function as was found for the NC nanowall band structure corrections also applies to the NC rectangular nanowire correction factors.

In the case of NU emitters with $E_F < 0$, the band structure correction factors

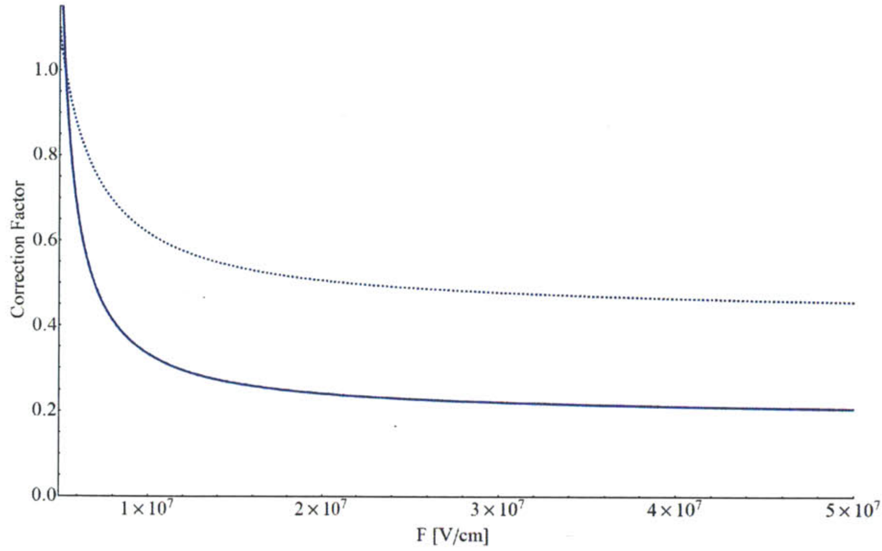

Figure 5-8: The correction factors for NU emitters with $E_F < 0$ are the same between emitter geometries. For low applied fields, the correction factors increase sharply, but converge to the ratio of the effective mass to the free electron mass for high applied fields.

take the form

$$\lambda_B = \frac{1 - \gamma_n}{1 - \gamma_n c_{R,n} k_B T} \tag{5.7}$$

and are shown in Figure 5-8. For low applied fields, the correction factors exceed unity and seemingly enhance the emitted current density. However, the current density from this enhancement is most likely not significant due to the low tunneling probabilities at such low applied fields. As the applied field increases, the correction factors approach the ratio of the effective mass to the free electron mass for the given constant energy surface. Consequently, these correction factors are non-negligible at fields relevant to field emission and have a noticeable impact on the ECD. Correction factors for NC emitters with $E_F < 0$ are functionally the same as shown in Figure 5-6 and Figure 5-7, but with slightly larger first subband correction factors due to the substitution of χ_e eV for $\phi + E_F$ in Equation 5.6.

5.4 Fowler-Nordheim Plots for Quantum-Confined Emitters

A common way of analyzing experimental field emission data is with Fowler-Nordheim plots, which plot $\ln\left[J/F^2\right]$ vs. $1/F$ or $\ln\left[I/V^2\right]$ vs. $1/V$. Since the elementary form of the Fowler-Nordheim equation is

$$J(F) = A\phi^{-1}F^2 \exp\left[-\frac{B}{\gamma_a F}\phi^{3/2}\right] \tag{5.8}$$

the slope of the FN plot can be used to determine the work function or field enhancement factor of the emitter from experimental field emission data. Different forms of FN plots, termed normally-unconfined and semiconductor FN plots are needed for parameter extraction from quantum-confined emitters and are presented in this section.

5.4.1 Parameter Extraction from Normally-Unconfined Emitters

In order to investigate the applicability of using FN plots to analyze data from quantum-confined emitters, the work function of the NU nanowall and NU rectangular nanowire emitters (with $\gamma_a = 1$) is extracted from their FN plots in Figure 5-9 and compared to the work function used in generating the ECD data. As can be seen, the slopes of the 1 nm NU nanowall and 1 nm $\times$ 1 nm NU rectangular nanowire are larger than the slopes for the 5 nm NU nanowall and 5 nm $\times$ 5 nm NU rectangular nanowire, which appear to display bulk emitter characteristics. As a result, the values of ϕ extracted from the FN plot for the smaller NU nanowall and NU rectangular nanowire in Table 5.1 do not agree with the known work function. The discrepancy between the extracted and known work function is due to: i) the

construction of the FN plot and ii) the method used in extracting the work function for quantum-confined emitters.

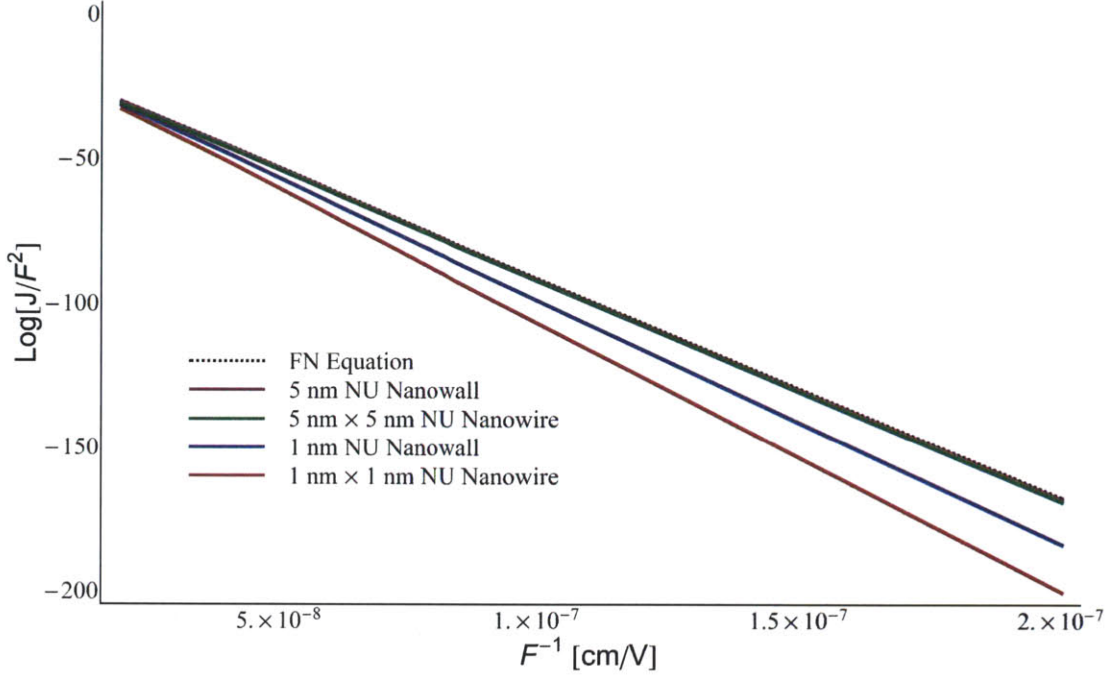

Figure 5-9: FN plots for for an elementary bulk emitter, 5 nm NU nanowall emitter, 1 nm NU nanowall emitter, 5 nm × 5 nm NU rectangular nanowire emitter, and 1 nm × 1 nm rectangular nanowire emitter for which $E_F = 10$ eV, $\phi = 5$ eV.

Traditionally, FN plots are constructed by dividing J by F^2, then taking the natural log of the result and plotting it against $1/F$, yielding a straight line. The work function or field enhancement factor of a bulk emitter can then be extracted from the slope of the FN plot by

$$\phi = \left(-\frac{\gamma_a m}{B}\right)^{2/3} \tag{5.9}$$

where m is the slope of the FN plot, B is the second FN constant, and γ_a is the field enhancement factor at the emitter tip. However, the ECD for NU emitters is not always proportional to F^2. A more general form for elementary ECD equations of

Emitter Type	FN ϕ (eV)	% Error	FN-type ϕ (eV)	% Error
Bulk	5.00	0	–	–
1 nm NU NW	5.35	6.90	5.00	0
2.5 nm NU NW	5.04	0.81	5.01	0.26
5 nm NU NW	5.01	0.23	5.03	0.58
1 nm × 1 nm NU rNW	5.69	13.8	5.00	0
2.5 nm × 2.5 nm NU rNW	5.08	1.63	5.03	0.52
5 nm × 5 nm NU rNW	5.02	0.46	5.06	1.17

Table 5.1: Work functions extracted from FN plots and FN-type plots for which $E_F = 10$ eV, $\phi = 5$ eV, and $\gamma_a = 1$.

NU emitters can be expressed as

$$J(F) = e \sum_{\alpha} A_\alpha F^p \exp\left[-\frac{B}{\gamma_a F}\left(\phi + E_{t,\alpha}\right)^{3/2}\right] \tag{5.10}$$

where A_α is a constant per subband, p is the pre-exponential field power, and $E_{t,\alpha}$ are any transverse quantum confinement energies of subband α. Due to the pre-exponential field power of NU emitters comprised of 1D and 0D electron gases in dimensions transverse to emission depending on powers of the applied electric field other than two, the slope of the FN plot is not constant. This can be corrected by generating plots analogous to FN plots, normally-unconfined Fowler-Nordheim (NUFN) plots, of the form $\ln[J/F^p]$ vs $1/F$. The slope extracted from NUFN plots can be used to determine the approximate barrier height seen by electrons at the emission reference level of the dominant emitting subband.

Having determined the slope of the NUFN plots, it is possible to extract the approximate work function. Assuming that the emitter is small enough that the ECD from a single subband constitutes the majority of the total ECD from the emitter leads to a simplification of Equation 5.10:

$$J(F) \approx eA_1 F^p \exp\left[-\frac{B}{\gamma_a F}\left(\phi + E_{t,1}\right)^{3/2}\right]. \tag{5.11}$$

By dividing J by F^p and taking the natural log of the result, the slope of the NUFN

plot becomes

$$m = -\frac{B}{\gamma_a}\left(\phi + E_{t,1}\right)^{3/2} \tag{5.12}$$

and the work function can be extracted from the slope using

$$\phi = \left(-\frac{\gamma_a m}{B}\right)^{2/3} - E_{t,1}. \tag{5.13}$$

NUFN plots were prepared for both the NU nanowall and NU rectangular nanowire emitters with $\gamma_a = 1$, the slope was measured, and the work function was extracted using Equation 5.13, as listed in the last two columns of Table 5.1. The results show a greater accuracy in extracting the work function from the 1 nm and 2.5 nm NU nanowalls and 1 nm $\times$ 1 nm and 2.5 nm $\times$ 2.5 nm NU rectangular nanowires, but lower accuracy for the work functions of the 5 nm NU nanowall and 5 nm $\times$ 5 nm NU rectangular nanowire, when compared to traditional FN analysis for bulk emitters. The decrease in accuracy for the 5 nm emitters is due to the breakdown of the assumption that only one subband contributes significantly to emission as the emitter's dimensions increase. When additional subbands are incorporated into the NUFN plot, the function plotted on the y-axis is no longer the natural log of a single exponential term, but the natural log of a sum of exponentials, resulting in no clear way to extract the work function analytically. Thus, the breakdown of the single subband assumption marks the onset of the transition region in which the emitter cannot be decisively treated as comprising a 1D or 2D or 3D electron gas. However, Table 5.1 shows that using either the FN or NUFN procedure to extract the work function of an emitter in the transition region leads to errors of similar magnitude in the extracted work function, both under 1.5%. An extended analysis on the transition region and how particular system parameters affect the location of the transition point between electron gas dimensionalities can be found in Appendix E.

After the incorporation of band structure effects and the Schottky-Nordheim bar-

rier into the model of field emission from silicon, the work function cannot be reliably extracted from FN plots. The band structure effects introduce additional exponential terms that contain the difference between the work function and effective work function for each of the constant energy surfaces, which eliminates the pure exponential character of the ECD equations. In addition, due to the introduction of a barrier shape correction factor (ν) that is dependent upon the applied field, the FN plot is no longer a straight line. The sum of these effects is a greater error in determining the work function or field enhancement factor of silicon emitters.

For emitters with $E_F < 0$, the electron affinity of the emitter is able to be extracted from semiconductor FN (SFN) plots. Due to the pre-exponential factor in the ECD equations not being a strong function of the applied field, a plot of the form $\ln[J]$ vs. $1/F$ is appropriate for data analysis. Since the transmission function is expanded about $W = 0$, there are no quantum confinement energies in the zero-field reference barrier height and the electron affinity can be extracted from

$$\chi_e = \left(-\frac{m\gamma_a}{B}\right)^{2/3} \tag{5.14}$$

which is appropriate for all non-degenerate semiconductor NU emitters, regardless of their dimensionality.

5.4.2 NC Emitters

Theoretically, the work function or field enhancement factor of NC emitters can also be extracted via the slope of logarithmic plots of experimental field emission data. Using the single subband approximation, the general form for the ECD from elementary NC emitters is

$$J(F) \simeq A_q \exp\left[-\frac{B}{\gamma_a F}\left(\phi + E_F - W_q\right)^{3/2}\right] \tag{5.15}$$

where A_q is a constant per subband q and W_q is the normal energy of the emitter for subband q. As the pre-exponential field power is zero for NC emitters, the appropriate plot needed to extract function for NC emitters is the same as for the SFN plot: $\ln[J]$ vs. $1/F$. This leads to an equation that gives a work function of

$$\phi = \left(-\frac{\gamma_a m}{B}\right)^{2/3} - E_F + W_q. \tag{5.16}$$

In practice, this does not appear to be a reliable way of extracting the work function since the extraction requires that the Fermi energy, field enhancement factor, and the normal energy of the dominant subband also be known. As a result, extracting the work function or electron affinity from NC emitters is not discussed further here.

5.5 Comparison of Framework Equations to Experimental Data

In order to test the validity of the framework, ECD equations are compared to experimental data from various field emitters. While data for arrays of emitters of various geometries and materials is readily available, validation of the framework requires data from a sufficiently small single emitter ($<\sim$ 5 nm). Data from a single, quantum-confined emitter is preferred because the ECD equation can be directly compared to both the plot of J vs. F. Two systems that fit these requirements are those of a vertical single-layer graphene emitter and single carbon nanotube emitter.

5.5.1 Vertical Single-Layer Graphene

Tsai et al. fabricated and measured the field emission characteristics of a single, vertically-oriented piece of single-layer graphene [84]. Treating graphene as a metal allows for the use of the following equation from the framework in predicting the

ECD:

$$I^{u}_{wall}\left(F\right) = eA_{emis}\frac{2}{hL_x}\sqrt{2m_0\pi}\sum_{\alpha_x}\left(\frac{2\gamma_a F}{3Bt\sqrt{\phi + E_{\alpha_x}}}\right)^{3/2}\exp\left[-\frac{B}{\gamma_a F}\nu\left(\phi + E_{\alpha_x}\right)^{3/2}\right] \tag{5.17}$$

where γ_a is the field enhancement factor of the floating cylinder given by Equation C-2, the work function of graphene is approximately 5.0 eV [85], and the approximate emission area was extracted to be $A_{emis} = 6.12 \times 10^{-16} cm^2$. Since the thickness of graphene layers is approximately 0.335 nm [86], the emitter width is taken to be $L_x = 0.335$ nm.

Using these parameters, the ECD from Equation 5.17 was plotted against the experimental data in Figure 5-10. Since no emitter height was given with the data, emitter heights were adjusted in the ECD equations to find a field enhancement factor that gave the best visual fit to the data for each sweep, resulting in an emitter heights of 8.5 μm, 10.5 μm, and 14μm for the first, second, and third sweeps respectively. For comparison, the ECD predicted from bulk emitters of equivalent geometry are also shown as the dashed curves.

In agreement with the results in §5.2.1, the difference between the bulk ECD equations and NU nanowall ECD equations is significant for an emitter of such a small size. In addition, for an emitter of this size, the effects of quantum confinement of the electron supply are of approximately the same order of magnitude as the effect of field enhancement at the emitter tip. Since the typical size of graphene flakes prepared using the method from [84] are on the order of several micrometers, the emitter heights predicted by fitting the ECD equations to the experimental data seem reasonable. However, the comparison of the NU nanowall ECD equation to the current emitted from a single-layer graphene edge is a rough approximation at best. Xiao et al. have performed a more extensive analysis of emission from the edge of a single-layer graphene emitter that is specific to graphene emitters [87].

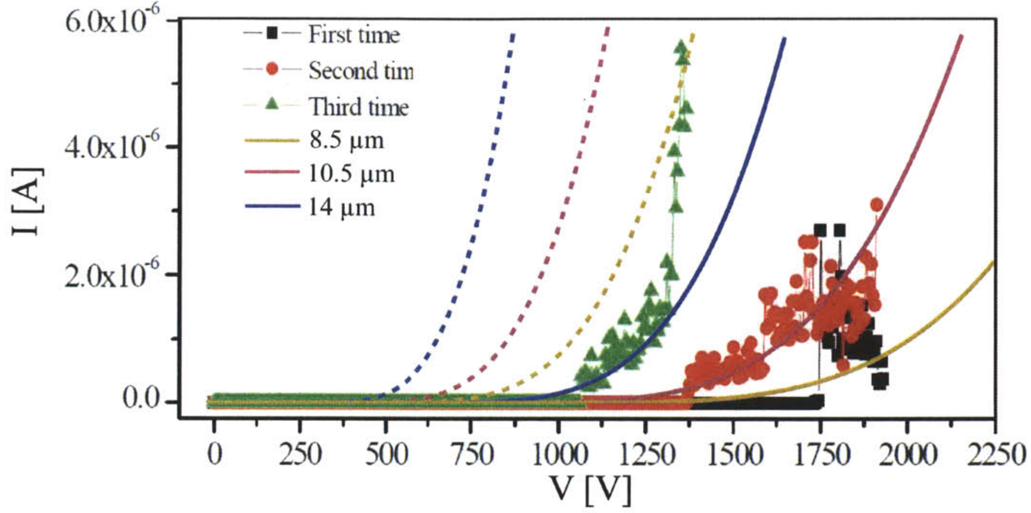

Figure 5-10: Experimental field emission data from a vertically-oriented single-layer graphene sheet for three different voltage sweeps, overlaid by the ECD predicted by Equation 5.17 for emitters with heights of 8.5 μm, 10.5 μm, and 14 μm. Dashed curves represent the ECD predicted for a bulk emitter of equivalent geometry.

5.5.2 Single-Walled Carbon Nanotube

The framework was also compared with data from single, single-walled carbon nanotubes (SWNT) via the equation for the elementary NU cylindrical nanowire emitter with the Schottky-Nordheim barrier:

$$I^{u}_{cwire,\alpha_{m,n}}(F) = eA_{emis}\frac{2}{h\pi a^2}\sum_{m,n}\left(\frac{2\gamma_a F}{3Bt\sqrt{\phi + E_{\alpha_{m,n}}}}\right) \times \exp\left[-\frac{B}{\gamma_a F}\nu\left(\phi + E_{\alpha_{m,n}}\right)^{3/2}\right] \tag{5.18}$$

where γ_a is given by the floating sphere at emitter plane potential model in Equation C-2, $\phi = 5$ eV, and $A_{emis} = \pi a^2$. Equation 5.18 was compared to experimental field emission data from multiple SWNT emitters with varying lengths, radii, and anode spacings, as shown in Figure 5-11 [88]. On each of the plots, the NU cylindrical nanowire equation for the appropriate system parameters was plotted alongside the equivalent bulk emitter equation.

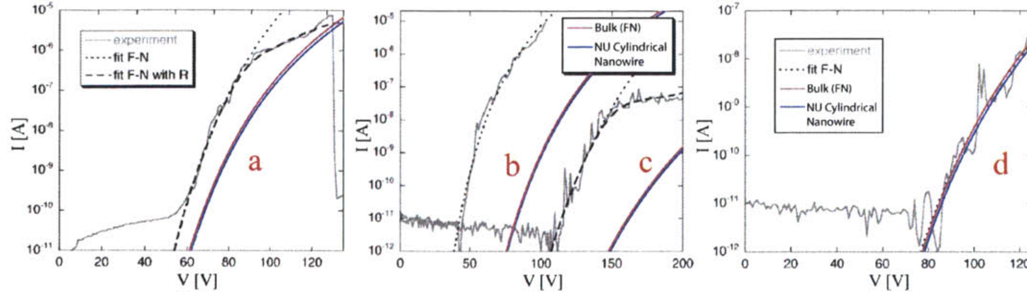

Figure 5-11: Field emission data from four sets of experimental setups, where a is the SWNT radius, l is the SWNT length, and d is the SWNT-anode spacing: (a) $a = 5$ nm, $l = 0.66$ μm, $d = 2$ μm, (b) $a = 7$ nm, $l = 1.32$ μm, $d = 2$ μm, (c) $a = 7$ nm, $l = 2.35$ μm, $d = 3.75$ μm, and (d) $a = 5$ nm, $l = 4.56$ μm, $d = 5.8$ μm. Both the NU cylindrical nanowire equation and bulk emitter equation are plotted for each data set.

The NU cylindrical nanowire equation seems to universally underestimate the current emitted from the SWNT, but due to a lower field enhancement factor than extracted from the data and not from quantum confinement of the electron supply. Overall, the plots show that for emitters of these sizes ($a = 5, 7$ nm) field enhancement at the emitter tip exerts significantly more influence over the total emitted current than quantum confinement of the electron supply, as evidenced by the similarity between the calculated emission curves for the NU cylindrical nanowire and bulk emitter. As a result, the majority of the error between the framework and the experimental data comes from the model used for calculating the field enhancement at the tip of the emitter and the adjustment to the ECD from quantum confinement is minimal, yet still quantifiable.

5.6 Chapter Summary

In this chapter, the effects of quantum confinement on the ECD, relative to the ECD predicted by the elementary FN equation were investigated. While transverse quantum confinement of an emitter decreases the emitted current density, normal quantum confinement leads to an oscillatory ECD that may exceed the ECD predicted

by the FN equation for small normal well widths. The incorporation of electric field enhancement at the emitter tip into the model reveals that at some critical emitter width(s), the effects of an increasingly quantum-confined electron supply overcome the barrier thinning introduced by field enhancement and the ECD reaches a maximum value before decreasing toward zero at very small well widths.

The effects of finite temperature, the Schottky-Nordheim barrier, and the band structure of silicon on the ECD were also discussed. Emitters at a finite temperature emit a slightly higher amount of current than their $T = 0$ K counterparts, but in most cases this additional contribution is negligible. The Schottky-Nordheim barrier increases the absolute ECD of all types of emitters relative to emitters modeled by the exact triangular barrier, but as the amount of quantum-confinement of the electron supply increases, the additional ECD from the rounded barrier is reduced due to the majority of the ECD coming from energy levels far below the top of the barrier. Band structure effects per constant energy surface of silicon serve to reduce the ECD relative to the free electron constant energy surfaces used in traditional field emission theory. While able to be ignored for degenerate silicon emitters, band structure effects significantly reduce the ECD from non-degenerate, n-type silicon emitters.

When analyzing field emission data from quantum-confined emitters via FN plots, it was found that the FN equation is appropriate for use with emitters that have multiple subbands contributing significantly to the total ECD. For NU metal and degenerate semiconductor emitters with a single dominant subband, a normally-unconfined FN plot should be used, which divides by a different pre-exponential power of the field depending on the dimensionality of the electron supply. In order to extract the work function or field enhancement factor from NUFN plots, it is also necessary to take into account the transverse confinement energy of the dominant subband. For NU non-degenerate semiconductor emitters and all types of NC emitters, there is no factor of F in the pre-exponential factor and a plot of J vs. $1/F$ should be used.

When compared with experimental data for vertical single-layer graphene and single-walled carbon nanotubes, the framework demonstrated that except in cases where emitters are extremely small ($<\sim$ 1 nm), the difference between the bulk emitter equation ECD and the NU emitter ECD equation were negligible compared to the difference in the ECD for varying field enhancement factors. As a result, unless emitters are sufficiently small, quantum-confinement of the emitter's electron supply does not appear to be a significant when determining the total ECD from nanoscale emitters.

Chapter 6

Thesis Summary and Future Work

6.1 Summary

At the outset of this work, the ultimate goal was to investigate the effects of quantum confinement of a field electron emitter's electron supply on the emitted current density via analytical emitted current density equations. While providing clear qualitative results, the elementary framework for cold field emission, its extension to silicon emitters, and the associated analysis developed in this thesis are just a small step into a largely unexplored region of the theory of field emission.

The elementary framework provides physically-simplified emitted current density equations that are meant to predict the ECD from emitters with quantum-confined electron supplies more accurately than the elementary Fowler-Nordheim equation. Notable differences from the elementary FN equation for transversally-quantum-confined NU emitter ECD equations include a weaker dependence on the applied field in the pre-exponential factor and the addition of transverse quantum confinement energy terms to the emitter work function in the exponential portion, resulting in a comparatively larger tunneling barrier height for electrons. The lack of integration over normal energies for NC emitter ECD equations results in no dependence

on the applied field in the pre-exponential term, a strong dependence on the normal energy of the electron subband, and no concept of a reference zero-field barrier height.

In order to extend the model to silicon emitters in Chapter 4, a more physically-complete set of ECD equations was derived by incorporating various correction factors to account for finite temperature, the Schottky-Nordheim barrier potential, and the non-spherical constant energy surfaces of silicon. Across all cases, the incorporation of the SN barrier potential and band structure effects increase the ECD predicted from silicon emitters relative to the elementary model, as electrons see a lower barrier height and silicon has six conduction valleys from which electronic states contribute to emission. For emission from the conduction band of materials with $E_F > 0$, the band structure corrections for silicon emitters were negligible aside from the multiplication factor of six to account for electronic states in all conduction valleys. Emission from the conduction band of materials with $E_F < 0$ was significantly affected by band structure corrections and the emitted current density from each constant energy surface was reduced by a factor equal to approximately the ratio of the effective mass of electrons transverse to the emission direction to the free electron mass.

Using equations generated by the elementary framework, the effects of normal and transverse quantum confinement of the electron supply on the ECD were investigated in the absence of geometry-dependent field enhancement in Chapter 5. In NU emitters, transverse quantum confinement of the electron supply causes a decrease in the ECD with decreasing transverse dimensions due to fewer electrons in the emitter and an increased tunneling barrier height seen by electrons. As a function of the normal well width, the emitted current density of NC emitters oscillates due to the cyclic process of dominant emitting electron subbands leaving or entering the quantum well and can exceed that predicted by a bulk emitter because of high tunneling attempt frequencies for electrons confined to very small normal well widths. Incorporating the field enhancement factor into the elementary ECD equations demonstrated that

the ECD increases as transverse emitter dimensions decrease due to the increasing, geometry-dependent local electric field until a critical emitter width or radius d_{peak}. Below d_{peak}, the supply of electrons to the barrier becomes the limiting factor and the ECD decreases with decreasing transverse emitter dimensions. However, as the calculations using material parameters for tungsten show, transverse quantum confinement effects only dominate over electrostatic field enhancement for an emitter diameter below approximately 1 nm. Plots of the NU silicon ECD equations versus emitter dimensions yielded qualitatively similar results to the elementary ECD equations. However, for emitters with $E_F < 0$, the absolute ECD was reduced relative to emitters with $E_F > 0$ as a result of the decreased electron supply. For NC emitters with $E_F < 0$, the oscillatory behavior seen in the elementary ECD equations disappeared as a result of all emitting subbands contributing more evenly to the total ECD when the ERL (conduction band edge) was located at least $3k_BT$ above E_F.

With respect to parameter extraction from FN plots, it was found that using the bulk theory to describe emission from quantum-confined emitters led to noticeable errors in results. An alternative set of plotting and parameter extraction procedures specifically designed for emitters with quantum-confined electron supplies was proposed and an analysis was carried out that demonstrated that when a single subband dominated the total ECD, the proposed procedures were more accurate than traditional FN theory. When multiple subbands contribute significantly to emission, these proposed plotting procedures are less accurate for parameter extraction and seem to work approximately as well as using FN plots.

6.2 Model Limitations

Providing a simple set of equations for the ECD from emitters with quantum-confined electron supplies has naturally introduced many trade-offs with respect to the physical

validity of the model. As this thesis has focused on issues exclusively related to quantum confinement of the electron supply, only model limitations directly relevant to electronic structure will be addressed in this section. However, it should be noted that there are many other areas of field emission theory and modeling that have opportunities to make significant progress in closing the gap with experimental results, such as the theory dictating FN plot interpretation, theory of electron tunneling, behavior of non-metallic field emitters, and emitter tip electrostatics [89].

The largest assumption made in the model is that the emitters are comprised of an ideal electron gas with plane-wave wave functions for electrons. The validity of this assumption for electrons in unconfined dimensions of metallic emitters seems to be acceptable, as it has been successful at describing experimental phenomena related to the electrical and thermal properties of metals and is employed in texts on solid state physics [90, 91]. On the other hand, the applicability of this model to semiconductor emitters is unclear, due to the expected importance of the details of band structure, crystal orientation, and defects/impurities for emission calculations. More rigorous solutions for the electronic wave functions, energies, and band structures may be obtained via including the several potential terms typically found in crystalline solids into a field emission model [92].

Another consideration that has been overlooked is detailed modeling of the field penetration and electronic states in semiconductors near or on the emitting surface. Penetration of the applied field into the semiconductor near the emitting surface leads to the formation of an accumulation layer of electrons which may contribute significantly to the total emitted current density. More detailed models for band bending exist [54, 64] and the analytical approach from Appendix D should be compared to such models to test its validity. Similarly, the electronic structure close to and on the emitting surface is known to be different from that of the emitter bulk [92], likely leading to different emission physics than what was presented in this work. Especially for

the NC emitter case, treating the electrons semi-classically as particles bouncing between the walls of such a small, normally-confined well seems inappropriate with two surfaces in close proximity. It is expected that these issues should be addressed with more detailed quantum-mechanical models of electronic wave functions and energies that may incorporate atomic structure, but it is unclear if these additional physical considerations have a significant enough effect for inclusion in engineering models of field emission. The result would be a more physically accurate description of field emission, but the degree to which analytical solutions can be provided is unknown at the current time.

6.3 Future Work

Future work on the effects of the quantum confinement of the electron supply on field emission is informed both by the shortcomings of the model discussed above as well as additional models and theory that are needed by the field. A more physically valid description of emission from semiconductors, including modeling additional quantum-mechanical effects of electrons in nanoscale crystalline solids and emission from the surfaces of very thin emitters, is needed for better agreement between emission theory and experiment. Similarly, the details of the electron supply to and in the emitter tip are poorly understood. Calculating the energy level distribution of electrons in different tip geometries could lead to determinations of whether or not quantum confinement effects are important to consider in such situations. Finally, it would be useful to have procedures for determining the point at which a nanoscale emitter should be considered quantum-confined and under what conditions the emitter can be approximated as a bulk emitter. Ideally, analytical solutions to these problems would be found and incorporated into relatively simple equations for immediate use by field electron emission experimentalists.

Bibliography

[1] J. W. Gadzuk and E. W. Plummer. Field emission energy distribution (feed). *Rev. Mod. Phys.*, 45:487–548, Jul 1973.

[2] F. Rana, S. Tiwari, and DA Buchanan. Self-consistent modeling of accumulation layers and tunneling currents through very thin oxides. *Applied physics letters*, 69(8):1104–1106, 1996.

[3] RE Burgess, H Kroemer, and JM Houston. Corrected values of fowler-nordheim field emission functions v (y) and s (y). *Physical Review*, 90:515–515, 1953.

[4] J. A. del Alamo. *Integrated Microelectronic Devices: Physics and Modeling*. Prentice Hall, 2012.

[5] R.F. Pierret and G.W. Neudeck. *Advanced semiconductor fundamentals*, volume 6. Pearson Education, Upper Saddle River, NJ, second edition, 2003.

[6] T.G. Phillips and J. Keene. Submillimeter astronomy [heterodyne spectroscopy]. *Proceedings of the IEEE*, 80(11):1662 –1678, nov 1992.

[7] P.H. Siegel. Terahertz technology in biology and medicine. *Microwave Theory and Techniques, IEEE Transactions on*, 52(10):2438 – 2447, oct. 2004.

[8] T.W. Crowe. Opening the terahertz window. In *Compound Semiconductor Integrated Circuit Symposium, 2004. IEEE*, pages 21 – 24, oct. 2004.

[9] J. R. Wang, P. Racette, J. D. Spinhirne, K. F. Evans, and W. D. Hart. *Geophysical Research Letters*, 25(8):1145–1148, 1998.

[10] J.C. Dickinson, T.M. Goyette, A.J. Gatesman, C.S. Joseph, Z.G. Root, R.H. Giles, J. Waldman, and W.E. Nixon. Terahertz imaging of subjects with concealed weapons. Technical report, DTIC Document, 2006.

[11] K. Kawase, Y. Ogawa, Y. Watanabe, and H. Inoue. Non-destructive terahertz imaging of illicit drugs using spectral fingerprints. *Opt. Express*, 11(20):2549–2554, 2003.

[12] D. Woolard, R. Kaul, R. Suenram, A.H. Walker, T. Globus, and A. gSamuels. Terahertz electronics for chemical and biological warfare agent detection. In *Microwave Symposium Digest, 1999 IEEE MTT-S International*, volume 3, pages 925–928. IEEE, 1999.

[13] T.H. Lee. Candidate thz sources: the history and future (?) of velocity-modulated devices. In *Proceedings of SPIE*, volume 6120, page 61200E, 2006.

[14] B.S. Williams. Terahertz quantum-cascade lasers. *Nature photonics*, 1(9):517–525, 2007.

[15] G.N. Fursey. Field emission in vacuum micro-electronics. *Applied surface science*, 215(1):113–134, 2003.

[16] P.A. George, C. Manolatou, F. Rana, and A.I. Akinwande. Integrated microcavity klystrons for generating high power coherent thz radiation. In *Conference on Lasers and Electro-Optics*. Optical Society of America, 2005.

[17] J.W. Han, J. Sub Oh, and M. Meyyappan. Vacuum nanoelectronics: Back to the future?gate insulated nanoscale vacuum channel transistor. *Applied Physics Letters*, 100(21):213505–213505, 2012.

[18] H. Mimura, Y. Neo, H. Shimawaki, T. Matsumoto, and K. Yokoo. Emission characteristics and application of semiconductor field emitters. *Applied surface science*, 244(1):498–503, 2005.

[19] W.A. Deheer, A. Chatelain, and D. Ugarte. A carbon nanotube field-emission electron source. *Science*, 270(5239):1179–1180, 1995.

[20] T. Zhai, L. Li, Y. Ma, M. Liao, X. Wang, X. Fang, J. Yao, Y. Bando, and D. Golberg. One-dimensional inorganic nanostructures: synthesis, field-emission and photodetection. *Chemical Society Reviews*, 40(5):2986–3004, 2011.

[21] A. Malesevic, R. Kemps, A. Vanhulsel, M.P. Chowdhury, A. Volodin, and C. Van Haesendonck. Field emission from vertically aligned few-layer graphene. *Journal of applied physics*, 104(8):084301–084301, 2008.

[22] RN Hall. The application of non-integral legendre functions to potential problems. *Journal of Applied Physics*, 20(10):925–931, 1949.

[23] JA Becker. The use of the field emission electron microscope in adsorption studies of w on w and ba on w. *Bell System Technical Journal*, 30:907, 1951.

[24] WP Dyke, JK Trolan, WW Dolan, and G. Barnes. The field emitter: fabrication, electron microscopy, and electric field calculations. *Journal of Applied Physics*, 24(5):570–576, 1953.

[25] H.G. Kosmahl. A wide-bandwidth high-gain small-size distributed amplifier with field-emission triodes (fetrodes) for the 10 to 300 ghz frequency range. *Electron Devices, IEEE Transactions on*, 36(11):2728–2737, 1989.

[26] PH Cutler, J. He, J. Miller, NM Miskovsky, B. Weiss, and TE Sullivan. Theory of electron emission in high fields from atomically sharp emitters: validity of the fowler-nordheim equation. *Progress in surface science*, 42(1):169–185, 1993.

[27] GNA Van Veen. Space-charge effects in spindt-type field emission cathodes. *Journal of Vacuum Science & Technology B: Microelectronics and Nanometer Structures*, 12(2):655–661, 1994.

[28] KL Jensen, EG Zaidman, MA Kodis, B. Goplen, and DN Smithe. Analytical and seminumerical models for gated field emitter arrays. i. theory. *Journal of Vacuum Science & Technology B: Microelectronics and Nanometer Structures*, 14(3):1942–1946, 1996.

[29] L. Dvorson, M. Ding, and A.I. Akinwande. Analytical electrostatic model of silicon conical field emitters. i. *Electron Devices, IEEE Transactions on*, 48(1):134–143, 2001.

[30] L. Dvorson, M. Ding, and A.I. Akinwande. Analytical electrostatic model of silicon conical field emitters. ii. extension to devices with focusing electrode. *Electron Devices, IEEE Transactions on*, 48(1):144–148, 2001.

[31] Richard G Forbes, CJ Edgcombe, and U Valdre. Some comments on models for field enhancement. *Ultramicroscopy*, 95:57–65, 2003.

[32] Takao Utsumi. Vacuum microelectronics: what's new and exciting. *Electron Devices, IEEE Transactions on*, 38(10):2276–2283, 1991.

[33] RV Latam. High voltage vacuum insulation: the physical basis, 1981.

[34] Rod V Latham. *High voltage vacuum insulation: basic concepts and technological practice.* Academic Press, 1995.

[35] CJ Edgcombe and U Valdre. The enhancement factor and the characterization of amorphous carbon field emitters. *Solid-State Electronics*, 45(6):857–863, 2001.

[36] CJ Edgcombe and U Valdre. Microscopy and computational modelling to elucidate the enhancement factor for field electron emitters. *Journal of Microscopy*, 203(2):188–194, 2001.

[37] Dan Nicolaescu. Physical basis for applying the fowler–nordheim j–e relationship to experimental i–v data. *Journal of Vacuum Science & Technology B: Microelectronics and Nanometer Structures*, 11(2):392–395, 1993.

[38] NS Xu and RV Latham. The physical origin of pre-electron breakdown pinholes. *High Voltage Vacuum Insulation: Basic Concepts and Technological Practice, Academic Press, London*, 1995.

[39] Michael Kenneth Miller. Atom probe field ion microscopy. Technical report, Oak Ridge National Lab., TN (USA), 1986.

[40] R.H. Fowler and LW Nordheim. Electron emission in intense electric fields. *Proceedings of the Royal Society of London. Series A*, 119(781):173–181, 1928.

[41] X.Z. Qin, W.L. Wang, N.S. Xu, Z.B. Li, and R.G. Forbes. Analytical treatment of cold field electron emission from a nanowall emitter, including quantum confinement effects. *Proceedings of the Royal Society A: Mathematical, Physical and Engineering Science*, 467(2128):1029–1051, 2011.

[42] A. Sommerfeld. Zur elektronentheorie der metalle. *Naturwissenschaften*, 15:825–832, 1927. 10.1007/BF01505083.

[43] Harold Jeffreys. On certain approximate solutions of lineaer differential equations of the second order. *Proceedings of the London Mathematical Society*, s2-23(1):428–436, 1925.

[44] G. Wentzel. Eine verallgemeinerung der quantenbedingungen für die zwecke der wellenmechanik. *Zeitschrift für Physik A Hadrons and Nuclei*, 38(6):518–529, 1926.

[45] H.A. Kramers. Wellenmechanik und halbzahlige quantisierung. *Zeitschrift für Physik A Hadrons and Nuclei*, 39(10):828–840, 1926.

[46] L. Brillouin. La mcanique ondulatoire de schrdinger: une mthode gnrale de resolution par approximations successives. *Comptes Rendus de l'Academie des Science*, 183:24–26, 1926.

[47] E.L. Murphy and RH Good Jr. Thermionic emission, field emission, and the transition region. *Physical review*, 102(6):1464, 1956.

[48] W. Schottky. Influence of structure-action especially the thomson constructive force, on the electron emission of metals. *Phys. Z.*, 15:872, 1914.

[49] L.W. Nordheim. The effect of the image force on the emission and reflexion of electrons by metals. *Proceedings of the Royal Society of London. Series A*, 121(788):626–639, 1928.

[50] Richard G Forbes. Simple good approximations for the special elliptic functions in standard fowler-nordheim tunneling theory for a schottky-nordheim barrier. *Applied physics letters*, 89(11):113122–113122, 2006.

[51] R.G. Forbes. Comments on discrepancies in the fowler and nordheim 1928 paper. In *Vacuum Nanoelectronics Conference (IVNC), 2011 24th International*, pages 113–114. IEEE, 2011.

[52] Beverly A Politzer and PH Cutler. Theory of electron tunneling from d bands in solids i. application to field emission. *Materials Research Bulletin*, 5(8):703–720, 1970.

[53] Beverly A Politzer and PH Cutler. Band-structure calculation of the electron spin polarization in field emission from ferromagnetic nickel. *Physical Review Letters*, 28(20):1330–1333, 1972.

[54] R. Stratton. Theory of field emission from semiconductors. *Physical Review*, 125(1):67, 1962.

[55] Douglas Nagy and PH Cutler. Calculation of band-structure effects in field-emission tunneling from tungsten. *Physical Review*, 186(3):651, 1969.

[56] Jeans JH. *The Mathematical Theory of Electricity and Magnetism.* 4th edition.

[57] F Rohrbach. Cern report 71-5. *TC-L*, 1971.

[58] N. Fröman and P.O. Fröman. *JWKB approximation: contributions to the theory.* North-Holland Amsterdam, 1965.

[59] R.G. Forbes. On the need for a tunneling pre-factor in fowler nordheim tunneling theory. *Journal of Applied Physics*, 103(11):114911–114911, 2008.

[60] LD Landau and EM Lifshitz. Quantum mechanics, vol. 3. *Course of theoretical physics*, page 183, 1965.

[61] R Stratton. Field emission from semiconductors. *Proceedings of the Physical Society. Section B*, 68(10):746, 1955.

[62] Robert Stratton. Energy distributions of field emitted electrons. *Phys. Rev*, 135(3), 1964.

[63] Robert Gomer. *Field emission and field ionization*, volume 34. Harvard University Press Cambridge, MA, 1961.

[64] TT Tsong. Field penetration and band bending near semiconductor surfaces in high electric fields. *Surface Science*, 81(1):28 42, 1979.

[65] SA Guerrera. Feature scaling of large, ballasted, field emission arrays. Master's thesis, Massachusetts Institute of Technology.

[66] R.G. Forbes and Z.B. Li. Emission reference level: A missing concept in emission theory. In *Vacuum Nanoelectronics Conference (IVNC), 2011 24th International*, pages 121–122. IEEE, 2011.

[67] Richard G Forbes. Thin-slab model for field electron emission. *Journal of Vacuum Science & Technology B: Microelectronics and Nanometer Structures*, 28(2):C2A43–C2A49, 2010.

[68] RW Gurney and EU Condon. Quantum mechanics and radioactive disintegration. *Physical Review*, 33(2):127, 1929.

[69] David Jeffery Griffiths. *Introduction To Quantum Mechanics, 2/E.* Pearson Prentice Hall, 2004.

[70] F W Robinett. Visualizing the solutions for the circular infinite well in quantum and classical mechanics. *Am. J. Phys*, 64(4):4, 1996.

[71] L.D. Landau, EM Lifshitz, JB Sykes, JS Bell, and ME Rose. Quantum mechanics, non-relativistic theory: Vol. 3 of course of theoretical physics. *Physics Today*, 11:56, 1958.

[72] Richard G. Forbes. Physics of generalized fowler-nordheim-type equations. volume 26, pages 788–793. AVS, 2008.

[73] N. D. Lang and W. Kohn. Theory of metal surfaces: Induced surface charge and image potential. *Phys. Rev. B*, 7:3541–3550, Apr 1973.

[74] RN Thomas, RA Wickstrom, DK Schroder, and HC Nathanson. Fabrication and some applications of large-area silicon field emission arrays. *Solid-State Electronics*, 17(2):155–IN7, 1974.

[75] HF Gray, GJ Campisi, and RF Greene. A vacuum field effect transistor using silicon field emitter arrays. In *Electron Devices Meeting, 1986 International*, volume 32, pages 776–779. IEEE, 1986.

[76] RB Marcus, TS Ravi, T Gmitter, HH Busta, JT Niccum, KK Chin, and D Liu. Atomically sharp silicon and metal field emitters. *Electron Devices, IEEE Transactions on*, 38(10):2289–2293, 1991.

[77] D Temple, CA Ball, WD Palmer, LN Yadon, D Vellenga, J Mancusi, GE McGuire, and HF Gray. Fabrication of column-based silicon field emitter arrays for enhanced performance and yield. *Journal of Vacuum Science & Technology B: Microelectronics and Nanometer Structures*, 13(1):150–157, 1995.

[78] Gen Hashiguchi and Hidenori Mimura. New fabrication method and electrical characteristics of conical silicon field emitters. *Japanese journal of applied physics*, 34(part 1):1493–1497, 1995.

[79] D Temple, WD Palmer, LN Yadon, JE Mancusi, D Vellenga, and GE McGuire. Silicon field emitter cathodes: Fabrication, performance, and applications. *Journal of Vacuum Science & Technology A: Vacuum, Surfaces, and Films*, 16(3):1980–1990, 1998.

[80] Meng Ding, Han Kim, and Akintunde I Akinwande. Observation of valence band electron emission from n-type silicon field emitter arrays. *Applied physics letters*, 75(6):823–825, 1999.

[81] IW Rangelow and St Biehl. Fabrication and electrical characterization of high aspect ratio silicon field emitter arrays. *Journal of Vacuum Science & Technology B: Microelectronics and Nanometer Structures*, 19(3):916–919, 2001.

[82] L Dvorson, I Kymissis, and AI Akinwande. Double-gated silicon field emitters. *Journal of Vacuum Science & Technology B: Microelectronics and Nanometer Structures*, 21(1):486–494, 2003.

[83] CA Spindt, CE Holland, A Rosengreen, and Ivor Brodie. Field-emitter arrays for vacuum microelectronics. *Electron Devices, IEEE Transactions on*, 38(10):2355–2363, 1991.

[84] Jeff TH Tsai, Timothy YE Chu, Jia-Yuan Shiu, and Chu-Shou Yang. Field emission from an individual freestanding graphene edge. *Small*, 8(24):3739–3745, 2012.

[85] Seung Min Song, Jong Kyung Park, One Jae Sul, and Byung Jin Cho. Determination of work function of graphene under a metal electrode and its role in contact resistance. *Nano letters*, 12(8):3887–3892, 2012.

[86] ZH Ni, HM Wang, J Kasim, HM Fan, T Yu, YH Wu, YP Feng, and ZX Shen. Graphene thickness determination using reflection and contrast spectroscopy. *Nano Letters*, 7(9):2758–2763, 2007.

[87] Zhiming Xiao, Juncong She, Shaozhi Deng, Zikang Tang, Zhibing Li, Jianming Lu, and Ningsheng Xu. Field electron emission characteristics and physical mechanism of individual single-layer graphene. *ACS nano*, 4(11):6332–6336, 2010.

[88] Jean-Marc Bonard, Christian Klinke, Kenneth A Dean, and Bernard F Coll. Degradation and failure of carbon nanotube field emitters. *Physical Review B*, 67(11):115406, 2003.

[89] Richard G. Forbes. Tutorial on the theory of field electron emission. 2013.

[90] Neil W Ashcroft and N David Mermin. Solid state physics (holt. *Rinehart and Winston, New York*, 19761, 1976.

[91] Terry P. Orlando, Rajeev J. Ram, and Stephen D. Senturia. Physics for solid state applications. 2008.

[92] A. Modinos. Field, thermionic, and secondary electron emission spectroscopy. 1984.

[93] X. Aymerich-Humet, F. Serra-Mestres, and J. Millan. A generalized approximation of the fermi–dirac integrals. *Journal of Applied Physics*, 54(5):2850–2851, 1983.

[94] John F Cochran and Bretislav Heinrich. Applications of maxwells equations. *Simon Fraser University*, 144, 2004.

[95] Peter L. Hagelstein, Stephen D. Senturia, and Terry P. Orlando. *Introductory Applied Quantum and Statistical Mechanics.* John Wiley & Sons, Inc., Hoboken, NJ, 2004.

[96] Peter L. Hagelstein. Introduction to numerical modeling in engineering and applied physics. 2011.

Appendix A

Poisson-Boltzmann Formulation of Band Bending

In order to investigate the electrostatics near the surface of the semiconductor, the Poisson equation must be solved. Taking the semiconductor-vacuum interface to be an infinite plane in the x and y dimensions located at $z = 0$, the one-dimensional Poisson equation is

$$\frac{d^2\phi(z)}{dz^2} = \frac{\rho}{\epsilon_s} \tag{A.1}$$

where ϕ is the potential in the semiconductor as a function of z, ρ is the charge density, and ϵ_s is the dielectric constant of the semiconductor. Assuming an n-type semiconductor in which all of the donor dopants are ionized, the charge density can be written as

$$\rho = e\left(n - p + N_D\right) \tag{A.2}$$

with e being the elementary charge, n the electron density, p the hole density, and N_D the density of ionized donor dopants. Invoking Maxwell-Boltzmann statistics for electrons, the carrier concentrations can be expressed in terms of the potential in the

semiconductor

$$n = n_{0B} \exp\left[\frac{e\phi}{k_B T}\right] p = p_{0B} \exp\left[-\frac{e\phi}{k_B T}\right] \tag{A.3}$$

n_{0B} and p_{0B} are the equilibrium concentrations of electrons and holes in the bulk of the semiconductor ($z \to \infty$), for which $\phi = 0$. In the bulk, charge neutrality must hold and $N_D = p_{0B} - n_{0B}$. In addition, it is a fair assumption that $n \simeq N_D$ in the bulk, making $p \simeq n_i^2/N_D$. Substituting the above definitions into Equation A.1 leads to

$$\frac{d^2\phi(z)}{dz^2} = -\frac{eN_D}{\epsilon_s}\left[\frac{n_i^2}{N_D^2}\left(\exp\left[-\frac{e\phi}{k_B T}\right] - 1\right) - \left(\exp\left[\frac{e\phi}{k_B T}\right] - 1\right)\right] \tag{A.4}$$

Multiplying both sides of the equation by $2\left(d\phi/dz\right)$ and integrating from $z = \infty$ to $z = 0$ on the left side and from $\phi = 0$ to $\phi = \phi$ on the right side yields

$$\frac{d\phi}{dz} = -\sqrt{\frac{2k_B T}{\epsilon_s}}\left[\frac{n_i^2}{N_D^2}\left(\exp\left[-\frac{e\phi}{k_B T}\right] + \frac{e\phi}{k_B T} - 1\right) + \left(\exp\left[\frac{e\phi}{k_B T}\right] - \frac{e\phi}{k_B T} - 1\right)\right]^{1/2} \tag{A.5}$$

In accumulation for an n-type semiconductor, ϕ is positive and the above equation can be simplified if $\phi \gg k_B T/e$.

$$\frac{d\phi}{dz} = -F(z) = -\sqrt{\frac{2k_B T}{\epsilon_s}} \exp\left[\frac{e\phi}{2k_B T}\right] \tag{A.6}$$

Integrating $d\phi/dz$ and imposing the boundary conditions $\phi(0) = \phi_s$ and $F(0) = F_s$, where F is the electric field in the semiconductor, gives the potential in the semiconductor as a function of z:

$$\phi(z) = -\frac{2k_B T}{e}\ln\left[\frac{z}{\sqrt{2}L_D} + \frac{1}{F\sqrt{\frac{\epsilon_s}{2N_D k_B T}}}\right] \tag{A.7}$$

In terms of the applied electric field, F_{vac}, the equations take the forms listed in Equation 2.51.

Appendix B

Elementary Emitted Current Density Equations

B.1 Normally-Unconfined Emitted Current Density Equations

B.1.1 NU Nanowire

As a result of electrons in states higher than $W = W_R$ and lower than $W = 0$ contributing relatively little to the emitted current density in the limit of $T \to 0$ K, the limits of integration can be extended to $-\infty$ and ∞. The integral takes the following form:

$$J^u_{wire,\alpha}(F) = e\frac{2}{hA_e}\int_{-\infty}^{\infty}\frac{\delta_\alpha}{1+\exp\left[\frac{W+E_{t,\alpha}-E_F}{k_BT}\right]} \times \exp\left[-\frac{B}{\gamma_a F}\left(\phi+E_{t,\alpha}\right)^{3/2}\right]\exp\left[c_{1,\alpha}\left(W+E_{t,\alpha}-E_F\right)\right]dW \tag{B.1}$$

This definite integral has a standard solution and its evaluation yields a temperature-dependent equation for the emitted current density due to a single subband of elec-

trons, with index α.

$$J^{u}_{wire,\alpha}(F) = e\frac{2}{hA_e}\delta_\alpha \frac{c_{1,\alpha}\pi k_B T}{\sin\left[c_{1,\alpha}\pi k_B T\right]} c_{1,\alpha}^{-1} \exp\left[-\frac{B}{\gamma_a F}\left(\phi + E_{t,\alpha}\right)^{3/2}\right] \quad \text{(B.2)}$$

Taking the limit as $T \to 0$ K and summing over all subbands yields an approximate, analytical solution for the emitted current density from a NU rectangular nanowire, per unit area, which is Equation 3.50.

B.2 Normally-Confined Emitted Current Density Equations

B.2.1 NC Nanowall

As $T \to 0$ K, $\ln\left[1 + \exp\left[\left(E_F - W_q\right)/k_B T\right]\right] \simeq \left(E_F - W_q\right)/k_B T$ and the expression is simplified to

$$J^{c}_{wall,q}\left(W_q, F\right) = e\frac{8\pi m_0}{h^3}\frac{W_q}{q}\delta_q\left(E_F - W_q\right)\exp\left[-\frac{B}{\gamma_a F}\left(\phi + E_F - W_q\right)^{3/2}\right] \quad \text{(B.3)}$$

The total emitted current density is found by summing over all subbands of electrons in the system, with the terminal subband index Q given by Equation 3.41, yielding Equation 3.55.

B.2.2 NC Rectangular Nanowire

While the supply function for a normally-confined rectangular nanowire is readily found by using Equation 3.30b and Equation 3.29b, the integral has no known ana-

lytical solution and approximations must be made in order to continue.

$$N_{q,\alpha}\left(W_q\right) = \frac{4}{2\pi d L_e}\sqrt{\frac{2W_q}{m_0}}\delta_q\delta_\alpha\int_0^\infty \frac{1}{1+\exp\left[\frac{\frac{\hbar^2 k_t^2}{2m_0}+E_{t,\alpha}+W_q-E_F}{k_B T}\right]}dk_t \tag{B.4}$$

The integral is recognized as the Fermi-Dirac integral of order $-1/2$ and the supply function can be recast with the integral in standard form with $x = \hbar^2 k_t^2/\left(2m_0 k_B T\right)$ and $\eta = \left(E_F - E_{t,\alpha} - W_q\right)/k_B T$. In the limit as $T \to 0$ K, $\eta \to \infty$ and ∞ can be replaced by η as the upper limit of integration.

$$N_{q,\alpha}\left(W_q\right) = \frac{4}{dhL_e}\sqrt{W_q k_B T}\delta_\alpha\delta_q\int_0^\eta \frac{x^{-1/2}}{1+\exp\left[x-\eta\right]}dx \tag{B.5}$$

As $\eta \gg 1$, the exponential in the denominator is negligible compared to unity and the integrand can be approximated by $2x^{1/2}$, yielding an approximation of the supply function that is within approximately 2% of the exact value [93].

$$N_{q,\alpha}\left(W_q\right) = \frac{8}{dhL_e}\delta_q\delta_\alpha\sqrt{W_q\left(E_F - E_{t,\alpha} - W_q\right)} \tag{B.6}$$

Multiplying the supply function by the elementary charge and transmission function in Equation 3.40 and summing over all subbands produces the rectangular nanowire emitted current density equation, as given in Equation 3.58.

B.2.3 NC Cylindrical Nanowire

Since emission from a NC cylindrical nanowire is always in the radial direction and the well is defined radially, there are no confined transverse energy levels $E_{t,\alpha}$. However, a portion of the subband energy in the cylindrical well is non-radial in nature and the normal (radial in this case) energy is given by Equation 3.20, denoted by $W_{\alpha_{m,n}}$. The electron travels a distance equal to four times the nanowire radius a between

collisions with the emitting surface and the length over which the emission occurs is half the circumference of the nanowire: $L_e = \pi a$. These definitions yield the emitted current density equation for the NC cylindrical nanowire:

$$J^c_{cwire}\left(W_{\alpha_{m,n}}, F\right) = e\frac{2}{\pi a^2 h}\sum_{m,n}\delta_{\alpha_{m,n}}\sqrt{W_{\alpha_{m,n}}\left(E_F - W_{\alpha_{m,n}}\right)} \times \exp\left[-\frac{B}{\gamma_a F}\left(\phi + E_F - W_{\alpha_{m,n}}\right)^{3/2}\right] \tag{B.7}$$

Appendix C

Field Enhancement Factor

When a uniform electric field is applied to a convex surface, the maximum magnitude of the electric field at the apex is greater than the average field far from the surface. The expression for the field at the apex of the curved surface is dependent upon the specific geometry of the surface. This consequence of electrostatics is important for field emission, as fabricating emitters with very small radii of curvature allows for field emission to occur at lower applied voltages than predicted by the elementary FN equation. In this section, the emitting surfaces of the geometries studied in Chapter 3 are modeled as a (i) floating sphere at the emitter plane potential, (ii) a floating cylinder at the emitter plane potential, or (iii) a perfectly planar surface.

C.1 Floating Sphere at Emitter Plane Potential

Due to bulk emitters typically being shaped like a needle or whisker, the emitter tip is commonly modeled as a hemisphere on a post or an emitting sphere floating above an emitter plane. Of the emitter geometries studied in Chapter 3, the floating sphere model is applicable to the bulk emitter, NU rectangular nanowire, and NU cylindrical nanowire. The field enhancement factor at the apex of the floating sphere is equal

to [31]

$$\gamma_a \simeq 3.5 + \frac{l}{\rho} \tag{C.1}$$

where l is the height of the center of the sphere above the emitter plane and ρ is the radius of the sphere.

C.2 Semicylinder on Emitter Plane

For emitter geometries that are more accurately described as emitting along an edge, rather than emitting from a tip, a better model for the field enhancement factor is that of a floating cylinder at the emitter plane potential. Before embarking on that derivation, it is useful to determine the lower limit on the field enhancement factor at the apex of the cylinder. This lower limit is set by the model of a semicylinder of radius ρ resting on the emitter plane, as shown in Figure C-1. The solution to the electrostatics problem posed here is entirely determined by the boundary conditions specified by the model: (i) far away from the semicylinder, $F = F_M$, where F_M is defined as the average, uniform electric field applied to the emitter (ii) the semicylinder and the emitter plane must form an equipotential system, and (iii) the semicylinder and emitter plane must be at a uniform potential.

Figure C-1: The "semicylinder on emitter plane" model consists of a semicylinder of radius ρ on a plane. The semicylinder and emitter plane form an equipotential system.

Using Gauss's Law, a uniform electric field of magnitude F_M, far away from the

semicylinder is generated by a sheet charge on the emitter plane equal to $\sigma = \epsilon_0 F_M$. This also creates a potential $\Phi_p(y) = -yF_M$, where y is measured as the distance above the emitter plane. In order for the emitter plane and semicylinder to form an equipotential system, the potential at the surface of the semicylinder must be $\Phi_d(y) = yF_M$. Due to the application of the field to the semicylinder, the natural choice for the source of this potential is an infinitely long line of dipoles oriented in the y direction and centered on the emitter plane surface. The potential from an infinitely long line of dipoles can be modeled as two infinitely long lines of charge (one positive, one negative), separated by a distance d. The potential from an infinitely long line of charge is given by [94]

$$\Phi_{line} = -\frac{\rho_L}{2\pi\epsilon_0}\ln[\rho] \qquad \text{(C.2)}$$

where ρ_L is the line charge density and ρ is the radial distance away from the line charge in cylindrical coordinates. Summing the potential contributions from both line charges and taking the limit as $d \to 0$ yields an expression for the potential from an infinitely long line of dipoles:

$$\Phi_d = \frac{P_L \cos[\phi]}{2\pi\epsilon_0\rho} \qquad \text{(C.3)}$$

where P_L is the dipole density and ϕ is the polar angle as measured from the y axis. Equating Equation C.3 with the boundary condition $\Phi_d = \rho\cos(\phi) F_M$ leads to a dipole density of

$$P_L = 2\pi\epsilon_0 F_M \rho^2. \qquad \text{(C.4)}$$

The goal is to determine the field at the apex of the semicylinder, which corresponds to $\phi = 0$. At the apex, it can be shown that the non-radial component of the electric field from the line of dipoles is zero, while the expression for the radial electric field

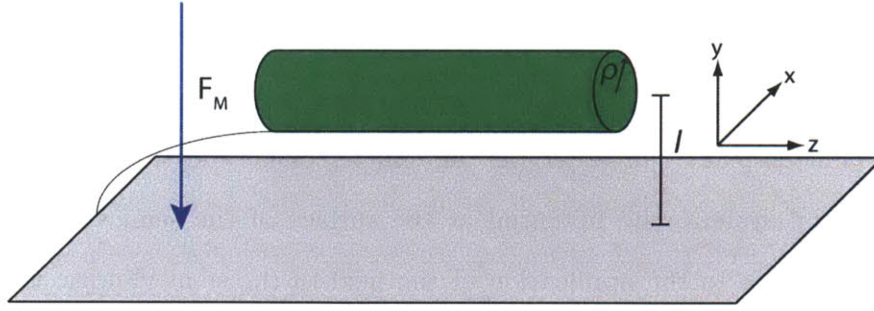

Figure C-2: In the "floating cylinder at emitter plane potential" model, the center of a cylinder of radius ρ is a distance l above the emitter plane. The wire between the cylinder and the emitter plane indicates that they form an equipotential system.

is

$$F_\rho(\rho) = \frac{P_L}{2\pi\epsilon_0\rho^2}\hat{\rho} \tag{C.5}$$

Inserting the dipole density from Equation C.4 gives the radial field at the apex of the cylinder from the dipoles as $F_\rho = F_M$. Summing this with the contribution at the apex from the emitter plane gives $F_a = 2F_M$ and an apex field enhancement factor of

$$\gamma_a = 2 \tag{C.6}$$

C.3 Floating Cylinder at Emitter Plane Potential

The "floating cylinder at emitter plane potential" model, illustrated by Figure C-2, is similar to the semicylinder on a plane model except that the center of the cylinder is elevated a distance l above the emitter plane. Assuming the apices of the emitters are curved, this model is appropriate for describing emission from the NU nanowall and NC nanowire geometries. Using the same dipole and sheet charge densities as were used in the "semicylinder on emitter plane" model leads to a difference in potential between the emitter plane and the cylinder surface of approximately $\Delta\Phi = -lF_M$. In order to eliminate this potential difference and restore the equipotential system, an infinitely long line of positive charge can be introduced at the center of the cylinder.

Setting the potential of an infinitely long line of charge equal to the negative of the potential difference requires that the charge density of the line of charge be

$$\rho_{L1} = -\frac{2\pi\epsilon_0}{lF_M \ln\left[\rho\right]}. \tag{C.7}$$

However, this line of charge creates a non-uniform potential distribution across the emitter plane that again upsets the equipotential system. This non-uniformity can be rectified by placing an image line charge a distance l behind the emitter plane with charge density ρ_{L1}. However, the addition of this image line charge does not yet solve the problem because it changes the potential at the surface of the cylinder. By ensuring that the sum of the potentials from the additional line charge and image line charge add up to lF_M, the line charge density can be chosen such that boundary conditions are met:

$$P_{L2} = \frac{2\pi\epsilon_0 lF_M}{\ln\left(\frac{2l}{\rho}\right)} \tag{C.8}$$

Inserting this dipole density into Equation C.3 gives the contributions to the radial electric field at the apex from the line charge and the image line charge

$$\begin{aligned} F_{a,l}\left(\rho\right) &= \frac{F_M}{\ln\left(\frac{2l}{\rho}\right)}\frac{l}{\rho}\hat{\rho} \\ F_{a,im}\left(\rho\right) &= -\frac{F_M}{\ln\left(\frac{2l}{\rho}\right)}\frac{1}{2}\hat{\rho} \end{aligned} \tag{C.9}$$

Adding these terms to the radial field at the apex of the "semicylinder on emitter plane" model yields the field enhancement factor at the apex:

$$\gamma_a = 2 + \frac{1}{\ln\left(\frac{2l}{\rho}\right)}\left(\frac{l}{\rho} - \frac{1}{2}\right). \tag{C.10}$$

Appendix D

Emission from an Accumulation Layer

D.1 Accumulation Layer Well

When a negative electric field is applied to the surface of a non-degenerately doped semiconductor, a portion of the field penetrates into the material. As a response, the electrons in the conduction band of the semiconductor move towards the semiconductor-vacuum interface to set up an canceling electric field to reach equilibrium within the material. The presence of the electric field inside the semiconductor causes the conduction band to bend downwards (often below the Fermi level) and forms an accumulation layer of electrons.

According to the Poisson-Boltzmann formulation of band bending for an n-type semiconductor in Appendix A, the conduction band has an approximate shape given by:

$$E_c(z) = 2k_BT\ln\left[\frac{z}{\sqrt{2}L_D} + \frac{1}{F_{vac}\frac{\epsilon_0}{\epsilon_s}\sqrt{\frac{\epsilon_s}{2N_Dk_BT}}}\right] \quad \text{(D.1)}$$

where z is the distance from the semiconductor-vacuum interface into the material, ϵ_s

is the permittivity of the semiconductor, F_{vac} is the applied electric field in vacuum, N_D is the donor dopant concentration, L_D is the Debye length, and $\sqrt{2}L_D$ is the extent of the accumulation layer. The total amount of band bending is given by evaluating Equation D.1 at $z = 0$:

$$\Delta E_c = 2k_BT \ln \left[F_{vac} \frac{\epsilon_0}{\epsilon_s} \sqrt{\frac{\epsilon_s}{2N_Dk_BT}} \right]. \tag{D.2}$$

Like the electrons in an inversion layer of a MOSFET [4], the electrons in an accumulation layer are confined by a potential related to the downward bending of the conduction band. Similar to NC emitters, this confining potential creates an "accumulation layer well" in which electrons are normally quantum confined. The accumulation layer well is bounded by the conduction band edge in the bulk, the conduction band edge near the interface, and the semiconductor-vacuum interface, as shown in Figure D-1.

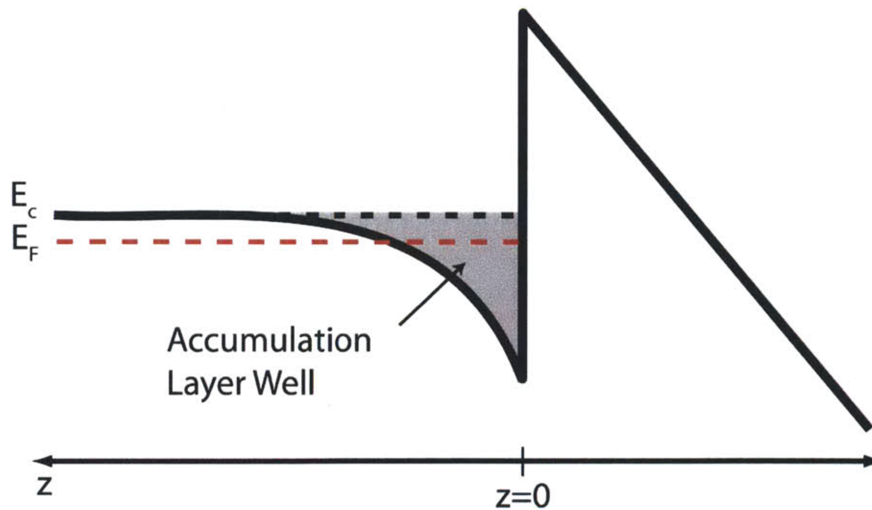

Figure D-1: The accumulation well is bounded by the energy of the conduction band edge in the bulk, the conduction band edge near the interface, and the semiconductor-vacuum boundary.

The energy levels in the well cannot be calculated exactly via analytical methods, but approximate analytical forms for the bound state energies can be derived from

a form of the JWKB approximation [95]. In this method, the energy levels are calculated based upon the classical turning points of the particle and setting the wave function's phase difference by specifying the number of walls with infinite potentials. The normalized time-independent Schrödinger equation is

$$\epsilon\psi\left(y\right) = -\frac{d^2}{dy^2}\psi\left(y\right) + v\left(y\right)\psi\left(y\right) \tag{D.3}$$

where ϵ is the normalized energy, ψ is the wave function, and v is the normalized potential. By using the sine version of the JWKB approximation, the wave function is given by

$$\psi\left(y\right) = \frac{\sin\left[\phi\right]}{\sqrt{\eta}} \tag{D.4}$$

where ϕ is the phase of the wave function and $\eta = \pm\sqrt{\epsilon - v\left(y\right)}$. The phase difference for a potential well with one hard boundary (semiconductor-vacuum interface) and one soft boundary (conduction band edge in the semiconductor) should be equal to $\left(n - 1/4\right)\pi$ and is calculated by integrating over η between minimum and maximum y values. Normalizing the Schrödinger equation requires that the variables in use be scaled accordingly, giving

$$\begin{aligned} y &= \frac{z}{\sqrt{2}L_D} \\ \epsilon &= \frac{8m_0L_D^2}{\hbar^2}E \\ c &= \frac{16m_0k_BTL_D^2}{\hbar^2} \\ a &= \exp\left[-\frac{e\phi_s}{2k_BT}\right] \end{aligned} \tag{D.5}$$

where ϕ_s is the potential at the semiconductor surface. With the above definitions, the potential is defined as

$$v\left(y\right) = c\ln\left[y\right] \tag{D.6}$$

and the equation to solve for the energy levels is

$$\int_{y_{min}}^{y_{max}} \sqrt{\epsilon - c \ln [y]} dy = (n - 1/4) \pi. \tag{D.7}$$

Using the electron's classical turning points as the limits of integration yields $y_{min} = 0$ and $y_{max} = \exp [\epsilon / c]$. Carrying out the integration and solving for the energy levels gives

$$\begin{aligned} \epsilon &= \ln \left[2\sqrt{\pi} \left(n - \frac{1}{4} \right) \right] \\ E_n &\approx 2 k_B T \ln \left[\frac{\hbar}{2 L_D} \sqrt{\frac{\pi}{m_0 k_B T}} \left(n - \frac{1}{4} \right) \right]. \end{aligned} \tag{D.8}$$

The first five normalized energy levels of the accumulation layer well are given in Table D.1.

In order to check the validity of the approximate energy levels, the energies were calculated exactly by using a three-point shooting Numerov method [96]. Via this method, the normalized time-independent Schrödinger equation is discretized and valid energy levels are found by adjusting the normalized energy parameter until the wave function satisfies all requisite boundary conditions. The Numerov normalized time-independent Schrödinger equation is given by

$$u_{i+1} = 2u_i - u_{i-1} + h^2 u_i (\ln [y_i] - \epsilon) \tag{D.9}$$

where u is the wave function, the subscripts indicate the position in discrete space as a function of the index i, h is the spacing between points, y is the normalized position coordinate, and ϵ is the normalized energy. Setting the initial index of the wave function, which is far into the semiconductor, to 0 and adjusting ϵ until the wave function equals zero at the semiconductor-vacuum interface results in the normalized energies for the well. The first five normalized energies are listed in Table D.1, which

n	Approximate	Exact
1	0.97783	1.04375
2	1.82513	1.84625
3	2.27711	2.28875
4	2.58727	2.59500
5	2.82366	2.82875

Table D.1: Normalized energy levels for the logarithmic well calculated via the approximate JWKB method and exact three-point shooting Numerov method.

n \ N_D (cm^{-3})	10^{15}	10^{16}	10^{17}	10^{18}	10^{19}
1	-0.24447	-0.18497	-0.12546	-0.06596	-0.00645
2	-0.20068	-0.14117	-0.08167	-0.02216	0.03734
3	-0.17732	-0.11781	-0.05831	0.00120	0.06070
4	-0.16129	-0.10178	-0.04228	0.01723	0.07673
5	-0.14907	-0.08956	-0.03006	0.02945	0.08895

Table D.2: The first five energy levels in the accumulation layer well as a function of the donor dopant density in eV at $T = 300$ K. The conduction band edge in the bulk is taken as the energy reference.

shows good agreement between the energy values generated by the two methods. As an additional note, changing the applied field (which changes the potential) has little to no effect on the relative location energy levels and energy level spacing with respect to the bottom of the well at the semiconductor-vacuum interface, consistent with Equation D.8.

The shape and size of the accumulation layer well changes for different donor dopant densities, as the electron concentration near the semiconductor surface determines the extent to which the applied field penetrates. Since the typical donor dopant densities of electrons in silicon typically range from 10^{15} cm^{-3} to 10^{19} cm^{-3}, the first five approximate subband energies for the logarithmic well with these dopant densities are given in Table D.2.

D.2 Accumulation Layer Emitted Current Density

The calculation of the emitted current density from the accumulation layer is the same as that of a normally-confined emitter. As an example, the ECD from a bulk silicon emitter will be considered for various values of N_D at a constant applied field. The supply function is the product of the attempt frequency and the transverse electron density. Using the general form for the attempt frequency and the logarithmic shape of the conduction band gives

$$\nu_q^{acc}(W_q) = \sqrt{\frac{k_B T}{2\pi m_0 L_D^2}} \exp\left[-\frac{W_q}{2k_B T}\right] \left\{ \text{Erf}\left[\sqrt{\frac{W_q}{2k_B T} - \ln\left[\frac{1}{F_{vac}\frac{\epsilon_0}{\epsilon_s}\sqrt{\frac{\epsilon_s}{2N_D k_B T}}}\right]}\right] \right.$$
$$\left. -\text{Erf}\left[\sqrt{\frac{W_q}{2k_B T} + \ln[2] - \ln\left[\frac{2}{F_{vac}\frac{\epsilon_0}{\epsilon_s}\sqrt{\frac{\epsilon_s}{2N_D k_B T}}}\right] + \frac{\sqrt{2}Z_q}{L_D}}\right] \right\}^{-1} \tag{D.10}$$

where Z_q is the classical turning point of the electrons in each subband given by

$$Z_q = \hbar\sqrt{\frac{\pi}{2m_0 k_B T}}\left(n - \frac{1}{4}\right) - \frac{\sqrt{2}L_D}{F_{vac}\frac{\epsilon_0}{\epsilon_s}\sqrt{\frac{\epsilon_s}{2N_D k_B T}}}. \tag{D.11}$$

The transverse electron density is the same as in the bulk emitter:

$$n_{t,q}(W_q) = \frac{2\pi m_0 k_B T}{h^2} \ln\left[1 + \exp\left[-\frac{W_q - E_F}{k_B T}\right]\right]. \tag{D.12}$$

The transmission function takes an unexpanded form:

$$D_q(F, W_q) = \exp\left[-\frac{B}{F}(\chi_e - W_q)^{3/2}\right]. \tag{D.13}$$

N_D cm^{-3}	$J_{acc,bulk}$ $[\mu A/cm^2]$	J_{bulk} $[\mu A/cm^2]$
10^{15}	2.85×10^{-3}	3.51×10^{-4}
10^{16}	3.17×10^{-2}	3.50×10^{-3}
10^{17}	0.320	3.50×10^{-2}
10^{18}	2.90	0.349
10^{19}	24.0	3.49

Table D.3: Emitted current density from the accumulation layer well of a bulk silicon emitter ($J_{acc,bulk}$) and from the bulk silicon ECD equation without band bending (J_{bulk}) for $F = 2 \times 10^7$ V/cm.

Per subband, the emitted current density is given by the product of the supply function and transmission function

$$\begin{aligned} J_{acc,bulk,q}(F) &= e\frac{2\pi m_0 k_B T}{h^2}\nu_q^{acc} \\ &\times \ln\left[1+\exp\left[-\frac{W_q - E_F}{k_B T}\right]\right]\exp\left[-\frac{B}{F}\left(\chi_e - W_q\right)^{3/2}\right] \end{aligned} \tag{D.14}$$

In order to obtain the total ECD, the ECD contributions from all subbands in the system must be totaled, giving

$$\begin{aligned} J_{acc,bulk}(F) &= e\frac{2\pi m_0 k_B T}{h^2}\sum_q \nu_q^{acc} \\ &\times \ln\left[1+\exp\left[-\frac{W_q - E_F}{k_B T}\right]\right]\exp\left[-\frac{B}{F}\left(\chi_e - W_q\right)^{3/2}\right] \end{aligned} \tag{D.15}$$

Comparing the ECD from the accumulation layer well to the ECD equations derived in Chapter 4 that do not include band bending reveal that the accumulation layer ECD is significant. For a single, free-electron constant energy surface of a bulk semiconductor emitter with a Fermi energy below the conduction band edge in the bulk, the ECD is given by

$$J_{bulk}(F) = e\frac{4\pi m_0 k_B T}{h^3}\exp\left[\frac{E_F}{k_B T}\right]\exp\left[-\frac{B}{F}\chi_e^{3/2}\right]. \tag{D.16}$$

Table D.3 lists the total ECDs from the accumulation layer well of a bulk silicon emitter and from Equation D.16. Results show that the ECD from the accumulation

layer well is significant and cannot be neglected in studies of field emission from non-degenerately doped semiconductor emitters. As of now it is unclear whether the accumulation layer ECD is the only physical ECD from semiconductor emitters or if it is in addition to the ECD calculated without band bending.

Appendix E

Transition Region Between Emitter Dimensionalities

E.1 Transition Point

A possible benchmark for determining approximately when an emitter transitions from being quantum-confined to bulk is the well size for which the FN plot and the NUFN plots give the same extracted work function. Since these plots assume a constant slope when plotted against $1/F$, the transition point derived using this method is independent of the applied field. The extracted transition region midpoint as a function of selected values of ϕ and m_n^* is listed in Table E.1. The results show the trends in the work function and effective mass as discussed in §5.2 and predict a transition point that ranges from approximately 2 nm to 6 nm.

m^* $[m_0]$ / ϕ [eV]	0.25	0.50	0.75	1.00
2	4.57	3.23	2.64	2.28
3	5.04	3.56	2.91	2.52
4	5.41	3.82	3.12	2.70
5	5.70	4.04	3.29	2.85

Table E.1: The midpoint of the transition region between the NU nanowall and bulk emitter, as determined by matching the extracted work functions from the FN plot and NUFN plots for the nanowall emitter, given in terms of L_x (nm).

E.2 Transition Region and the Influence of System Parameters

For both the NU and NC ECD plots, the point at which the emitters change from being 1D or 2D to 3D electron gases is unclear. However, this transition happens over a range of well widths for which the normalized ECD is between 0 and the FN limit, termed the transition region. While for the elementary ECD equations, the width of this transition region remains rather constant for a given emitter geometry, system parameters such as the work function, effective mass(es) of electrons in the quantum well(s), and the applied electric field can change the well widths over which it occurs. The effects of these system parameters on the NU nanowall emitter's normalized ECD and transition region are investigated below. Although changes in the work function, effective mass, and applied field have the same effects on the ECD of NC emitters as in NU emitters, there is no well-defined transition region. Another system parameter, the Fermi energy, plays less of a role in determining the transition region, but is responsible for important qualitative characteristics of the normalized ECD plots for both NU and NC emitters.

E.2.1 Work Function

The magnitude of the work function plays a significant role in determining the degree of confinement of an emitter, as it sets the reference barrier height within each subband of electrons. Keeping the well width, Fermi energy, and applied field constant, decreasing (increasing) the work function leads to a lower (higher) barrier to transmission for all electron subbands in the well. As a result, the subbands with the lowest reference barrier heights constitute a smaller (larger) fraction of the total ECD, while the higher energy subbands contribute a larger (smaller) fraction than before the decrease (increase) in the work function. Thus, lowering (raising) the work function increases (decreases) the number of subbands contributing significant currents to the total ECD. Figure E-1 and Figure E-2 illustrate the effect of changing ϕ on the normal energy diagram and ECD curve for an NU nanowall emitter: a shift of the transition region to the left (right) as ϕ decreases (increases).

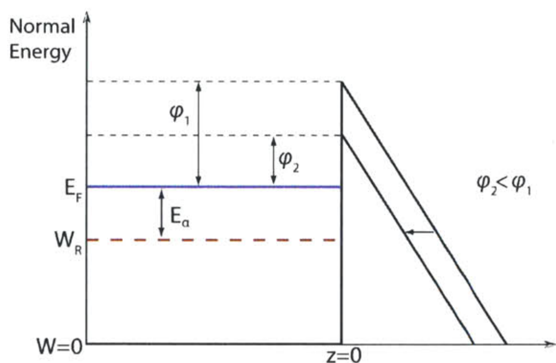

Figure E-1: Normal energy diagram for emission from the NU nanowall. Lowering ϕ reduces the barrier thickness seen at the reference energy W_R and increases the transmission probability of electrons in that subband.

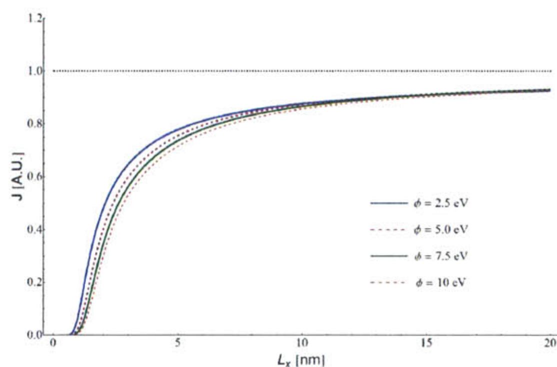

Figure E-2: The ECD of the NU nanowall normalized to the FN equation, as a function of the transverse well width L_x with the work function as a parameter, for which $F = 2 \times 10^7$ V/cm, $E_F = 10$ eV.

E.2.2 Effective Mass of Electrons

The effective mass of electrons in the infinite square well is inversely proportional to energy levels of the well. Thus, increasing (decreasing) the effective mass of electrons leads to a downward (upward) migration of energy levels in the well and a lowering (raising) of the reference zero-field barrier height for electrons in each subband, as in Figure E-3. In addition, due to the condition that for $T = 0$ K, no subbands with energies above E_F may contribute to emission, an increase (decrease) in the effective mass could result in subbands being added to (removed from) the well. These two effects are responsible for the leftward (rightward) shift of the normalized ECD curves for the NU nanowall emitter as the effective mass is increased (decreased), as shown in Figure E-4.

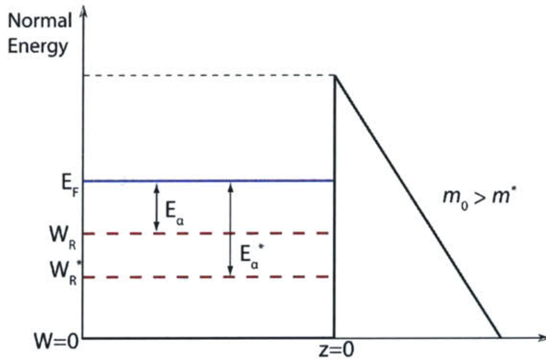

Figure E-3: Normal energy diagram for emission from the NU nanowall. Decreasing the effective mass of electrons in the well, m^* causes all well energy levels to migrate upwards in energy, leading to a decrease in the reference state energy from W_R to W_R^* and a reduced transmission probability for electrons in that subband.

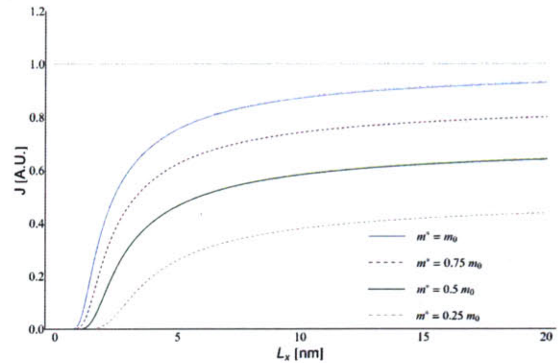

Figure E-4: The ECD of the NU nanowall normalized to the FN equation, as a function of the transverse well width L_x with the effective mass m^* as a parameter, for which $F = 2 \times 10^7$ V/cm, $E_F = 10$ eV, $\phi = 5$ eV.

E.2.3 Applied Electric Field

The applied field also has a significant effect on the absolute location of the transition region between emitter dimensionalities. Increasing (decreasing) the applied field has the direct effect of increasing (decreasing) the transmission probability of all subbands in the well due an overall thinning (thickening) of the barrier to emission, as shown in Figure E-5. Consequently, an increase (decrease) in the applied field leads to more (fewer) subbands contributing to emission and a shift in the transition region to the left (right). Figure E-6 shows ECD plots from the elementary NU nanowall emitter as a function of the applied field.

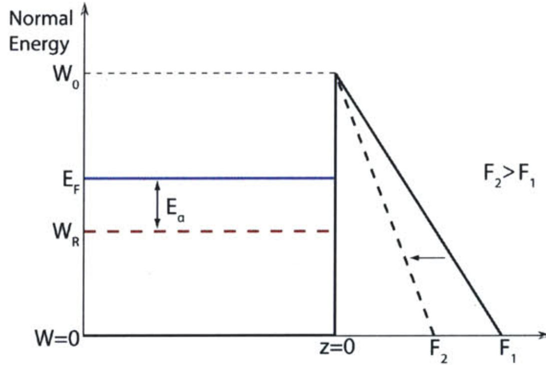

Figure E-5: Normal energy diagram for emission from the NU nanowall. Increasing the applied electric field directly reduces the barrier thickness seen by electrons at reference energy W_R, increasing their transmission probability.

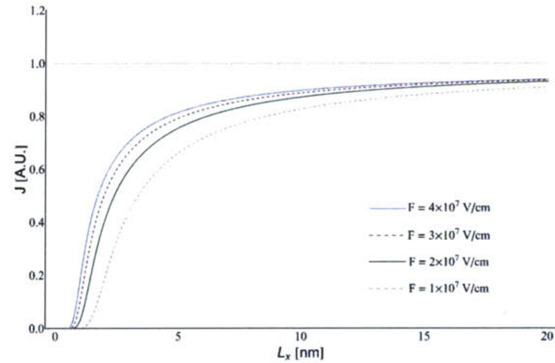

Figure E-6: The ECD of the NU nanowall normalized to the FN equation, as a function of the transverse well width L_x with the applied field as a parameter, for which $E_F = 10$ eV and $\phi = 5$ eV.

E.2.4 Fermi Energy

For $T = 0$ K, the Fermi energy marks the sharp boundary between occupied electronic states (below E_F) and non-occupied electronic states (above E_F). As was discussed above, electron subbands with energies above E_F cannot contribute to the total ECD from a quantum-confined emitter. As a consequence of this cutoff in the electron supply, the absolute magnitude of the Fermi energy determines the smallest well-

width for which the total ECD of an emitter is non-zero. For the NU nanowall emitter, the smallest infinite square well with a Fermi energy E_F that can support an electron subband is

$$w_{on} = \sqrt{\frac{h^2}{8m_0E_F}}. \tag{E.1}$$

While a higher E_F ensures a lower w_{on}, it does not guarantee a higher ECD from the nanowall emitter or a faster convergence to the FN limit. With a larger E_F, subbands can be admitted into the well at much smaller well widths, but these subbands see a reference zero-field barrier height equal to

$$H_R = \phi + \frac{h^2}{8m_0w_{on}^2}. \tag{E.2}$$

Consequently, a lower w_{on} also corresponds to a higher barrier to transmission for electrons in the subband, leading to a lower subband ECD and no leftward or rightward shift in the ECD curve due to changes in E_F.

While changes in E_F result in no horizontal shifts in the normalized ECD plots, the qualitative characteristics of ECD plots for NU and NC emitters can be altered in other ways by lowering the Fermi level to values near zero. For NU emitters, lowering E_F below some energy $E_{F,crit}$ results in the segmentation of the continuous normalized ECD curve into multiple curves that represent the ECD contributions from each of the subbands in the well, as shown in Figure E-7. These discontinuities occur in the ECD plot if the Fermi energy is low enough that when new subbands are admitted into the well ($E_{\alpha_x} < E_F$), their reference zero-field barrier heights are low enough that the subband ECD is significant compared to the ECD contributions from the subbands already in the well. Roughly, the discontinuities begin to appear in the ECD plots when the ECD from the newly-added subband exceeds approximately 1% of the ECD from the next highest subband. Using the ECD from the first two

subbands of the NU nanowall to calculate the cutoff E_F leads to the expression

$$0.01 < \left(\frac{\phi + E_1}{\phi + E_2}\right)^{3/4} + \exp\left[-\frac{B}{F}\left(\phi + E_2\right)^{3/2} - \left(\phi + E_1\right)^{3/2}\right] \tag{E.3}$$

where E_1 and E_2 are the first and second subband energies of the infinite square well, respectively. Since the discontinuities occur when a new subband is added to the well,

$$\begin{aligned} E_2 &= E_F \\ E_1 &= \frac{E_2}{4} = \frac{E_F}{4}. \end{aligned} \tag{E.4}$$

Making the substitutions for the energy levels and taking the log of both sides leads to

$$\ln\left[0.01\right] < \ln\left[\left(\frac{\phi + \frac{E_F}{4}}{\phi + E_F}\right)^{3/4}\right] - \frac{B}{F}\left(\phi + E_F\right)^{3/2} - \left(\phi + \frac{E_F}{4}\right)^{3/2}. \tag{E.5}$$

Assuming that this critical Fermi energy is much smaller than the work function leads to an expression for $E_{F,crit}$ of the form

$$E_{F,crit} \approx \left[-\frac{F}{B}\left(\ln\left[0.01\right] - \frac{B}{F}\phi^{3/2}\right)\right]^{3/2} - \phi \tag{E.6}$$

which is appropriate for the NU nanowall. For $F = 2 \times 10^7$ V/cm and $\phi = 5$ eV, the predicted $E_{F,crit}$ for the NU nanowall is approximately 0.40 eV.

For NC emitters, lowering E_F results in two qualitative changes in the ECD: i) a decrease in the amplitude of the ECD oscillations and ii) a broadening of the ECD oscillations, leading to fewer oscillations over the same range of well widths. Due to E_F serving as the upper energy boundary for subbands in the well, a lower Fermi energy restricts the subbands to lower normal energies, W_q, and consequently, lower electron group velocities. The lower group velocities limit the electrons to comparatively lower arrival rates for the same well widths, leading to oscillations with lower maximum amplitudes. A lower E_F also results in fewer subbands entering

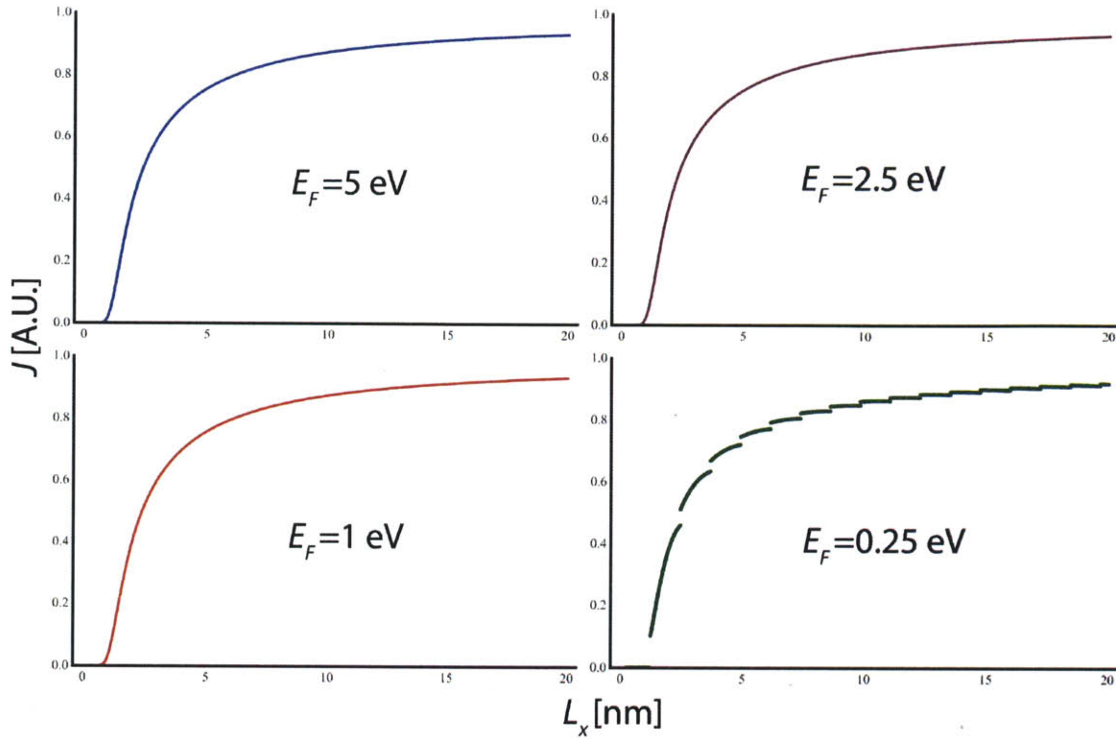

Figure E-7: The normalized ECD of the elementary NU nanowall for selected values of E_F. Above $E_{F,crit}$, changes in the Fermi energy do not affect the normalized ECD, while the ECD curve becomes discontinuous for Fermi energies below $E_{F,crit}$.

the well and contributing to emission over a change in well width ΔL_z. For example, over a range of normal well widths L_z, the magnitude of the energy migration of a higher energy level of index $n+k$ in terms of the magnitude of the energy migration of a lower energy level of index n is

$$\Delta E_{n+k} = \frac{(n+k)^2}{n^2} \tag{E.7}$$

showing that for the same change in L_z, higher energy levels in the well have a greater energy shift. As a result of the slower rate of change of lower energy levels with respect to L_z, a lower E_F leads to fewer subbands being added to the well (fewer oscillations) and a slower progression along the curve of the average number of emitted electrons for each subband in Figure 5-4 (broader oscillations). The normalized ECD of the NC nanowall emitter for selected values of E_F is shown in Figure E-8. For very

small values of E_F ($<\sim$ .20 eV), the assumption that extending the lower limit of integration over W from 0 to $-\infty$ breaks down and the normalized ECD of the NC nanowall converges to values smaller than unity. As a solution, the NC nanowall ECD is normalized to a numerically-integrated version of the elementary Fowler-Nordheim equation, shown in Figure E-8.

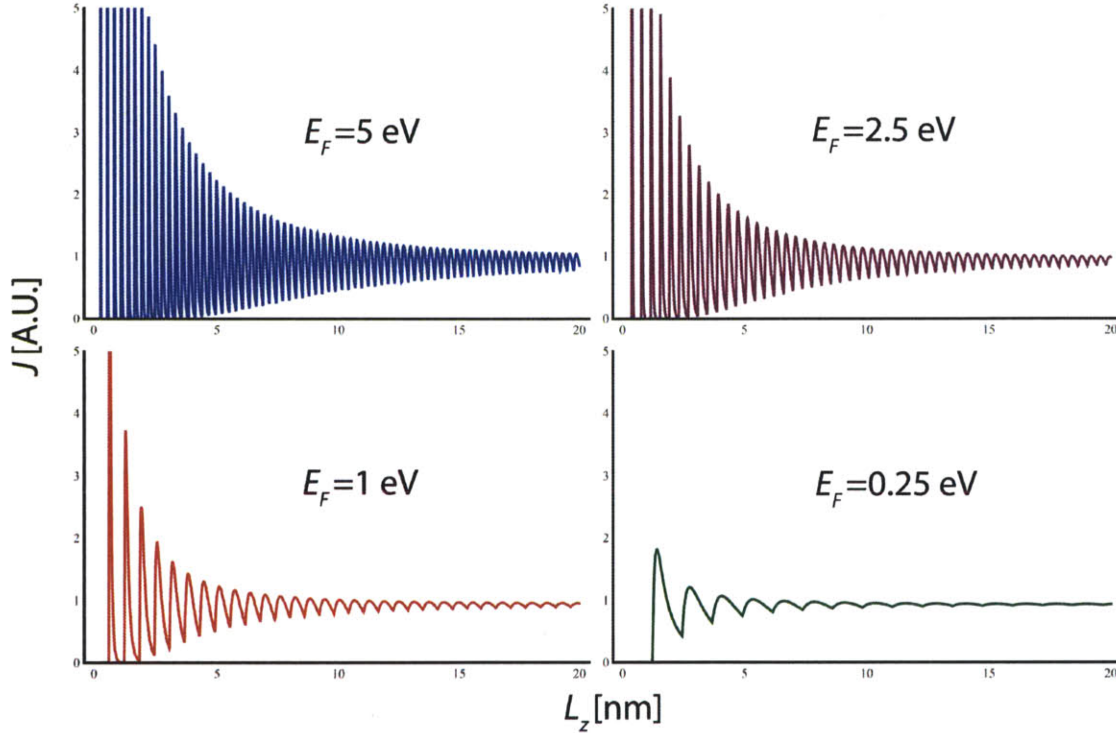

Figure E-8: The normalized ECD of the elementary NC nanowall for selected values of E_F. As E_F decreases, the normalized ECD oscillations decrease in amplitude, become broader, and converge more quickly to the FN limit. For values of E_F $<\sim$ 0.2 eV, the ECD is normalized to a numerically-integrated version of the FN equation.